Università degli Studi della Basilicata

Dottorato di Ricerca in

"Metodi e Tecnologie per il Monitoraggio Ambientale"

TITOLO DELLA TESI

"Study of droplet activation in thin clouds using ground-based Raman lidar and ancillary remote sensors"

Settore Scientifico-Disciplinare

Fis/06

Coordinatore del Dottorato
Prof. Aurelia Sole

Dottorando
Dott. Marco Rosoldi

Tutors
Dott. Gelsomina Pappalardo
Dott. Fabio Madonna

A.A. 2013/2014 Ciclo XXVII

INDEX

CHAPTER 1

INTRODUCTION

1.1 Overview of aerosol-cloud interactions

The study of aerosol and cloud properties has been historically divided into two separate disciplines within the field of atmospheric science. The attention paid to global climate change has shown that clouds can have a very relevant effect on the Earth's climate and the role played by aerosols in their formation, persistence, and dissipation is one of the most uncertain factors.

Aerosol-cloud interactions (ACI) occur through several processes. A few of them are relatively well studied and understood. For example, it is known that an increase in the aerosol concentration increases the number of droplets in warm clouds, decreases their average size, reduces the rate of precipitation, and extends the cloud lifetime. Other effects are not yet well known. For example, persistent ice super-saturated conditions are observed in the upper troposphere that appear to exceed our understanding of the conditions required for cirrus cloud formation. The aerosol activation, i.e. the cloud droplet formation from aerosol particles, is not yet accurately parameterized in global climate models and in cloud resolving models. It is probably the largest source of uncertainty in estimating the effects of ACI on Earth's radiation balance and climate, known also as indirect aerosol effects. The aerosol activation is a highly complex and nonlinear process, that depends on a multitude of parameters, such as size distribution of aerosols acting as cloud condensation nuclei (CCN), their chemical composition, meteorological conditions, updrafts and downdrafts within cloudy regions. Moreover, there are several issues in the performance of the instrumentation used to provide model input and to assess model performance. For example, the measurement of CCN concentrations is in itself a challenge, while a theoretical understanding of the different measurement methodologies, in both their strengths and limitations, is essential for evaluating instrumental uncertainties (Nenes, 2003).

A summary of the aerosol and cloud related processes, as reported in the Intergovernmental Panel on Climate Change Fifth Assessment Report, hereinafter IPCC 5th AR, is shown in Figure 1.1 (Boucher et al., IPCC, 2013).

The main uncertainty is associated with the effect of black carbon and organics (aerosol types of anthropogenic interest) on droplet and ice formation. The impact of natural aerosols on clouds (for example mineral dust) as well as of other natural but highly sensitive effects (for example the Wegener–Bergeron–Findeisen process, by which precipitation particles may form within a mixed phase cloud composed of both ice crystals and liquid water drops) needs also a better assessment.

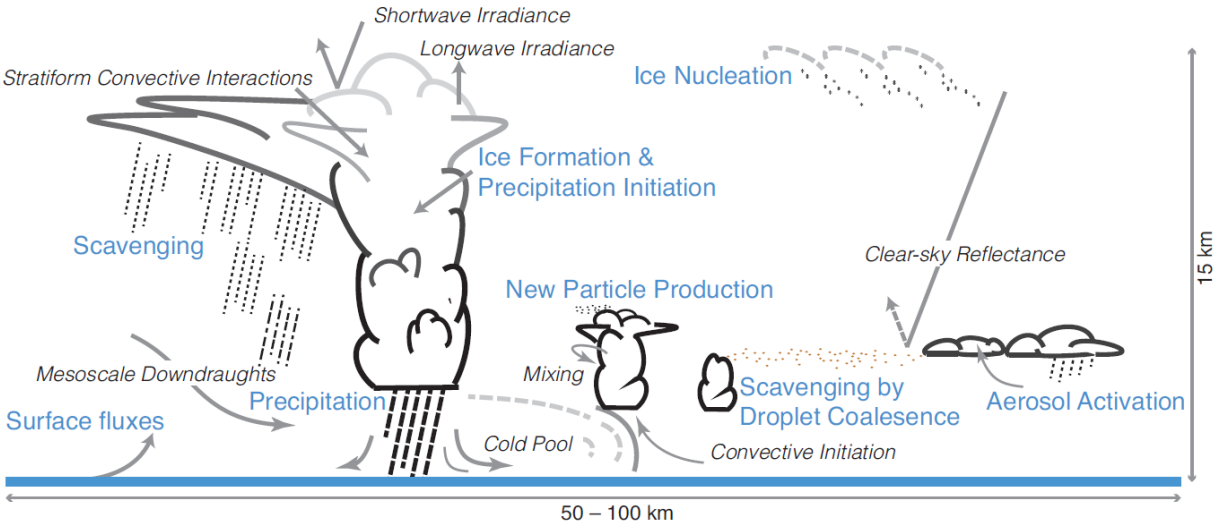

Figure 1.1: Aerosol and cloud related processes as summarized in the Intergovernmental Panel on Climate Change Fifth Assessment Report (IPCC 5th AR) [Boucher et al., IPCC, 2013]; processes that affect aerosol-cloud interactions are in blue; resulting secondary processes are in grey.

The cloud albedo effect is the increase in cloud reflectance that occurs as a result of an aerosol concentration increase in liquid clouds whose liquid water content remains constant (Twomey, 1974, 1977). The microphysical reason behind the albedo effect is related to the enhancement of cloud drop number concentrations and the decrease of cloud drop sizes, which lead to higher cloud reflectance. Secondary effects of aerosols on clouds are characterized by a suppression of precipitation (Albrecht, 1989), which is supposed to have the same microphysical reason of the albedo effect, but it is also due to an enhancement in evaporation (Wang et al., 2003; Xue and Feingold, 2006; Jiang et al., 2006), as well as by general microphysical-dynamical feedbacks associated with the boundary layer and free-tropospheric cloud system (e.g., Stevens et al., 1998; Ackerman et al., 2004). A further result of an increase in aerosol concentration would be an increase of the breadth of the cloud drop size distribution: this would have the effect of decreasing aerosol influences on shortwave radiation and on inhibition of precipitation development (Peng and Lohmann, 2003). The nature and magnitude of these effects are highly uncertain. The increase in

albedo of liquid water clouds due to anthropogenic aerosols is the mostly studied aerosol indirect effect.

Studies from global climate models suggest that in the absence of giant CCN and aerosol-induced changes in ice microphysics, anthropogenic aerosols suppress precipitation in liquid water clouds; precipitation would be suppressed as well as in mixed-phase clouds in which the ice phase plays only a minor role. A reduction in precipitation formation leads also to increased cloud processing of aerosols. Studies with cloud resolving models, on the other hand, have shown that cloud processing could lead either to an increase or decrease in precipitation formation in subsequent cloud cycles, depending on the size and concentration of activated CCN (Lohmann and Schwartz, 2008). When the actual cloud lifetime is analyzed in cloud resolving model simulations, an increase in aerosol concentration from very clean to strongly anthropogenically influenced situations does not increase cloud lifetime, even though precipitation is suppressed (Jiang et al., 2006). This effect is due to competition between precipitation suppression and enhanced evaporation of the more numerous smaller cloud droplets at high cloud droplet concentration.

Representation of the albedo effect in global-scale climate models has produced a negative (cooling) global annually averaged radiative forcing estimate of 0.7 W m^{-2}, with a 90% confidence range from – 0.3 W m^{-2} to – 1.8 W m^{-2} (Forster et al., IPCC, 2007). This radiative forcing represents the greatest uncertainty of all climate forcing mechanisms reported by the IPCC 4th AR. Radiative forcing, as defined by the IPCC, is the net change in irradiance at the tropopause after stratospheric equilibrium is reached, but with a fixed tropospheric state (Ramaswamy et al., 2001). Secondary aerosol-cloud effects are consequently relegated by IPCC to feedbacks or ‘‘responses’’ in the climate system as opposed to the ‘‘radiative forcing’’ of the albedo effect (Forster et al., IPCC, 2007). Figure 1.2 shows the estimations of radiative forcing for different atmospheric constituents and processes from the IPCC 5th AR (Stocker et al., IPCC, 2013). The horizontal bars represent the values of radiative forcing, while the thin black segments are the corresponding uncertainty ranges; green diamonds and associated uncertainties are referred to the estimations assessed in IPCC 4th AR. It is evident that the radiative forcing estimation with the lowest level of confidence and the greatest range of uncertainty is due to aerosol-cloud interactions. This contribution is of -0.45 W m^{-2} with a variability ranging from - 1.2 W m^{-2} to 0.0 W m^{-2}.

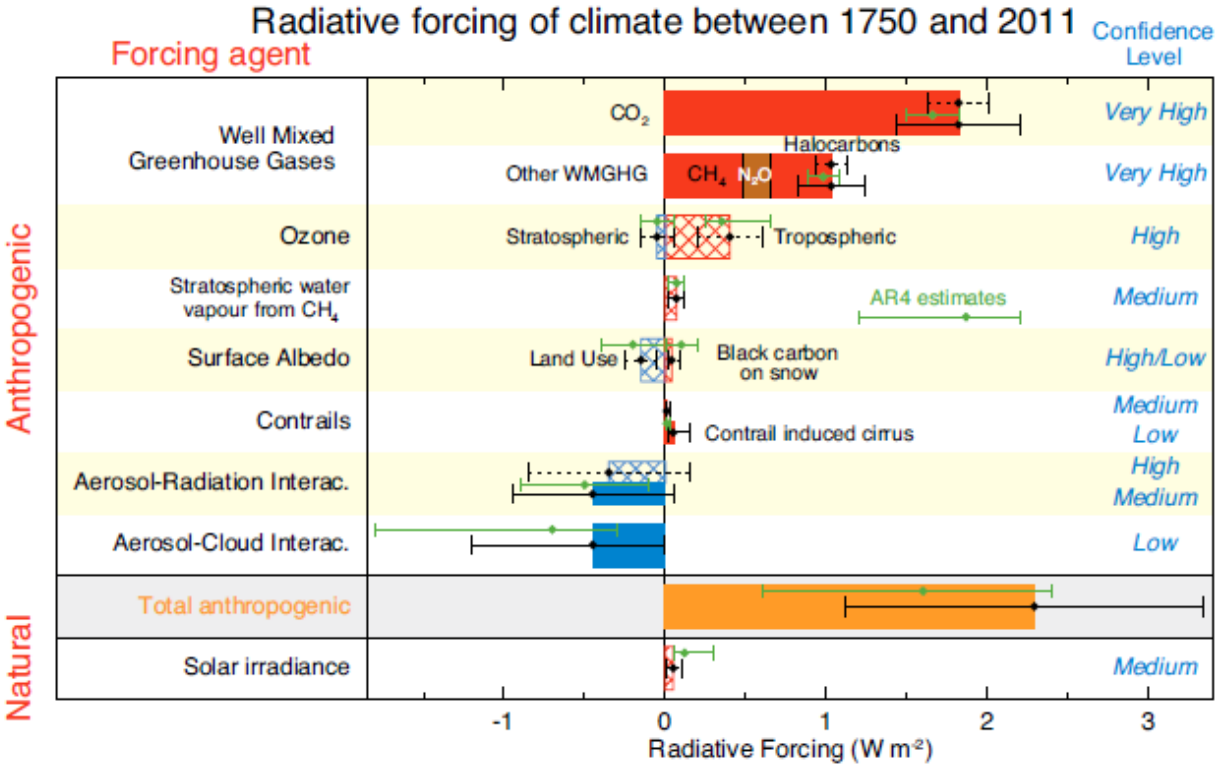

Figure 1.2: Estimations of radiative forcing for different atmospheric constituents and processes from IPCC 5th AR (Stocker et al., IPCC, 2013). The horizontal bars represent the values of radiative forcing and the thin black segments are the corresponding uncertainty ranges; green diamonds and associated uncertainties are referred to the estimations assessed in IPCC 4th AR (Forster et al., IPCC, 2007).

1.2 Droplet activation

Aerosol particles which are capable of initiating drop formation at supersaturation levels typical of atmospheric cloud formation (ranging between 0.01 % and 1 %, depending on cloud type) are called cloud condensation nuclei (CCN). CCN are those particles which have large enough radii and enough solute content to activate into droplets at a prescribed supersaturation.

Droplet activation is the most important and challenging effect in understanding aerosol-cloud interactions. It represents the direct microphysical link between aerosols and clouds, and it is at the heart of the indirect aerosol effects (Nenes and Seinfeld, 2003).

Cloud droplet activation is a highly complex and nonlinear process. Only a fraction of aerosol particles, depending on size distribution, chemical composition, and updraft velocity, can grow beyond their critical sizes to form droplets, while the not activated ones exist as interstitial particles (Ming Yi, et al., 2006).

In marine air, only about 50 % of all aerosol particles may be CCN for typical clouds, with supersaturations lower than 1% (Hegg and Hobbs, 1992). Typically, CCN are particles smaller than 0.2 µm, or about 1/100 the size of a cloud droplet on which water vapor condenses. Water requires a non-gaseous surface to make the transition from a vapor to a liquid; this process is called condensation. In the atmosphere, this surface presents itself as tiny solid or liquid particles called CCN. Clouds form when air containing water vapor and aerosol particles is cooled below the dew point. Water vapor condenses on aerosol particles. The equilibrium vapor pressure of water above a liquid water drop is controlled by Raoult's law (vapor pressure lowering by solute) and the Kelvin equation (free energy of surface tension) and is strongly a function of drop radius. The vapor pressure is given by the so-called Köhler (Köhler, 1936) equation for the water vapor pressure as a function of drop radius, which can be written as:

$$e = e_w exp\left[\frac{2M_w\sigma}{R_g T\rho a} - \frac{\nu m_s/M_S}{\left(\frac{4}{3}\pi a^3\rho - m_s\right)/M_w}\right] \quad (1.1)$$

where: e is the water vapor pressure in equilibrium with the drop, e_w is the saturation vapor pressure of water at the ambient temperature, M_W and M_S are the molecular weights of water and solute respectively, σ is the solution-air surface tension, Rg is the gas constant, T is the temperature, ρ is the solution density, a is the drop radius, v is the van' t Hoff factor (equiv / mol) including non ideality corrections and m_s is the solute mass.

In Köhler's theory, the "activation" of an aerosol particle to form a cloud droplet occurs when the environmental water vapor pressure exceeds maximum in Köhler equilibrium expression (critical supersaturation), with resultant condensation of water vapor, sufficiently long for the drop radius to exceed the corresponding critical radius. Once the drop is activated it grows under kinetic control. Activation is inherently kinetic, being controlled mainly by vapor-phase diffusion and heat transfer. All droplets with critical supersaturations below the maximum value of ambient saturation S can activate to cloud droplets, although the diffusional growth of droplets may be sufficiently slow that all droplets with critical supersaturations below S will not have time to activate (Jensen and Charlson, 1984; Nenes et al., 2001). The maximum value of S achieved in a rising air mass, as well as the number of activated droplets, results from a competition between the ambient cooling rate and condensational depletion of water vapor, which is affected by the number concentration, size distribution, and composition of the aerosol particles present.

Köhler's theory works well when the CCN are composed of a completely or fairly soluble solute and assumes that CCN are in thermodynamic equilibrium until the point of spontaneous growth. Moreover, it is assumed that a cloud forms only in a supersaturated water vapor environment, that is true for particles composed of completely soluble substances (with or without the presence of insoluble material), and that the number of activated particles is controlled strictly by meteorological factors, such as the rate at which a rising air parcel cools. However, it has recently become evident that chemical processes, compositional influences on physical properties, and kinetics also influence the formation of cloud droplets. These include the roles of insoluble particles (Kumar et al., 2009), soluble gases (Kulmala et al., 1993; Laaksonen et al., 1998), partially soluble solutes (Shulman et al., 1996), surface tension depression by organic substances (Facchini et al., 1999), aqueous-phase chemistry (Mattila et al., 2000), and slow condensation kinetics (Jensen and Charlson, 1984; Nenes et al., 2001). These processes necessitate a reshaping of the theory of cloud formation and suggest that additional information is needed to develop an ability to relate cloud droplet number concentration to the gases and aerosols in an increasingly anthropogenically perturbed atmosphere (Nenes, 2003). For example, a reshaping of Köhler's theory that describes droplet formation from insoluble but wettable particles, such as dust and black carbon, has been developed by Kumar (Kumar et al., 2009). The activation of these insoluble particles is treated by the Frenkel-Halsey-Hill (FHH) adsorption model (Sorjamaa and Laaksonen, 2007) in which water vapor is adsorbed onto the surface of insoluble particles. The equilibrium water vapor supersaturation, S, of a given insoluble particle is given by:

$$S = \frac{4M_w\sigma}{RT\rho_w D_p} - A_{FHH}\left(\frac{D_p - D_{dry}}{2D_w}\right)^{-B_{FHH}} \quad (1.2)$$

where: σ is the surface tension at the particle-gas interface, M_w is the molar mass of water, R is the universal gas constant, T is the temperature, ρ_w is the density of water, D_p is the equivalent particle diameter, D_{dry} is the dry particle diameter, D_w = 2.75 Å is the diameter of a water molecule adsorbed on the particle surface, A_{FHH} and B_{FHH} are empirical constants.

A_{FHH} characterizes interactions between the first monolayer of water molecules and aerosol surface. B_{FHH} characterizes the attraction between the aerosol surface and water molecules in subsequent layers; the smaller the value of B_{FHH}, the greater the distance at which the attractive forces act (Sorjamaa and Laaksonen, 2007). A_{FHH} and B_{FHH} are compound-specific

and determined experimentally. A_{FHH} has been experimentally found to range from 0.1 to 3.0, while B_{FHH} ranges from 0.5 to 3.0 (Sorjamaa and Laaksonen, 2007).

In both theories of droplet activation described above, during cloud formation the environmental supersaturation in a given air parcel typically exhibits a short transient maximum, triggered by initial adiabatic cooling and quenched by condensation of water vapor onto the newly available surface area of the activated cloud droplets, which serves as a runaway sink for water vapor. The time history of the saturation ratio depends intrinsically on the interaction of water vapor with aerosol and gaseous solutes. Cloud droplet activation determines the droplet number concentration and size distribution of the resultant cloud and the distribution of soluble gases taken up in the cloud water. The efficiency of activation of aerosol particles is of interest in cloud chemistry and microphysics. The efficiency of cloud droplet activation is a major influence on deposition of aerosol materials in rain.

1.3 Droplet activation in numerical models

Droplet activation in atmospheric models is simulated using various parameterizations, whose complexity range from simple empirical correlations to physically-based prognostic formulations.

The simplest parameterization that allows the analytic calculation of the number of activated particles was found by Twomey and Wojciechowski (Twomey and Wojciechowski, 1969). They measured the concentrations of activated CCN as a function of supersaturations in the atmosphere in a very comprehensive field campaign and parameterized the activated CCN concentration N_{CCN} with the following relation:

$$N_{CCN} = CS^K \tag{1.3}$$

where S (%) is the ambient supersaturation and C (cm^{-3}) and K are constant parameters characteristic of the atmosphere in which the measurement is performed. Another parameterization provides the maximum activable CCN concentration $N_{CCN_{max}}$ (Twomey, 1959):

$$N_{CCN_{max}} = C^{2/K+2}\left(\frac{6.9\times10^{-2}W^{3/2}}{K\beta\left(\frac{K}{2},\frac{3}{2}\right)}\right)^{2/K+2} \tag{1.4}$$

where C (cm^{-3}) and K are characteristic atmospheric parameters, W ($cm\ s^{-1}$) is the updraft velocity and β is the beta function. These parameterizations do not account for the dependence of droplet activation on the chemical composition and size distribution of aerosols and (1.3) takes no account even for dependence on updraft velocity of air parcels. As a consequence, the above-mentioned parameterizations are extremely limited in their applicability to the wide variety of conditions controlling droplet formation.

More advanced parameterizations (Abdul-Razzak and Ghan, 2000, 2002; Ekman et al., 2004), based on Kohler theory of the behavior of a solution droplet in equilibrium with the ambient water vapor field, take into account the chemical composition and size distribution of the aerosols. They consider a parcel of initially cloud-free air, rising adiabatically at constant speed. The model inputs include size distribution and chemical composition of aerosols, a spectrum of updraft velocities and thermodynamic properties, such as air temperature and pressure, at the cloud base. The size distribution is described by a mono-modal or multimodal lognormal size distribution, where each mode can have different internally mixed chemical composition; alternatively, the aerosol size distribution can be represented by a number of different size bins, with a uniform concentration and internally mixed chemical composition of particles in each bin, that is called "sectional representation" and allows for treatment of size distributions that diverge widely from lognormal distributions. The chemical composition for each aerosol type is taken into account via a hygroscopicity parameter, which is used in defining critical supersaturation as a function of radius for each particle (the more hygroscopic the particles, the lower the critical supersaturation for a given radius). The mass fraction of each aerosol type for each particle radius is also required to run the models. In order to account for the variability of updraft velocity within the turbulent, convective clouds, a spectrum of updraft velocities with mean and standard deviation is considered. The concentration of activated CCN is derived calculating the maximum supersaturation reached in the air parcel as it rises, assuming that the maximum supersaturation is the critical supersaturation for the smallest particle activated in each mode or size bin. This assumption should be valid if the chemical composition in each mode or size bin is homogeneous and the particles are all spherical.

The previous parameterizations, based on Kohler theory, have some issues. One of the assumptions of Kohler theory is that the solution drops are in equilibrium with the ambient water vapor field. It implies that the mass transfers from the aerosols to the ambient atmosphere and vice-versa are instantaneous. But the instantaneous equilibration of all the aerosol particles to any changes in supersaturation leads to a problem with the large aerosol particles. The water vapor absorbed by these large particles when they activate may be

larger than the total water vapor available at that point in the atmosphere (Chuang et al., 1997).

Furthermore, the assumption of equilibrium leads to a wrong estimation of the number of activated particles due to kinetic limitations of mass transfer between aerosols and ambient atmosphere as the aerosols grow by condensing water vapor from the ambient atmosphere (Nenes et al.,2001). According to Kohler theory, all the particles whose critical supersaturation is lower than the maximum the parcel has will activate immediately. But according to condensational growth theory, the time for which the particle encounters a supersaturation higher than its critical supersaturation is very important too. The aerosol must encounter such supersaturations long enough for the aerosol to grow to its critical size. Four different possible scenarios are identified:

- Aerosol particles whose equilibrium supersaturation decreases, after activation, and always remains lower than the parcel supersaturation. Thus, these particles always remain activated.
- Aerosol particles with a large dry diameter and, according to Kohler theory, low critical supersaturation S_c. These particles need very large times to reach equilibrium, do not have sufficient time to reach their critical diameter and hence cannot activate. But these particles continuously grow, because the parcel supersaturation S remains greater than S_c, and attain a wet diameter as large as other activated particles. Thus, these particles must be counted as activated.
- Aerosol particles with a high critical supersaturation S_c such that the time for which the parcel supersaturation S is greater than S_c is not sufficient for the particle to grow to its critical size. Thus, these particles initially grow as long as $S > S_c$, but when $S < S_C$ they start to evaporate.
- Aerosols which are activated initially, but during the evolution of the parcel supersaturation, this becomes lower than the equilibrium supersaturation of the particles and the particles start to evaporate. Thus, these droplets evaporate and the water vapor added to the ambient atmosphere allows the other particles to grow.

The experiments showed that because of these kinetic limitations, the equilibrium assumption over-estimates the cloud droplet number by less than 10% for pristine marine aerosol and by more than 40% for continental aerosols (Nenes et al.,2001).

Finally, processes of mass redistribution between the particles can occur due to various effects, such as different amounts of salt in the particles, different sizes of particles, radiative cooling or heating of the drops. For example, given two aerosol particles with different sizes,

the equilibrium vapor pressure over these particles is different because, by Kohler equilibrium theory, it depends on their sizes. Then, if the ambient supersaturation falls between the equilibrium supersaturations of these two particles, the smaller particle would evaporate while the larger one would grow. Thus, water molecules can be transferred from the smaller drops to the larger ones. Although these mass redistribution processes can be neglected for monodisperse aerosols, they become pronounced as the aerosol chemical composition and size distribution vary greatly.

To address some of the limitations discussed above, new parameterizations of aerosol activation, based on time-dependent calculation of mass transfer between aerosols and the ambient atmosphere, have been developed (Steele, 2004; Fountoukis and Nenes, 2005; Ming et al., 2006). These parameterizations are an extension of the previous ones, that compute the mass transfer to and from aerosols by solving a time-dependent diffusion equation, while taking into account the influence of gas kinetics on the water vapor diffusivity. This explicit computation of aerosol activation is expected to provide accurate prediction of cloud droplet number concentrations from aerosol size distribution and chemical composition.

The parameterizations of droplet activation are applied to global models, in order to quantify the aerosol indirect effects on the planetary energy balance, and to cloud-resolving models, in order to provide a computationally efficient way to predict supersaturation and cloud formation and evolution.

1.4 State of the art about the experimental study of aerosol-cloud interactions

Aerosol-cloud interactions, and in particular cloud droplet activation, are not yet accurately quantified and parameterized in numerical weather and climate models, because their experimental investigation is very difficult due to the complexity of the involved processes which take place in the atmosphere far away from the ground. However, the experimental investigation of these processes, based on accurate estimations of aerosols and cloud properties, is strongly needed in order to reliably evaluate ACI and cloud microphysics in numerical models and better quantify the impact of clouds on the Earth's climate due to the aerosol-cloud interactions, that is the aerosol indirect effects. "Disentangling" the effects of aerosols and meteorology on cloud radiative effects is a major challenge that prevents us

from quantifying the aerosol cloud-mediated climate forcing and therefore constitutes the largest source of uncertainty in anthropogenic climate forcing (Rosenfeld et al., 2014).

ACI have been examined empirically using several different variables to represent cloud microphysics (e.g., cloud optical depth, drop effective radius, drop number concentration) and various proxies for aerosol amount (e.g., aerosol optical depth, light scattering coefficient, CCN number concentration and size distribution). Additionally, these observations have been made from an array of different instruments that reside on various platforms or at the same observation station. Measurements are commonly made in situ at the surface or from aircraft and by ground-, aircraft-, and space-based remote sensing. All these measurements techniques have their advantages and limitations, but their synergetic use along with the development of new methodologies for the data exploitation can strongly contribute to the investigation of ACI.

Space-based remote sensing allow to study atmospheric variables at global scale, but ground-based observations are necessary for calibration and validation (GCOS, 2006). Upcoming satellite missions aim at showing the benefit coming from the availability of technological improvements and innovations. However, research is necessary to improve retrieval algorithms of atmospheric variables and to assess the real advances in the knowledge of weather and climate. Quality-controlled vertical profiles of atmospheric key variables provided by ground based advanced atmospheric observatories represent the optimal basis for the satellite calibration/validation programs. So far, atmospheric observatories are working towards the development of new observations strategies and the full exploitation of the synergy among active and passive profiling sensors. This is highly relevant for the new generation satellites equipped with multiple sensors on board the same observation platform. Ground-based observations provide long-term monitoring also of parameters that, at present, are challenging for space observations. For instance, the study of thin liquid water clouds as well as the mechanisms leading to droplet activation is challenging for satellite passive sensors, whereas they are important for weather and climate studies.

Moreover, the retrieval algorithms that can be applied to satellite measurements often need to be assessed on dedicated ground based platforms. For example, the CHASER (Clouds, Hazards, and Aerosols Survey for Earth Researchers) satellite mission (Rosenfeld et al., 2012; Rennó et al., 2013) aims to perform simultaneous measurements of CCN and cloud microphysical and dynamical properties from space, using the base of convective clouds as CCN chambers. Rosenfeld (2012) has shown how the number of activated CCN into cloud drops at the base of convective clouds (Na) is retrieved based on the high-resolution (375m)

satellite retrievals of vertical profiles of convective cloud drop effective radius (r_e). The maximum cloud base supersaturation (S) is calculated when Na is combined with radar-measured updraft and yields CCN, which was validated well against ground-based CCN measurements during the conditions of well-mixed boundary layer over the U.S. Department of Energy's Atmospheric System Research Southern Great Plains site.

Satellite retrieving Na is a new capability, which is one essential component of simultaneous measurements of cloud microstructure and CCN from space by using clouds as natural CCN chambers. Anyhow, a methodology for satellite estimates of cloud base updraft is not yet been developed and demonstrated. Therefore, ground based remote sensing is the ideal platform where to test the algorithms to be implemented for the retrieval of parameters from satellite sensors. This implies the need of investigating extensive datasets for those parameters that might act as a proxy for the study of the interaction between aerosol and cloud layers.

Although the different measurement techniques are complementary, differences in perspective as well as mismatched sampling in space and time will result in variability and uncertainties in the characterization of ACI, that should be well assessed before each specific study. For a wide range of aerosol concentrations and cloud liquid water, local radiative forcing (under conditions of total cloud cover) can range from approximately 1 to 60 W m^{-2} (McComiskey and Feingold, 2008, 2012). Understanding the relationships among these various measurements is a mandatory first step toward understanding the natural variability of the processes in different environmental conditions as distinct from measurement uncertainty. A quantitative characterization of ACI on process level scales is necessary for reducing the uncertainty in associated radiative forcing estimated by global-scale climate models. For example, the quantification of the albedo effect as it varies under different environmental conditions and with different observational approaches is not well characterized. This results in persistent and large uncertainties in radiative forcing (Ramanathan et al., 2001; Feingold et al., 2003; Twohy et al., 2005, and references therein; Kim et al., 2008).

Therefore, a big challenge is now to understand to what extent various measures of ACI are robust and consistent and which are the factors affecting the magnitude of ACI (e.g., cloud type, water phase, dynamics, aerosol composition and size). Moreover, it is needed to assess if the variability in metrics of ACI found in the literature is due to physical processes, measurement uncertainties, observational approaches, or a combination of all of these.

1.5 Summary of the content

In this work, a new methodology for experimental investigation of droplet activation, based on ground-based multi-wavelength Raman lidar and Doppler radar techniques, is presented. The study is focused on the characterization of thin liquid water clouds, which are low or midlevel super-cooled clouds characterized by a liquid water path (LWP) less than about 100 gm^{-2} (Turner et al., 2007). These clouds contribute for more than one third to the global mean cloud coverage (Rossow and Shiffer, 1999) and are often optically thin (i.e. cloud optical depth is lower than 3), which means that ground-based Raman lidar and Doppler radar allow the cloud top detection and the full profiling throughout cloud layers with high vertical and temporal resolution.

20 case studies with the presence of optically thin liquid clouds have been selected for this study. In particular, clouds with a *"*broken*"* structure are considered, where *"*broken*"* refers to single layer clouds with a not homogeneous horizontal structure, characterized by cloud fields separated by cloud-free regions.

The vertical profiles of extensive optical properties (extinction and backscattering coefficients) and water vapor content (water vapor mixing ratio and relative humidity) are retrieved in cloudy regions and in surrounding cloudless regions, with high vertical resolution, in the order of 100 m. The extinction coefficient profiles in cloudy regions are corrected for multiple scattering.

Several properties of cloud layers, such as their geometrical and optical depth, the height and temperature of their base and top, the cloud LWP have been estimated with good agreement with the cloud products obtained from Cloudnet algorithms. In particular, the estimation of the cloud base and cloud top heights has been compared with the Cloudnet products (Hogan and O'Connor, 2006).

The type and source of aerosol in cloud-free regions surrounding the clouds have also been identified from the analysis of air mass back-trajectories, provided by Hysplit model (Draxler and Rolph, 2014; Rolph, 2014), along with the values of the aerosol intensive optical properties (i.e. lidar ratios and Ångström exponents). Furthermore, the microphysical properties of aerosol in cloud-free regions surrounding the clouds are retrieved from the vertical profiles of multi-wavelength aerosol extensive optical properties, using the algorithm developed by Veselovskii et al. (2004). Aerosol microphysical properties include the size distribution and the complex refractive index.

A statistical study of the variability of optical properties and humidity in the transition from cloudy regions to cloud-free regions surrounding the clouds is presented and discussed.

From this study, threshold values of optical properties that allow to discriminate between cloudy and cloudless regions are identified. These values can be used to directly evaluate and improve the ability of cloud numerical models to predict the formation of liquid water clouds, using ground-based Raman lidar measurements of extinction and backscattering coefficients. This evaluation also implies an indirect validation of droplet activation parameterizations used in cloud models.

The moments of the radar Doppler spectra are analyzed to estimate droplet sizes as well as updrafts and downdrafts in cloudy regions, with the aim to correlate them to the aerosol microphysical and optical properties.

Finally, a correlation between the effective radius of aerosols in cloud-free regions surrounding the clouds and droplet updrafts and downdrafts close to the cloud base is found.

The presented methodology and results for thin liquid clouds can be applied for future research to improve our understanding of ACI, and particularly, cloud droplet activation. For ACI, correlations between cloud optical depth and aerosol optical (optical depth, lidar ratio) and microphysical (effective radius, number concentration) properties in proximity of clouds can be investigated; moreover, from cloud optical depth and LWP it is possible to retrieve cloud microphysical properties (effective radius and number concentration of droplets) and relate them to the aerosol optical and microphysical properties. This will be considered in the follow-up of this work.

For droplet activation, it is possible to directly validate the parameterizations used in the models, by applying them to the thin liquid clouds considered in this study. Indeed, the presented methodology allows to derive aerosol optical and microphysical properties and aerosol type in proximity of the clouds, cloud optical and microphysical properties, as well as information on the updraft speed and atmospheric thermodynamic properties at the cloud base. All these parameters contain information on the input and output (droplet concentration) data used in droplet activation parameterizations, as well as on diagnostic or prognostic variables of global, regional or cloud-resolving numerical models to which these parameterizations are applied. Therefore, these parameterizations and numerical models can be directly validated and improved.

The presented methodology is a good alternative to in situ measurements from aircraft in order to investigate ACI. These measurements are able to provide cloud and aerosol microphysics observations as well as atmospheric state observations (turbulence, temperature, and water vapor content), but they are still very expensive and limited in time and space sampling.

On the other hand, the other surface and satellite remote sensing techniques are not currently able to provide the estimation of the same aerosol and cloud properties, with the same precision. For example, Cloudnet cannot provide aerosol extinction coefficient and microphysical properties. The resolution of most conventional satellite passive sensors [e.g., Moderate Resolution Imaging Spectrometer (MODIS)] is too low to retrieve the properties of thin liquid clouds because of their small sizes (Dey et al., 2008), which prevents the acquisition of the long-term statistics needed to evaluate cloud parameterizations and numerical models; moreover, if retrieved, cloud droplet size and optical depth are typically biased (Marshak et al., 2006). Space-based lidars [e.g. Cloud–Aerosol Lidar and Infrared Pathfinder Satellite Observations (CALIPSO)] provide the profiles of optical properties for aerosols and clouds, but these profiles are retrieved from elastic backscatter lidar, with assumptions or parameterizations of lidar ratio constructed using ground-based lidar or sun photometer measurements (Winker et al., 2009; Young and Vaughan, 2009). This can result in large biases in the retrieval of particle optical properties and ACI.

The thesis is organized as follows.

Chapter 2 describes the remote sensing techniques, the instruments and the algorithms considered in this work. Particular attention is devoted to the lidar systems and their algorithms, used to retrieve the optical properties of aerosols and clouds and the atmospheric water vapor content, and to the Doppler radar, used for the retrieval of vertical wind.

Chapter 3 describes the methodology used for the analysis and processing of lidar, radar and microwave radiometer data, in order to determine the geometrical and optical properties of aerosols and clouds. A case study is also discussed.

Chapter 4 describes the results obtained from the analysis of 20 selected case studies. A new approach to estimate cloud boundaries from Raman lidar signals is compared to the corresponding estimations provided by Cloudnet. A statistical study of the variability of optical properties and humidity in the transition from cloudy regions to cloud-free regions is presented and discussed. This study leads to identify threshold values for the optical properties, that allow the discrimination between cloudy and cloudless regions. A statistical study of the moments of the radar Doppler spectrum is also reported, to characterize droplet size and updrafts and downdrafts close to the cloud base. Chapter 4 ends discussing the correlation between the effective radius of aerosols in cloudless regions surrounding the clouds and cloud updrafts and downdrafts close to the cloud base.

The thesis closes with a summary of the results and perspectives for future research.

CHAPTER 2

INSTRUMENTS AND ALGORITHMS

The research activity described in this work has been carried out at the Istituto di Metodologie per l'Analisi Ambientale of the Italian National Research Council (CNR-IMAA), where an advanced atmospheric observatory is operative. The CNR-IMAA Atmospheric Observatory (CIAO) is equipped with state-of-the-art techniques and instruments for the ground-based remote sensing of the atmosphere, including active and passive sensors, like lidars, ceilometers, radiometers, and a cloud radar, as well as surface meteorological and radiation sensors. CIAO is able to provide vertical profiles of aerosol, water vapor and cloud properties with high time-space resolution and high accuracy. Therefore, CIAO historical data archive represents an optimal basis to study ACI and droplet activation. In the following, the CIAO infrastructure with its instruments and algorithms is described.

2.1 CIAO

The CNR-IMAA Atmospheric Observatory (CIAO) is located in Tito Scalo, 6 km far from Potenza, Southern Italy, on the Apennine mountains (40.60 N, 15.72 E, 760 m a.s.l.) and less than 150 km far from the West, South and East coasts. The site is in a plain surrounded by low mountains (<1100 m a.s.l.). The observatory operates in a typical mountain weather strongly influenced by Mediterranean atmospheric circulation, resulting in generally dry, hot summers and cold winters. In this location phenomena like orographically-induced effects on cloud formation can be studied. The site is representative of the Mediterranean area and is affected by a large number of Saharan dust intrusions each year.

CIAO is a well-established ground-based remote sensing observatory for the study of weather and climate, the largest in the Mediterranean Basin. The observatory consists of a combination of advanced systems able to provide high-quality long-term properties of aerosol and clouds. Since 2000, systematic observations of aerosol, water vapor and clouds

have been collected and the acquisition of new active and passive microwave profilers has strengthened the equipment required for performing accurate aerosol and cloud observations.

CIAO whole facility is distributed within an area of about 200 m^2 and the problem of the co-location of atmospheric observations is not so relevant (see Figure 2.1).

At CIAO large attention has been traditionally paid to the study of aerosol and water vapor using lidar techniques (Pappalardo et al., 2004a, b, 2010; Mona et al., 2006, 2007, 2009). However, since 2004 the facility strengthened its observing capability for the monitoring of clouds through the acquisition of new active and passive microwave profilers, with the main objective to investigate aerosol-clouds interactions using both active and passive remote sensing techniques. The wide range of measurements provided at the facility makes it an ideal site for calibration, validation and intercomparison campaigns. All the observations performed at CIAO are designed in order to be redundant, traceable and to follow the main international standards, provided by the WMO and other research programs. CIAO equipment addresses the state-of-the-art for the ground based remote sensing of aerosol, water vapor and clouds including active and passive sensors, like lidars, ceilometers, radiometers, and radar, as well as two radiosounding systems, surface weather stations, radiation sensors and a sky camera.

CIAO is also equipped with a data center hosting several advanced calculus machines and a data storage with a capacity of 20 Tb, probably to be extended in the near future.

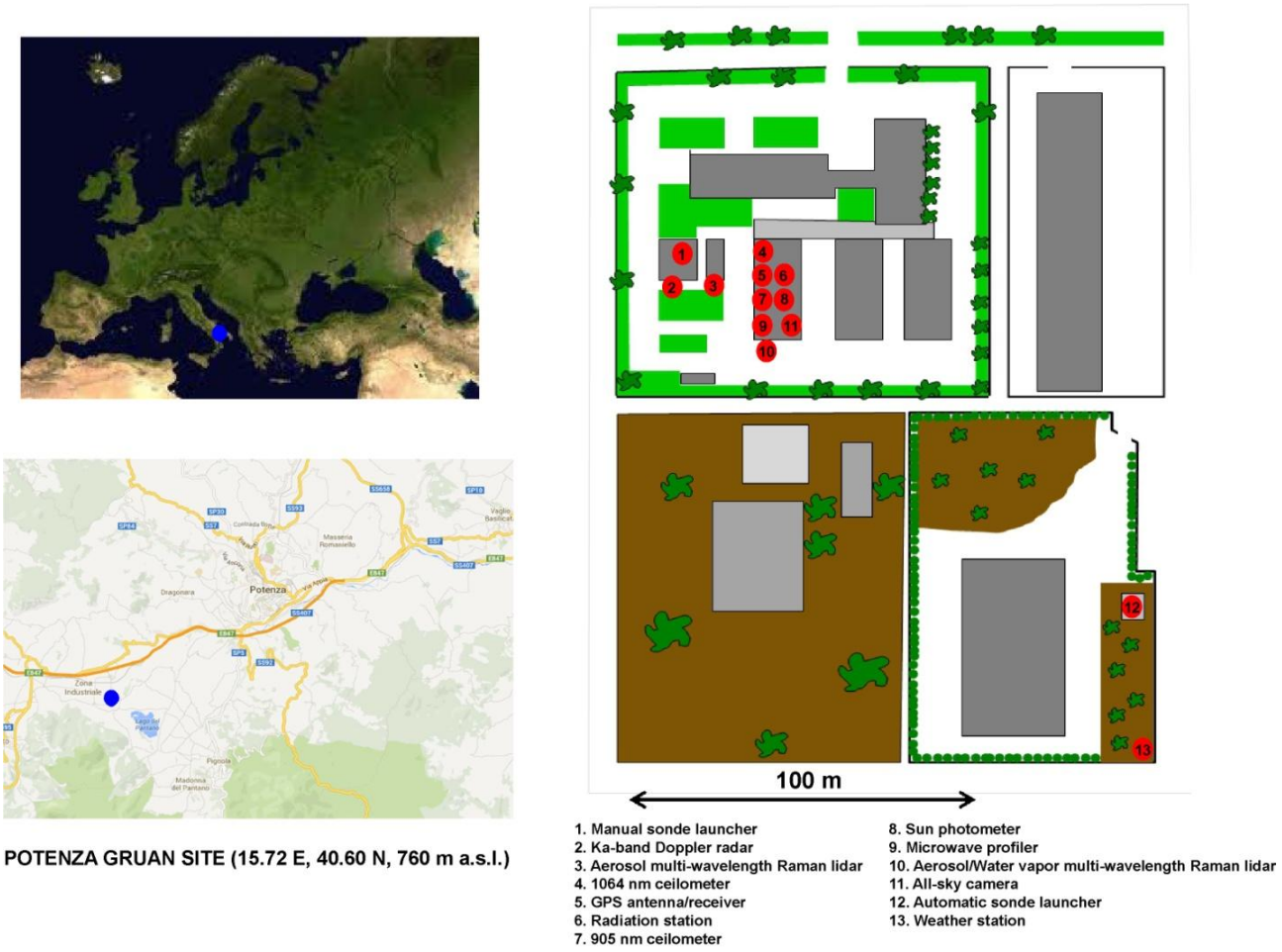

Figure 2.1: The Potenza GRUAN (GCOS Upper-Air Reference Network – www.gruan.org) Site

2.2 Lidars

Since 1993, lidar remote sensing of the atmosphere is one of the main research activities carried out at CIAO. Currently, two lidar systems are operative at CIAO, devoted to the study of aerosol, water vapor and clouds. These lidar systems have been designed and implemented by the observatory team. The multi-wavelength lidar system for tropospheric aerosol characterization, PEARL (Potenza EArlinet Raman Lidar), operative at CIAO since August 2005 (Mona et al., 2006, 2009), has been designed to provide simultaneous multi-wavelength aerosol measurements for the retrieval of optical and microphysical properties of the atmospheric particles (Ackermann et al., 1998; Müller et al., 2001) and water vapor mixing ratio profiles. This system is the result of the upgrade of a pre-existing lidar system, operative since May 2000 in the frame of EARLINET (Bösenberg et al., 2001). The system is

based on a 50 Hz Nd:YAG laser source emitting at 1064 nm and equipped with second and third harmonic generators. An optical system, based on mirrors, dichroic mirrors and 2X beam expanders, separates the three wavelengths allowing to optimize the laser beam power and divergence for each wavelength. The beams are mixed again in order to get the collinearity of the three wavelengths and to transmit them simultaneously and coaxially with respect to the lidar receiver, a F/10 Cassegrain telescope with a primary mirror of 0.5 m diameter and an equivalent focal length of 5 m. The backscattered radiation from the atmosphere is collected by the telescope and forwarded to the receiving system, equipped with 16 optical channels. Three channels are devoted to the detection of the radiation elastically backscattered from the atmosphere at the three laser wavelengths (355 nm, 532 nm and 1064 nm). Three channels detect the Raman radiation backscattered from the atmospheric N_2 molecules at 387 nm and 607 nm, and H_2O molecules at 407 nm. Two further channels detect the polarized components of the 532 nm backscattered light (perpendicular and parallel with respect to the direction of the linearly polarized beam transmitted by the laser at 532 nm). Each of all these channels is further split into two channels differently attenuated for the simultaneous detection of the radiation backscattered from the low and high altitude ranges, in order to extend and optimize the dynamic range of the system. The spectral selection of the collected radiation is performed by means of dichroic mirrors and interference filters. Interference filter bandwidths is 0.5 nm at all the wavelengths for both night-time and daytime operations. For the elastic backscattered radiation at 1064 nm the detection is performed by using an avalanche photodiode detector (APD) and the acquisition is performed in analog mode. For all the other acquisition channels, the detection is performed by means of photomultiplier tubes (PMT) and the acquisition is in photon counting mode. PEARL performs systematic measurements two times per week in the frame of EARLINET (Pappalardo et al., 2010), and during international experiments or special atmospheric events (saharan dust outbreaks, volcanic eruptions, etc.). The raw vertical resolution of the lidar signals is 7.5 m for 1064 nm and 15 m for the other wavelengths, while the raw temporal resolution is 1 min. The optical configuration of the system is given in Figure 2.2, while the main specifications are listed in Table 2.1.

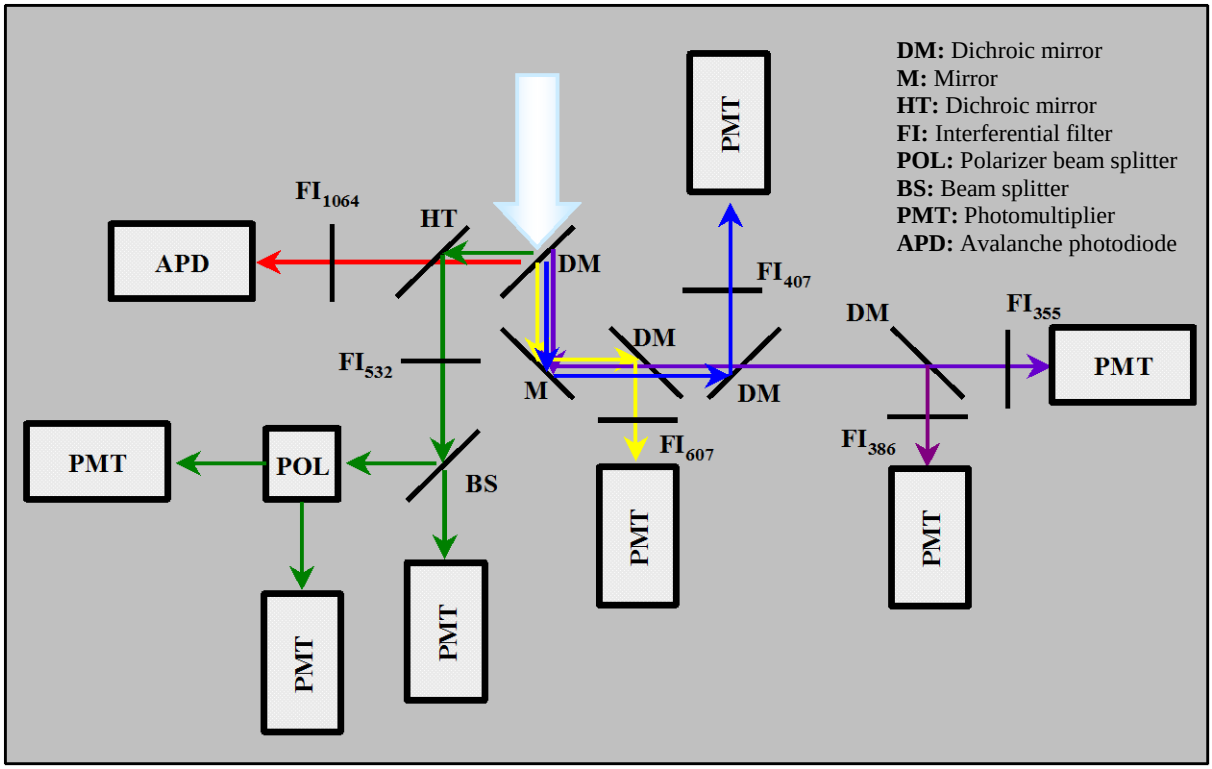

Figure 2.2: Optical layout of PEARL system

LASER: ND:YAG (Continuum Powerlite Precision II 9050)
Max. pulse energy : 1200mJ @1064nm
600mJ @532nm
350mJ @355nm
Max. repetition rate 50Hz
Beam divergence 0.25 mrad
(beam expander 2X with remixing)

RECEIVER: Cassegrain Telescope
Diameter of the primary mirror 0.5 m
Combined focal length 5 m
Nighttime field of view 1 mrad
Achromatic lens Ø=2", f=50cm

CHANNEL SELECTION
Interference filters (FI), bandwidth 0.5 nm
Polarizer beam splitter (BK7) a 532 nm (POL)
Dichroic mirrors (DM e HT)
Selection of high and low altitude channels

ACQUISITION
Fotomultipliers (PMT) THORN EMI
9202QA 532, 532⊥, 532∥, 607 nm
9893/350B 355, 386 nm
EG&G MCS – PCI (100ns min dwell time, 150MHz photon counting)
APD 1064 nm Licel Transient recorder (12bit 20 MHz analogic, 250 MHz photoncounting)

Operational since 2000 (upgrade in 2005 of a pre-existing lidar system)

Table 2.1: Main specifications of PEARL system

MUSA (Multi-wavelength System for Aerosol) is a mobile multi-wavelength lidar system based on a 20 Hz Nd:YAG laser emitting at 1064 nm and equipped with second and third harmonic generators and on a F/3 Cassegrain telescope with a primary mirror of 30 cm diameter and an equivalent focal length of 95 cm. The three laser beams at 1064, 532 and 355 nm are simultaneously and coaxially transmitted into the atmosphere in a bistatic configuration. As for PEARL, the receiving system has 3 channels for the detection of the radiation elastically backscattered from the atmosphere and 2 channels for the detection of the Raman radiation backscattered by the atmospheric N_2 molecules at 607 and 387 nm. The elastic channel at 532 nm is split into parallel and perpendicular polarization components by means of a polarizer beam splitter cube. The backscattered radiation at all the wavelengths is acquired both in analog and photon counting mode. The typical raw vertical resolution of the lidar signals is 3.75 m with a raw temporal resolution of 1 min. The system is compact and transportable. MUSA has been developed in cooperation with the Meteorological Institute of the Ludwig-Maximilians-Universität of Munich and it is one of the reference systems used in the frame of the EARLINET Quality Assurance program. The optical configuration of MUSA is given in Figure 2.3, while the main specifications are listed in Table 2.2.

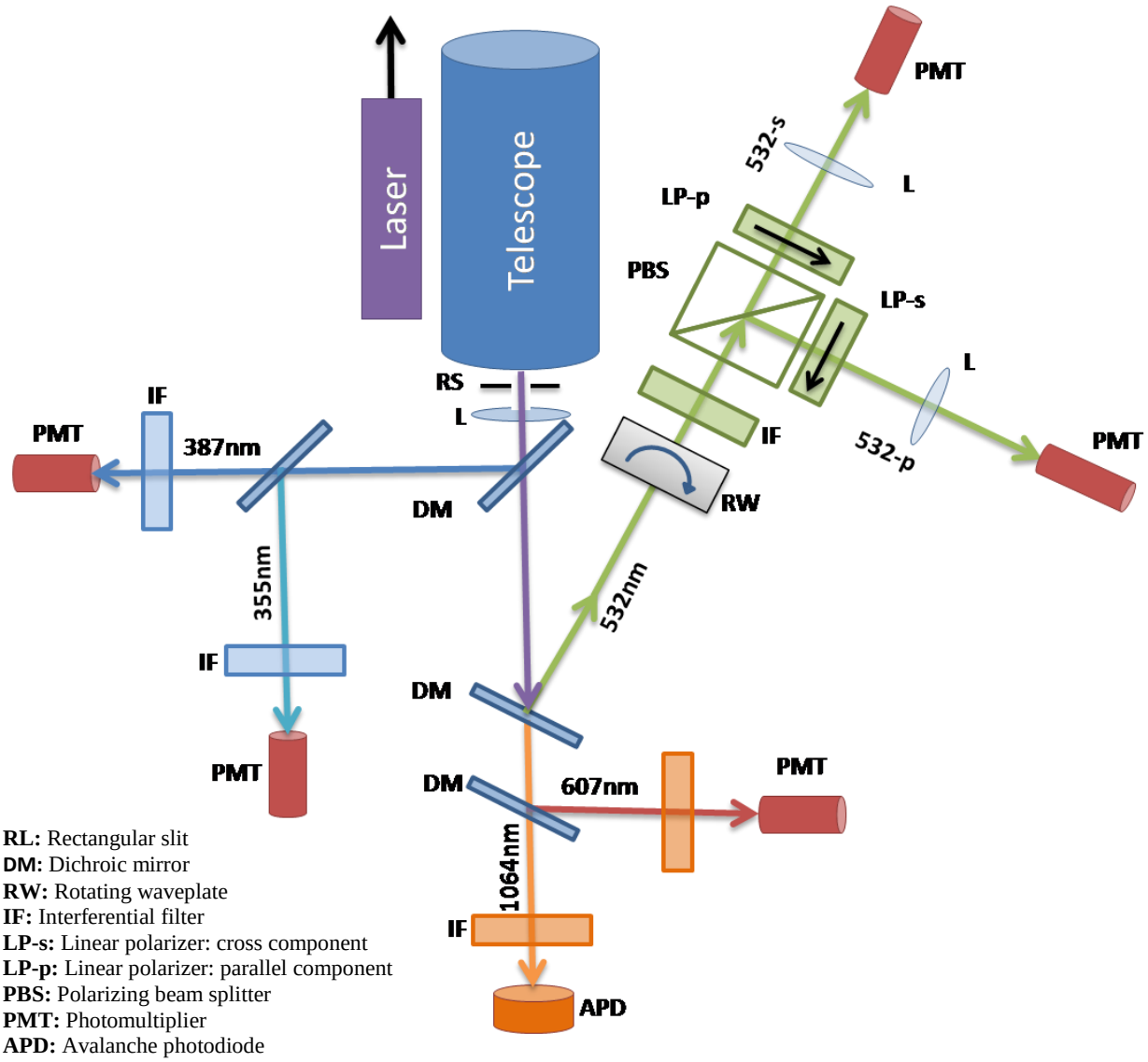

RL: Rectangular slit
DM: Dichroic mirror
RW: Rotating waveplate
IF: Interferential filter
LP-s: Linear polarizer: cross component
LP-p: Linear polarizer: parallel component
PBS: Polarizing beam splitter
PMT: Photomultiplier
APD: Avalanche photodiode

Figure 2.3: Optical layout of MUSA system

LASER: ND:YAG (Continuum Surelite II-20)	
Max. pulse energy :	550mJ @1064nm
	250mJ @532nm
	120mJ @355nm
Max. repetition rate	20Hz
Beam divergence	0.6 mrad
RECEIVER: Cassegrain Telescope	
Diameter of the primary mirror	0.3 m
Combined focal length	950 mm
Nighttime field of view	1 mrad
Achromatic lens	Ø=9mm, f=100mm
CHANNEL SELECTION	
Interference filters (FI), bandwidth 0.5 nm	
Polarizer beam splitter (BK7) at 532 nm (POL)	
Dichroic mirrors (DM e HT)	
ACQUISITION	
Fotomultipliers (PMT), Hamamatsu	
R7400P-06	355, 387, 532⊥, 532∥ nm
R7400U-20	607nm
APD	1064nm
Licel Transient recorder (12bit 40 MHz analogic, 250 MHz photoncounting)	
Operational since April 2009	

Table 2.2: Main specifications of MUSA lidar system

2.3 Optical properties of aerosol and clouds

Both MUSA and PEARL allow independent measurements of extensive optical properties of aerosols and clouds. These properties depend on both the nature and amount of the particles and are the extinction coefficient and backscattering coefficient.

The extinction coefficient $\alpha_\lambda(z)$ at a given wavelength λ is a measure of attenuation of the light passing through the atmosphere due to the scattering and absorption by particles and molecules. It is the fractional depletion of radiance per unit path length and has units of m^{-1}. The extinction coefficient is a combination of the scattering coefficient α_λ^s and the absorption coefficient α_λ^a of molecules (mol) and particles (par):

$$\alpha_\lambda(z) = \alpha_\lambda^{s,mol}(z) + \alpha_\lambda^{s,par}(z) + \alpha_\lambda^{a,mol}(z) + \alpha_\lambda^{a,par}(z) \qquad (2.1)$$

where z is the altitude range and lidar is pointing in the zenith viewing direction.

The backscattering coefficient $\beta_\lambda(z)$ is a measure of the scattering in the backward direction (i.e. towards the incident direction, at a scattering angle of 180°) for the light encountering the atmospheric particles and molecules.

The backscattering coefficient for elastic signals, i.e. at the same wavelength of incident light ($\lambda = \lambda_0$), can be summed up from the backscattering coefficients of molecules and particles:

$$\beta_{\lambda_0}(z) = \beta_{\lambda_0}^{mol}(z) + \beta_{\lambda_0}^{par}(z) \tag{2.2}$$

The backscattering coefficients of the molecular atmosphere as well as of the aerosol or cloud particles can be calculated from the number density of the scatterers $N^{mol/par}$, their scattering cross-section $\sigma_{\lambda_0}^{mol/par}$ and the phase function $\Phi_{\lambda_0}^{mol/par}(\theta)$ for the scattering angle of 180° ($\theta = \pi$):

$$\beta_{\lambda_0}^{mol/par} = N^{mol/par}\sigma_{\lambda_0}^{mol/par}\Phi_{\lambda_0}^{mol/par}(\pi) \tag{2.3}$$

A variable often used to describe aerosol and clouds properties is the optical depth of an aerosol or cloudy layer, defined as the integral of the particle extinction coefficient over the altitude range from the base to the top of the layer:

$$\tau = \int_{base}^{top} \alpha^{par}(z)dz \tag{2.4}$$

From particle extensive optical properties other optical parameters, used to describe aerosol and clouds, are derived. These are the intensive optical properties, which are independent of amount of particles, depending only on the nature of the specific type of particle.

The particle lidar ratio is defined as the ratio of the particle extinction coefficient and the particle backscattering coefficient:

$$S_{\lambda_0}^{par}(z) = \frac{\alpha_{\lambda_0}^{par}(z)}{\beta_{\lambda_0}^{par}(z)} \tag{2.5}$$

The lidar ratio profile can be derived only from profiles of $\alpha_{\lambda_0}^{par}(z)$ and $\beta_{\lambda_0}^{par}(z)$ determined in an independent way and with the same time and height resolutions.

The Ångström exponent å, as introduced for the first time (Ångström, 1929), describes the wavelength dependence of optical depths by the following relation:

$$\frac{\tau(\lambda_1)}{\tau(\lambda_2)} = \left(\frac{\lambda_2}{\lambda_1}\right)^{å} \tag{2.6}$$

where $\tau(\lambda_1)$ and $\tau(\lambda_2)$ are the optical depths relative to wavelengths λ_1 and λ_2. From multi-wavelengths Raman lidar observations we can derive extinction-related Ångström exponents:

$$\text{å}_\alpha(z) = ln\left(\frac{\alpha_{\lambda_1}^{par}(z)}{\alpha_{\lambda_2}^{par}(z)}\right)/ln\left(\frac{\lambda_2}{\lambda_1}\right) \quad (2.7)$$

and backscatter-related Ångström exponents:

$$\text{å}_\beta(z) = ln\left(\frac{\beta_{\lambda_1}^{par}(z)}{\beta_{\lambda_2}^{par}(z)}\right)/ln\left(\frac{\lambda_2}{\lambda_1}\right) \quad (2.8)$$

where $\alpha_{\lambda_1}^{par}(z)$ and $\alpha_{\lambda_2}^{par}(z)$ are the particle extinction profiles at wavelengths λ_1 and λ_2, while $\beta_{\lambda_1}^{par}(z)$ and $\beta_{\lambda_2}^{par}(z)$ are the particle backscattering profiles at wavelengths λ_1 and λ_2. As the lidar ratio, the Angström exponents are not dependent on the particle concentration, but they are related to aerosol microphysical properties. They are inversely proportional to the particle sizes and depend on the complex refractive index of the particles.

2.4 Lidar retrieval algorithms

The basic equation for the analysis of lidar signals is the so-called lidar equation, that describes the intensity of the signal collected by the lidar receiver depending on range z, several system parameters as well as on atmospheric parameters. In order to retrieve the atmospheric parameters by lidar equation, the approximation of single and independent scattering is needed. This means that a photon is scattered only once by the atmospheric constituents and that these are adequately separated and are randomly moving. Thus, the contributions to the total scattered energy by many targets have no phase relation and the total intensity is simply the sum of the intensities scattered from each target. In this case, the lidar equation can be written as:

$$P(\lambda_L, \lambda_S, z) = P_L(\lambda_L)\frac{c\,\tau_d}{2}\frac{A}{z^2}\Psi(\lambda_S, \lambda_L)O(z)\beta(\lambda_S, \lambda_L, z)T(\lambda_L, z)T(\lambda_S, z) + P_B \quad (2.9)$$

where: $P(\lambda_L, \lambda_S, z)$ is the backscattered power received from the distance z from the laser source (zenith pointing), at a specific polarization and wavelength λ_S, due to the scattering of the laser wavelength λ_L; $P_L(\lambda_L)$ is the mean output laser power per pulse; $c\tau_d/2$ represents the sounding vertical resolution, where c and τ_d are respectively the light speed

and the dwell time (i.e. the duration of a laser pulse); A/z^2 is the probability that a photon scattered from the distance z is collected by the receiving telescope of surface A; $\Psi(\lambda_S, \lambda_L) = \xi(\lambda_L, \lambda_S)\eta(\lambda_S)$ is transmission of the lidar receiver, where $\xi(\lambda_L, \lambda_S)$ is the optical efficiency of the lidar receiver, including such factors as the reflectivity of the telescope and the transmission of the conditioning optics, while $\eta(\lambda_S)$ is the quantum efficiency of the receiver and detection parts; $\mathrm{O(z)}$ is the system overlap function, that describes the incomplete overlap between the emitted laser beam and the receiver field of view near the ground (above a certain height z_{ovl} the overlap is complete and O(z) is defined to be 1); $\beta(\lambda_S, \lambda_L, z)$ is the volume backscattering coefficient at the distance z and wavelength λ_S, representing the probability that a photon transmitted at the laser wavelength λ_L is backscattered by the atmosphere into a unit solid angle; $\mathrm{T}(\lambda_L, z)$ and $\mathrm{T}(\lambda_S, z)$ are the one-way transmissivities of the light from laser source to the distance z at wavelength λ_L and from distance z to the receiver at wavelength λ_S, respectively; these terms can be expressed as:

$$\mathrm{T}(\lambda_L, z) = exp\left(-\int_0^z \alpha_{\lambda_L}(z')dz'\right) \quad \text{and} \quad \mathrm{T}(\lambda_S, z) = exp\left(-\int_0^z \alpha_{\lambda_S}(z')dz'\right) \tag{2.10}$$

where $\alpha_{\lambda_L}(z)$ and $\alpha_{\lambda_S}(z)$ are the extinction coefficients at wavelengths λ_L and λ_S as a function of range z along the path of the laser beam, including scattering and absorption effects by molecules and aerosols. Finally, P_B is the contribution to the power return due to the background photons.

2.4.1.Optical properties

The vertical profiles of particle extinction coefficient at 355 and 532 nm are directly derived from the nitrogen Raman signals at 387 and 607 nm, respectively, by the following equation (Ansmann et al., 1990; Pappalardo et al., 2004b):

$$\alpha_{\lambda_L}^{par}(z) = \frac{\frac{d}{dz}\left\{ln\left[N(z)/P_{\lambda_R}(z)z^2\right]\right\} - \alpha_{\lambda_L}^{mol}(z) - \alpha_{\lambda_R}^{mol}(z)}{1 + (\lambda_L/\lambda_R)^{å}} \tag{2.11}$$

where: $\alpha_{\lambda_L}^{par}(z)$ is the particle extinction coefficient at the laser wavelength λ_L (355 or 532 nm) and range z; $P_{\lambda_R}(z)$ is the power of the nitrogen Raman lidar signal at wavelength λ_R (387 or 607 nm) and range z; $N(z)$ is the number density of atmospheric nitrogen molecules

at range z; $\alpha_{\lambda_L}^{mol}(z)$ and $\alpha_{\lambda_R}^{mol}(z)$ are the molecular extinction coefficients at wavelengths λ_L and λ_R , respectively; å is the Ångström exponent, that describes the wavelength dependence of particle extinction coefficient. It is defined by the following relation:

$$\frac{\alpha_{\lambda_L}^{par}(z)}{\alpha_{\lambda_R}^{par}(z)} = \left(\frac{\lambda_R}{\lambda_L}\right)^{å} \tag{2.12}$$

The Ångström exponent å is not known and has to be estimated. Typical values are in the range from - 0.5 to 2.5. The fixed value of å = 1 is used to retrieve the extinction coefficient. The relative errors of α^{par} due to overestimation and underestimation of the å value by 0.5 are of the order of 5% (Ansmann et al., 1992a). $\alpha_{\lambda_L}^{mol}(z)$ and $\alpha_{\lambda_R}^{mol}(z)$ can be calculated from Rayleigh scattering coefficients and atmospheric number density profiles retrieved from models or radiosonde measurements.

The vertical profiles of particle backscattering coefficients at 355 and 532 nm are derived from the particle extinction coefficients and the elastically backscattered signals at 355 and 532 nm, combined with the corresponding nitrogen Raman signals at 387 and 607 nm (Ansmann et al., 1992a; Pappalardo et al., 2004b):

$$\beta_{\lambda_L}^{par}(z) = -\beta_{\lambda_L}^{mol}(z) + \left[\beta_{\lambda_L}^{par}(z_{ref}) + \beta_{\lambda_L}^{mol}(z_{ref})\right] \frac{O_{\lambda_R}(z) P_{\lambda_R}(z_{ref}) P_{\lambda_L}(z) \beta_{\lambda_L}^{mol}(z)}{O_{\lambda_L}(z) P_{\lambda_L}(z_{ref}) P_{\lambda_R}(z) \beta_{\lambda_L}^{mol}(z_{ref})} \exp(C) \tag{2.13}$$

$$C = \left[1 - \left(\frac{\lambda_L}{\lambda_R}\right)^{å}\right] \int_{z_{ref}}^{z} \alpha_{\lambda_L}^{par}(z')dz'$$

where: $\beta_{\lambda_L}^{par}(z)$ and $\beta_{\lambda_L}^{mol}(z)$ are the backscattering coefficients of particles and molecules at the laser wavelength λ_L (355 or 532 nm); $P_{\lambda_L}(z)$ is the power of the elastic lidar signal at wavelength λ_L ; $P_{\lambda_R}(z)$ is the power of the nitrogen Raman lidar signal at wavelength λ_R (387 or 607 nm); $O_{\lambda_L}(z)$ is the overlap function of the elastic channel at wavelength λ_L ; $O_{\lambda_R}(z)$ is the overlap function of the Raman channel at wavelength λ_R ; z_{ref} is a reference altitude where the scattering due to particles can be neglected compared to the scattering from molecules $\left[\beta_{\lambda_L}^{par}(z_{ref}) \ll \beta_{\lambda_L}^{mol}(z_{ref})\right]$; $\alpha_{\lambda_L}^{par}(z)$ is the particle extinction coefficient at wavelength λ_L, that can be calculated from (2.11) and (2.12).

$\beta_{\lambda_L}^{mol}(z)$ can be calculated from Rayleigh scattering coefficients and atmospheric number density profiles retrieved from models or radiosonde measurements. For most lidar systems the ratio $O_{\lambda_R}(z)/O_{\lambda_L}(z)$ cancels out since $O_{\lambda_R}(z) \simeq O_{\lambda_L}(z)$. In this case, the profile of the

particle backscatter coefficient is not affected by the incomplete overlap between laser beam and receiver field of view and can be derived for all heights, even close to the lidar. In case of lidar systems with $O_{\lambda_R}(z) \neq O_{\lambda_L}(z)$ the ratio $O_{\lambda_R}(z)/O_{\lambda_L}(z)$ can be determined experimentally by performing a test measurement with the same interference filters in front of the detectors of both Raman and elastic channels (Whiteman et al., 1992). z_{ref} is estimated by scanning the free troposphere for a height interval with clear conditions. This is done by comparing the measured elastic signal with the pure molecular Raman signal (Rayleigh-fit method). If these two signals fit together in a certain height range (i.e. the signal ratio is constant with height), this is an indication for the absence of aerosols. The reference value $\beta_{\lambda_L}^{par}(z_{ref})$ is assumed to be 0 (aerosol-free atmosphere assumption).

Alternatively, the profiles of particle backscattering coefficients at the laser wavelength λ_L are retrieved from the elastically backscattered signals only, with assumptions on lidar ratio profiles, using an iterative method (Di Girolamo et al., 1999). The particle backscatter coefficient in the i-th iteration step is calculated by the following equation:

$$\beta_{\lambda_L,i}^{par}(z) = \left(\frac{P_{\lambda_L}(z)K_{\lambda_L,i}}{P_{\lambda_L,i}^{mol}(z)} - 1\right)\beta_{\lambda_L}^{mol}(z) \tag{2.14}$$

where: $P_{\lambda_L}(z)$ is the power of the elastic overlap-corrected lidar signal a wavelength λ_L; $\beta_{\lambda_L}^{mol}(z)$ is the molecular backscattering coefficient at the laser wavelength λ_L , calculated from models or radiosonde measurements; $P_{\lambda_L,i}^{mol}(z)$ is an estimated molecular signal, expressed as:

$$P_{\lambda_L,i}^{mol}(z) = \beta_{\lambda_L}^{mol}(z)exp\left(-2\int_0^z S^{par}(z')\beta_{\lambda_L,i-1}^{par}(z')dz'\right) \tag{2.15}$$

where $S^{par}(z)$ is an assumed particle lidar ratio profile; $K_{\lambda_L,i}$ is a calibration factor and can be determined in an aerosol-free region z_{ref} :

$$K_{\lambda_L,i} = \frac{P_{\lambda_L,i}^{mol}(z_{ref})}{P_{\lambda_L}(z_{ref})} \tag{2.16}$$

In an initial step, the molecular signal $P_{\lambda_L,0}^{mol}(z)$ is estimated with the assumption $\beta_{\lambda_L}^{par}(z) = 0$ and is then used to derive an initial value of $\beta_{\lambda_L,0}^{par}(z)$. In the following iteration step i, the backscatter coefficient $\beta_{\lambda_L,i}^{par}(z)$ is calculated from a molecular signal which is estimated from the previous backscatter profile $\beta_{\lambda_L,i-1}^{par}(z)$. This procedure is repeated until the difference between $\beta_{\lambda_L,i}^{par}(z)$ and $\beta_{\lambda_L,i-1}^{par}(z)$ is smaller than a certain threshold.

The sources of uncertainties in the retrieval of the backscattering coefficient from elastic signals only are the same as in the retrieval from the combination of elastic and Raman signals, plus two additional large sources of uncertainty: the uncertainty due to the assumption of a particle lidar ratio profile, that can easily exceed 20% (Sasano et al., 1985); the uncertainty in the lowest part of the backscattering profile due to the incomplete overlap between laser beam and receiver field of view and the necessity to correct measured signals with the overlap function (Mattis et al., 2007). The assumptions for lidar-ratio values are derived from climatologic observations in the same region with combined Raman/elastic lidar or from the literature (Collis and Russell, 1976; Barnaba and Gobbi, 2001, 2004; Amiridis et al.,2005). The assumed values of lidar ratio are 45 sr at 355/532 nm and 55 sr at 1064 nm for aerosols, and 18 sr for clouds. Alternatively, lidar ratio profiles or their mean values, derived from simultaneous and co-located measurements with combined Raman-elastic lidar, if available, are used. The particle backscattering coefficient in the aerosol-free region z_{ref} is assumed to be 1.44 x 10^{-8} sr^{-1} m^{-1} and 8.0 x 10^{-9} sr^{-1} m^{-1} in the altitude range around 6.5-8.5 km and 12-14 km above ground level (a.g.l.), respectively. These reference values come from climatologic measurements with combined Raman-elastic lidar technique. The vertical profiles of particle backscattering coefficient at 1064 nm are obtained using only the iterative method.

2.4.2 Water vapor mixing ratio

PEARL also allows measurements of water vapor mixing ratio (WVMR) profile from the ratio between the water vapor Raman signal at λ_{H_2O} = 407 nm and the nitrogen Raman signal at λ_{N_2} = 387 nm (Ansmann et al., 1992b; Whiteman et al., 1992; Whiteman et al., 2001):

$$\chi_{H_2O}(z) = C\,\frac{O_{N_2}(z)P(\lambda_{H_2O},z)\sigma(\lambda_{N_2})T(\lambda_{N_2},z)}{O_{H_2O}(z)P(\lambda_{N_2},z)\sigma(\lambda_{H_2O})T(\lambda_{H_2O},z)} \tag{2.17}$$

where: $\chi_{H_2O}(z)$ is WVMR at range z, defined as the ratio of the mass of water vapor to the mass of dry air in a given volume in units of g kg^{-1}; C is a constant including the optical and quantum efficiencies of the receiver for both the Raman channels, as well as other constant terms depending only on the lidar experimental setup; $O_{N_2}(z)$ and $O_{H_2O}(z)$ are the overlap functions of the Raman channels at 387 nm and 407 nm, respectively; $P(\lambda_{H_2O},z)$ and $P(\lambda_{N_2},z)$ are the intensities of Raman lidar signals at 407 nm and 387 nm, respectively; $\sigma(\lambda_{N_2})$ and $\sigma(\lambda_{H_2O})$ are the Raman backscattering cross sections for nitrogen and water

vapor, respectively, relative to the laser excitation wavelength λ_L = 355 nm (known from the theoretical Raman spectra of nitrogen and water vapor molecules); $T(\lambda_{N_2}, z)$ and $T(\lambda_{H_2O}, z)$ are the one-way transmissivities of the light from distance z to the receiver, at 387 and 407 nm, respectively. These include both molecular and particle extinction coefficients at 387 and 407 nm:

$$\frac{T(\lambda_{N_2},z)}{T(\lambda_{H_2O},z)} = exp\left[-\int_0^z \left(\alpha_{\lambda_{N_2}}^{mol}(z') + \alpha_{\lambda_{N_2}}^{par}(z') - \alpha_{\lambda_{H_2O}}^{mol}(z') - \alpha_{\lambda_{H_2O}}^{par}(z')\right) dz'\right] \qquad (2.18)$$

The molecular extinction coefficients $\alpha_{\lambda_{N_2}}^{mol}(z)$ and $\alpha_{\lambda_{H_2O}}^{mol}(z)$ are calculated from Rayleigh scattering coefficients and atmospheric number density profiles retrieved from models or from radiosonde measurements. The particle extinction coefficients $\alpha_{\lambda_{N_2}}^{par}(z)$ and $\alpha_{\lambda_{H_2O}}^{par}(z)$ are calculated from the particle extinction coefficient $\alpha_{\lambda_L}^{par}(z)$ at the laser wavelength λ_L = 355 nm, derived from (2.11), and by using (2.12) with å = 1 to scale it at the Raman wavelengths λ_R = 387 nm and λ_R = 407 nm.

For a perfect lidar system, with identical optical paths for both the Raman channels at 387 and 407 nm, the two overlap functions $O_{N_2}(z)$ and $O_{H_2O}(z)$ are the same and their ratio would be unity throughout the range of measurement. In a real lidar system, this ratio depart from unity for the ranges closest to the telescope. If this departure from unity is significant, the ratio of the overlap functions can be experimentally quantified by taking data in both channels using a common nitrogen interference filter, whereby both lidar system channels measure the same atmospheric quantity. The ratio of the data from these channels quantifies the ratio of the overlap functions.

Note that the temperature variation with the height implies a broadening of the Raman water vapor and nitrogen spectra, that makes necessary to take into account the dependence of the water vapor mixing ratio on the atmospheric temperature (Whiteman, 2003). However, this dependence is neglected in our algorithm, assuming that the interferential filter bandwidths, in the order of 0.5 nm - 1 nm, are chosen so as to transmit the whole Raman spectrum backscattered from molecules, thus limiting the effects of atmospheric temperature variations on the measured lidar signals (Behrendt et al., 2002).

Finally, water vapor Raman lidar technique needs to be calibrated, that means to estimate the terms independent on height z in (2.17). In principle, if the experimental setup of the Raman lidar system does not undergo modifications, the value of calibration constant should not change with the time. The water vapor lidar profiles are calibrated matching them to

water vapor profiles measured with co-located and simultaneous radiosoundings in an altitude range where both the lidar and radiosonde investigate a common atmospheric region. Alternatively, the water vapor Raman lidar is calibrated by vertically integrating the lidar profiles of WVMR and matching the integrated water vapor (IWV) values with the corresponding values retrieved by a microwave radiometer in the same time range of lidar measurements. In order to use this calibration method, some assumptions are necessary, since the lidar water vapor profiles do not cover the entire investigated atmospheric column. Indeed, there is a lack of lidar measurements in lowermost layers, due to an incomplete overlap between laser beam and telescope field of view, and in uppermost layers, due to the extinction of water vapor Raman signal. Therefore, it is necessary to make assumptions about the WVMR lidar profile in the altitude ranges where lidar measurements are missing. This occurs below the full overlap lidar height, typically from the surface to 300 - 600 m a.g.l., depending on the system optical setup, and above the maximum height available from lidar profiles. To estimate the water vapor content in these two regions, a climatologic WVMR profile obtained from the co-located radiosounding historical archive is used.

2.5 Ka-band Doppler radar

Since March 2009, a meteorological Ka-Band cloud radar (MIRA36), designed by METEK GmbH, is operative at CIAO. It is a mono static magnetron-based pulsed Ka-Band Doppler radar for unattended long term observation of cloud properties.

The radar has a 1 m diameter antenna and emits microwave pulses at 35.5 GHz with a peak power of 30 kW, a pulse width of 200 ns and a pulse repetition rate of 5 KHz. The antenna beam width is 0.6° × 0.6°, with an antenna gain of 49 dBi, which is the ratio between the emitted (or received) power compared to the emitted (or received) power if the antenna was a perfect isotropic radiator. Linearly polarized signal is transmitted while co- and cross polarized signals are received simultaneously to detect co- and cross polarized radar Doppler spectra.

Typically, the moments of the radar Doppler spectra are used in radar data analysis. In this work the 0^{th}, 1^{st}, 2^{nd} and 6^{th} moments of the spectrum are considered. The signal-to-noise ratio (SNR) is the integral or zero-th moment of Doppler spectrum divided by the receiver noise level; the mean Doppler velocity is the mean or the first moment of Doppler spectrum and provides direct measurements of the speed of movement of targets on the radar

pointing direction; the linear depolarization ratio (LDR) is the ratio between the SNR in the cross channel and the co-channel that provides information on the shape and typology of targets.

In order to obtain information on the number concentration of targets and their size, the radar reflectivity factor (Z), i.e. the sixth moment of the Doppler spectrum, is used. Assuming spherical liquids drops the radar reflectivity factor can be calculated from:

$$Z\ \alpha\ \int_0^\infty N(D) \cdot D^6 \cdot dD \tag{2.19}$$

where Z is measured in [$mm^6 m^{-3}$], N(D) dD is the number concentration of water droplets with diameters between D and D + dD. Usually, since Z has a very dynamic range, it is expressed in dBZ, where dBZ = 10 $\log_{10}$ (Z [$mm^6\ m^{-3}$]).

The cloud radar operating at CIAO provides accurate reflectivity measurements over a dynamic range of approximately seven orders of magnitude, from -50 dBZ to +20 dBZ throughout the troposphere (Kollias et al., 2001). The averaging of the spectra over 1 minute and 90 meters vertical resolution can increase the minimum of the range up to about -60 dBZ. The radar sensitivity is −40.3 dBZ at 5 km with a time resolution of 0.1 sec, while the Doppler velocity resolution is 0.02 ms^{-1}. The receiver calibration is within an accuracy of less than ±1 dB. The LDR accuracy is within ±2 dB (Madonna et al., 2013). The system is equipped with a clutter fence that strongly suppresses the ground clutter echo. The radar is also equipped with a 3-D scanning unit and it has been the first radar system in Europe working in Ka-band with the possibility of performing a ± 90° scanning of the atmosphere.

The radar typically operates in zenith pointing mode and it is able to provide radar vertical profiles with a time resolution in the order of seconds and a vertical resolution up to 15 m, though the current configuration is set to a time resolution of 10 s and vertical resolution of 30 m. The data processing of radar measurements, up to the averaged power spectra, is performed by a digital signal processor (DSP). This is performed simultaneously for co- and cross channel. For each range gate, the complex signals of a certain number of consecutive pulses are Fourier transformed, obtaining in this way the power spectra. On a next step, the spectral lines which are above the detection threshold are selected, the noise level is subtracted and the global moments from these averaged spectra are calculated. Typically 200 consecutive spectra are averaged, which results in a time resolution of 10 s and vertical resolution of 30 m. Additionally, in order to increase the radar sensitivity, a parallel data processing is performed averaging 1200 consecutive spectra and 3 range gates, which results

in a time resolution of 1 minute and vertical resolution of 90 m. As mentioned above, this data processing allows to enhance the radar sensitivity of 5-10 dBZ (Rosoldi et al, 2013).
While the radar probes the atmospheric vertical structure, it receives echoes caused by different kinds of targets from different altitude ranges. Therefore, for interpreting the cloud radar data it is essential to discriminate among the scatterers (denominated here as targets) that produce the signal. Frequently, multi peak spectra are observed in the cloud radar spectra, designating that the signals from different targets coincide in the spectra from single range gates. Since their Doppler velocities are different, they can be separated in many cases. Thereby, after the noise is removed, significant peaks are searched for each spectrum and the moments are calculated. Then a multi mode cluster classification scheme, which considers the global spectral moments, the LDR and the multi-peak moments, is applied. For this purpose, each peak is assigned to a target type and then the moments of all peaks that had been assigned to the same target type are recombined. In the MIRA36 cloud radar algorithms, the considered target types are cloud, rain and plankton, where plankton stands for non-hydrometeorological targets.

2.6 Microwave profiler

A ground-based microwave profiler (MP3014), designed by Radiometrics Corporation (Ware et al., 2003), is operational at CIAO since February 2004. It measures the sky brightness temperature (Tb) at 12 frequencies: 5 in the K-band, distributed from the centre onto the wing of the 22 GHz water vapor resonance absorption line, the rest are in the V-band, distributed on one shoulder of the 60GHz oxygen spin-rotation band. The radiometer is equipped with an infrared thermometer (IRT), installed on the top of radiometer cabinet, able to measure zenith Tb within the spectral range from 9.6 μm to 11.5 μm, and with surface meteorological sensors, used as constraints in the retrieval algorithm. The microwave profiler is also able to perform a 3-D scanning of the atmosphere though it typically operates viewing only the zenith direction. The microwave profiler is also equipped with a rain effect mitigation system able to minimize error resulting from the accumulation of liquid water and ice on the microwave radiometer radome.
The sky brightness temperatures are inverted using a neural network algorithm (Solheim et al., 1998) trained on about 10000 radiosounding profiles. The Tb inversion provides temperature, humidity and cloud liquid water profiles up to 10 km above the ground station.

Additionally, the inversion provides an estimation of the Integrated Precipitable Water Vapor (IPWV) and of the cloud Liquid Water Path (LWP). The uncertainty of the IPWV and LWP are calculated according to Cadeddu et al. (2009). Vertical profiles are given with a vertical resolution of 100 m up to 1 km and 250 m from 1 km to 10 km, with a minimum temporal resolution of 12 s.

2.7 Ceilometers

Among the active remote sensing devices, two laser ceilometers are also operational at CIAO. Since August 2004, a CT25K ceilometer type, manufactured by VAISALA, continuously measures the cloud-base height and the signal backscattered by atmospheric particles. The ceilometer is basically an elastic backscatter lidar system that uses a pulsed In-Ga-As diode laser, emitting light pulses at 905 nm with low energy (1.6 μJ of energy per pulse) and high repetition rate (6.67 kHz), and detects the elastic backscattered radiation. Depending on the cloud optical thickness, CT25K processing software, designed by VAISALA, is able to provide up to three cloud layer heights simultaneously. Besides cloud layers, it also provides the profile of attenuated backscattering coefficient at 905 nm up to 7.5 km with a vertical resolution of 30 m and a temporal resolution of 15 s. CT25K data are used by the Cloudnet retrieval algorithms described in section 2.8.

Since September 2009, a second ceilometer for cloud base measurements, CHM15k type manufactured by Jenoptik Laser Optik Systeme, is operative at CIAO. CHM15k uses a Nd:YAG pumped diode laser, emitting light pulses at 1064 nm wavelength with 8 μJ energy for pulse and 5.58 kHz repetition rate, and is equipped with a photon counting acquisition system.

It is able to measure the cloud base height of cloud layers up to 15 km above the ground with the possibility to investigate the optical properties of cirrus clouds up to the tropopause. As for the CT25K ceilometer, CHM15k processing software, designed by Jenoptik, provides up to three cloud layer heights simultaneously, but it also provides the retrieval of the boundary layer height and of the cloud penetration depth. The 1064 nm raw signal has a vertical resolution of 15 m and a temporal resolution of 30 s.

2.8 Cloudnet

Cloudnet (www.cloud-net.org) is a European network of ground-based remote sensing stations, that aims to provide vertical profiles of cloud and aerosol properties with high temporal and spatial resolution in order to continuously evaluate and improve the representation of clouds in mesoscale weather models. CIAO is one of the Cloudnet stations. The essential instruments that must be present at each station are a vertically pointing Doppler cloud radar and a backscatter lidar operating continuously. Usually the lidar is a near infrared laser ceilometer reporting only an uncalibrated attenuated backscatter coefficient. Recommended but non-essential instruments are microwave radiometer, for providing liquid water path, and rain gauge. Furthermore, profiles of atmospheric dynamic and thermodynamic parameters over each station, such as pressure, temperature, humidity and horizontal wind, are essential for Cloudnet retrieval algorithms. This information is obtained using hourly profiles from short-range model forecasts, that assimilate the data from the radiosonde network. For this purpose, the Met Office 6–11 hour forecast data are used as this model has the highest horizontal resolution (around 12 km) and the other models provide data only from 12 hours onwards. When Met Office data are unavailable, ECMWF model data are used.

For each station all datasets from instruments and model forecasts are processed by Cloudnet algorithms (Hogan and O'Connor, 2006; Illingworth et al., 2007) so as to provide different cloud properties to compare to numerical cloud models in order to quantify and improve their performance. Processing is done one day at a time. If at any time in the day radar, lidar or model data are missing, then there will be a gap in the output products.

The first step in the processing is the conversion of the vertical coordinate of each input dataset to height above mean sea level in meters. This correction is necessary as most instruments report range from the instrument in kilometers, and they may have been mounted at different heights above the ground. The ceilometers often points several degrees (between 2° and 5°) from zenith to avoid specular reflection from horizontally aligned pristine crystals, which could be mistaken by the algorithm for the presence of super-cooled liquid water. Therefore, the range reported by these instruments is multiplied by the sine of the zenith angle to obtain height. In order to obtain a common grid for all input and output datasets, lidar and model data are usually interpolated on the radar time and height resolution. Likewise, the rain rate and liquid water path are interpolated on the time resolution of the radar. For CIAO station the common grid is 30 s in time ad 30 m in height.

Cloudnet processing also provides a target categorization: in each radar/lidar pixel several target types, such as liquid droplets, ice particles, aerosols and insects, may be present. The type of target in each pixel is identified by applying, for each type of target, specific categorization algorithms employing specific input data. These algorithms are essentially based on the fact that the radar is sensitive to large particles, such as rain and drizzle drops, ice particles, and insects, while the lidar is sensitive to higher concentrations of smaller particles, such as cloud droplets and aerosols. Moreover, Cloudnet algorithms for liquid cloud droplets provide also the estimation of the heights of cloud base and cloud top with a time resolution of 30 s. These algorithms use the ceilometer attenuated backscatter coefficient, the radar reflectivity factor and the temperature profiles as input data. Cloud base height is identified by threshold values for attenuated backscatter coefficient and for its gradient; cloud top is identified in similar way or by radar reflectivity in the case that the lidar has been extinguished while the radar still has a signal.

The target categorization datasets represent the input data for the application of subsequent algorithms providing the cloud meteorological products, such as liquid water content (LWC) and ice water content (IWC), with the same high resolution of the observations. Finally, by averaging these products to the vertical and horizontal resolution of a model, it is possible to estimate the values of cloud fraction, LWC and IWC in the model grid box and compare them with the corresponding values provided by the model for quantifying and improving the performances of that model.

CHAPTER 3

METHODOLOGY

3.1 Target selection: thin liquid water clouds

In the introduction, the importance of characterizing the process leading to the droplet activation is discussed.

In this chapter, it is proposed a methodology developed in order to obtain quantitative information about droplet activation process and aerosol-cloud interactions. The methodology is based on the study of thin liquid water clouds, identified as low or midlevel super-cooled clouds characterized by a liquid water path (LWP) lower than about 100 gm^{-2} (Turner et al., 2007). Many types of clouds may fall into this broad classification, including stratus, cumulus, stratocumulus, altostratus and altocumulus clouds.

Thin liquid water clouds are interesting for different reasons. Firstly, they have a global mean coverage so extensive that they cannot be ignored in the study of the impact of clouds on the Earth's radiative balance and climate. The results obtained from the International Satellite Cloud Climatology Project (ISCCP) reveal that low and midlevel clouds, often containing liquid water, are characterized by a mean LWP value of 51 and 60 g m^{-2}, respectively, and cover 27.5% and 19% of the global surface, while the global mean cloud fractional coverage is 68.6% (Rossow and Shiffer, 1999). As a consequence, these clouds contribute for more than one third to the global mean cloud coverage.

Furthermore, thin liquid clouds consist of nearly spherical water droplets whose scattering properties are well described by Mie theory, unlike ice clouds, that may contain multiple crystal shapes and require much more complicated scattering theories that can also handle the particle shape.

Finally, thin liquid clouds are often optically thin, i.e. they have low optical depth, usually lower than 3. This implies that they can be frequently penetrated by the lidar laser beam to measure a backscattered signal from the cloud itself and above the cloud. Therefore, ground-based Raman lidar technique often allows to obtain the vertical profiles of aerosol, water vapor and cloud properties below, inside and above thin clouds with high vertical (in the order of 100 - 200 meters) and temporal (in the order of 10 minutes) resolutions.

In this work, particular attention is devoted to optically thin *"*broken*"* clouds, where *"*broken*"* refers to single layer clouds with a not homogeneous horizontal structure, characterized by cloud fields separated by cloud-free regions.

These clouds are particularly interesting, because within the time window of a night time lidar measurement (typically 2 hours) the lidar can detect both cloudy and cloudless regions and allows the study of the variability of optical properties and relative humidity (RH) in the transition from the cloudy regions to the cloudless regions, during the processes leading to the cloud formation and decay.

The methodology has been applied to night time observations of low and mid-level optically thin broken clouds performed simultaneously with the multi-wavelength Raman lidars, the cloud Doppler radar and the microwave radiometer.

3.2 Lidar analysis

The Raman lidar technique has been used to retrieve the vertical profiles of optical properties and water vapor content for aerosol and clouds. Taking advantage of the structure of broken clouds, two different types of lidar analysis have been considered for this study: "without clouds", by averaging, in a selected time window, only the cloud-free lidar signals (before and after the clouds) and skipping the lidar signals containing clouds; "with clouds", by averaging, in the same time window, only the lidar signals containing clouds. The number of cloudy signals is expressed through the so called "skipped fraction", defined as the ratio of the number of cloudy signals to the total number of lidar signals in the selected time window. The analysis without clouds provides the aerosol optical properties and water vapor content in cloudless regions surrounding the clouds, while the analysis with clouds provides the cloud optical properties and water vapor content in cloudy regions.

The lidar signals contaminated by clouds are identified by visual inspection of the nitrogen Raman lidar signals at 387 nm and assuming that a strong negative slope in the signals is due to the extinction by the liquid water droplets.

The identification of clouds on the basis of Raman lidar signals rather than elastic lidar signals is justified by the following considerations. Raman lidar signals are attenuated by both aerosol and droplets. Elastic signals are sensitive to the increase of both the backscattering and extinction of aerosol and droplets, with a predominance of backscattering at the cloud base region and of extinction at the cloud top region. The overall

result is the observation of a peak in the elastic signals. Nevertheless, the peak due to the cloud in the elastic signals can also be observed in presence of high concentrations and/or sizes of aerosols, for example large hydrated aerosols; therefore, algorithm dealing with the identification of atmospheric targets can only rely on threshold values to discriminate between these two situations. Conversely, a strong drop in the Raman signals is only observed in presence of liquid water and never in presence of aerosol only. For example, Figure 3.1 shows two nitrogen lidar signals at 387 nm measured with an acquisition time of 1 minute. The signal on the left panel is measured in presence of a thick dust layer in the altitude range between 1200 m and 3200 m above ground level (a.g.l.), delimited by the dashed vertical lines; the signal on the right panel is measured in presence of an optically thin liquid cloud in the altitude range between 1200 m and 2200 m a.g.l., delimited by the dashed vertical lines. It looks evident how the extinction due to cloud liquid water droplets produces a strong drop in the corresponding Raman signal, while a strong drop in the Raman signal is not visible even in presence of a thick aerosol layer with a very high extinction coefficient, such as dust. The described cloud detection approach can be automated and implemented in an algorithm for the automatic processing of raw lidar data such as the Single Calculus Chain (SCC) developed within EARLINET (European Aerosol Research LIdar NETwork) [D'Amico G., et al., 2012].

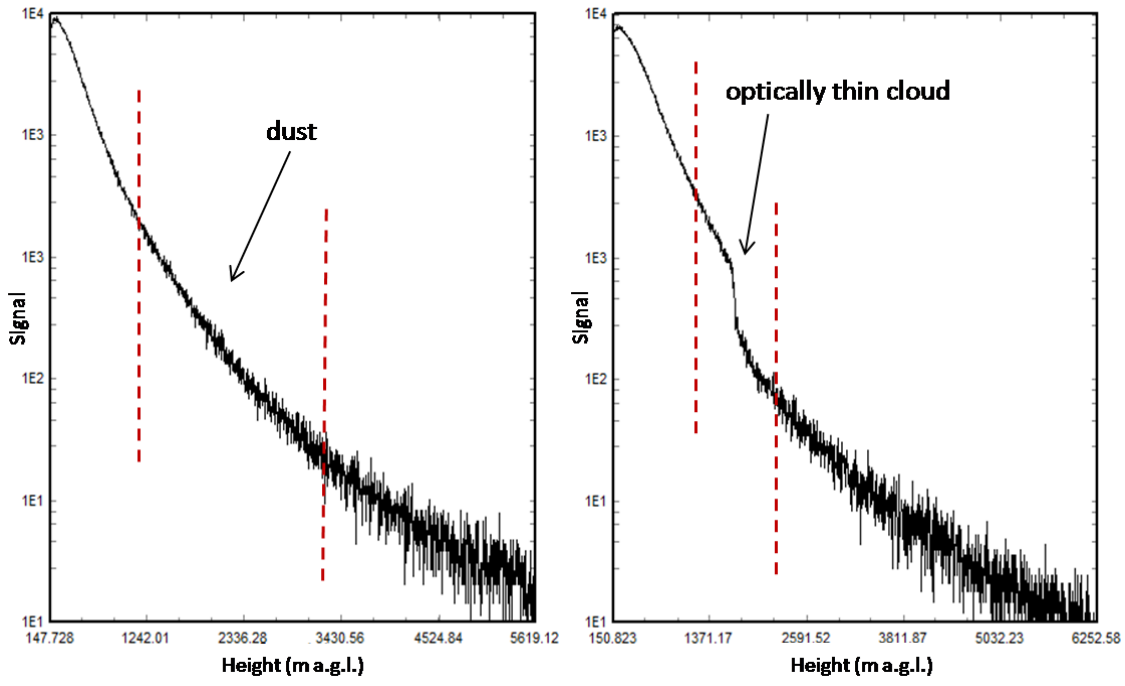

Figure 3.1: Examples of two nitrogen Raman lidar signals at 387 nm measured with an acquisition time of 1 minute in presence of a dust layer in the altitude range between 1200 m and 3200 m (left panel) and in presence of an optically thin liquid cloud between 1200 m and 2200 m (right panel). Heights are above ground level (a.g.l.)

The time windows selected for lidar analysis are in the range 15 - 45 minutes. This choice can be justified with the following considerations.

The averaging time for lidar analysis should be large enough to increase the signal to noise ratio (SNR) allowing to retrieve lidar products with low errors on the whole altitude range from the base to the top of clouds. This is particularly true for lidar analysis in presence of clouds, because within and above the clouds SNR strongly decreases due to the attenuation induced by cloud water droplets. In order to obtain lidar profiles of aerosol/cloud optical properties and water vapor content with a random uncertainty lower than 30% and a vertical resolution in the order of 100 - 200 m, a minimum time window of 5 minutes has been considered for the lidar analysis both with clouds and without clouds. For shorter time windows, the lidar systems operative at CIAO do not allow to achieve these performances. On the other hand, the time integration of lidar signals should be limited to intervals in which the atmosphere remains relatively stable with respect both to the aerosol properties and to the cloud properties. This is very challenging for clouds. In particular, the broken clouds, despite their not homogeneous horizontal structure, must be single layer clouds and should stay at the same altitude range during the selected time window. Actually, in the dataset considered in this study, it has not been rare the observation of aerosol layers being stable for the whole duration of a night time measurement session, while broken cloud layers stable for more than 20 minutes have never been observed. Therefore, the instability of broken clouds justify the adoption of a maximum time window of 45 minutes for the lidar data analysis.

For each observation of low or mid-level optically thin broken clouds, the vertical profiles of optical properties and water vapor content have been calculated using the same effective vertical resolution. The vertical smoothing produces a loss of information that results in a coarser effective vertical resolution than the raw one. Effective vertical resolution can be defined as the minimum distance for which two narrow and well-separated structures are resolved according to the Rayleigh criterion (Stasey, 1994). The effective vertical resolution for a lidar profile of an atmospheric parameter depends on the smoothing filter applied to the raw signal or to the final product, but also on the applied retrieval algorithm. The concept of effective vertical resolution is largely discussed in Pappalardo et al. (2004b).

The vertical profiles of aerosol/cloud extinction coefficient at 355 and 532 nm are calculated using the sliding linear fit technique. The number of bins used for the linear fit is the lowest possible allowing a reliable extinction estimation with a random uncertainty lower than 30%.

The relationship between the number of bins for the linear fit and the resulting effective vertical resolution is described in Pappalardo et al. (2004b).

The corresponding profiles of particle backscattering coefficient at 355, 532 and 1064 nm are calculated with a raw vertical resolution of 3.75 m and then smoothed on the same effective vertical resolution of the extinction profiles, using a 2^{nd} order Savitzky-Golay smoothing filter (W.H. Press et al., 1992). The relationship between the length of the Savitzky-Golay filter window and the effective vertical resolution is described in Iarlori et al. (2015).

The backscattering coefficients at 355 and 532 nm are retrieved with combined Raman-elastic lidar technique, while the backscattering coefficients at 1064 nm are retrieved with the iterative method, assuming a lidar ratio value of 55 sr outside the cloudy layers (derived from climatologic profiles of aerosol extinction and backscattering coefficient at 355 and 532 nm retrieved with combined Raman-elastic lidar technique and considering the spectra dependency), and the mean value of lidar ratio at 355 or 532 nm, scaled for the spectral dependency, inside the cloudy layers. The normalization constant used for this product comes from climatologic measurements with combined Raman-elastic lidar technique (see Chapter 2, paragraph 2.4.1). All the profiles of backscattering coefficient are calibrated above the cloudy layer.

The vertical profile of water vapor mixing ratio (WVMR) is calibrated using the integrated water vapor (IWW) measurements performed with the microwave radiometer and averaged on the same time window as the lidar analysis; if co-located and simultaneous radio-sounding profiles are available, the lidar WVMR profile is also calibrated using in-situ water vapor measurements, and then the calibrated profile is compared with the previous profile (see Chapter 2, paragraph 2.4.2). The RH profile is calculated from the lidar WVMR and the temperature profile obtained averaging the microwave radiometer measurements on the same time window of lidar analysis or, alternatively, from measurements performed by the co-located and simultaneous radio-sounding. Both WVMR and RH profiles are calculated with a raw vertical resolution of 15 m and smoothed to achieve the same effective vertical resolution of the extinction profiles.

The effective vertical resolutions used for lidar analysis are in the range between 160 m and 350 m. As mentioned above, the effective vertical resolution has been optimized in a way to obtain lidar profiles of particle optical properties and water vapor content at the highest vertical resolution and with a random uncertainty lower than 30%. In some cases, this was not possible for aerosol/cloud optical properties at 532 nm. For this reason, it is preferable to focus on aerosol/cloud optical properties retrieved at 355 nm.

Before concluding the description of the methodology of lidar analysis, it is necessary to add some details related to the retrieval of WVMR and RH profiles containing clouds.

The water vapor Raman lidar signal at 407 nm is much weaker than the nitrogen Raman signal due to the lower content of water vapor in the atmosphere. Moreover, even thin clouds with a low LWP are able to fully attenuate the Raman return from water vapor. This makes the measurements of water vapor within clouds very challenging. Moreover, the lidar calibration based on IWV measurements, provided by the microwave radiometer, is limited by the lack of lidar measurements in lowermost layers, due to the incomplete overlap between laser beam and telescope field of view, and in uppermost layers, due to low SNR of Raman signals. Therefore, it is need to integrate the water vapor retrieved using the lidar profile with the water vapor content in the two mentioned layers obtained using a climatologic profile of WVMR. This correction might bias the determination of the calibration constant. The bias is mainly due to the lack of lidar measurements in the lowest layers, that are also the moistest layers and mostly contribute to the total column water vapor. This is particularly relevant if clouds are present: the lower the clouds, the higher the bias. Furthermore, the low SNR of the water vapor Raman signal within the clouds reduces the vertical range profiled by the lidar and this increases the bias. For these reasons, if a relative calibration method based on IWV measurements is used, it is strongly recommended to use the more recent value of the calibration constant measured in clear sky condition or the value measured within the clear sky regions of the broken clouds.

Even when using a calibration constant value obtained in clear sky conditions, it is often challenging to get reliable lidar profiles of water vapor content within and above the clouds, if only cloudy lidar signals are averaged. Therefore, the retrieval of WVMR and RH with clouds has been performed averaging all lidar signals in the time window selected for the analysis, including in this way both cloudless and cloudy signals. As a result, WVMR and RH profiles with clouds represent an average between aerosol only conditions and cloudy sky conditions and not conditions of cloudy sky only. Nevertheless, these profiles allow to see the relative change in the relation between aerosol optical properties and RH as well as the change in the minimum value of RH, in the transition from aerosol to cloudy sky. This is relevant for catching the changes occurring within the clouds after the droplet activation.

Hereinafter, the products obtained from the analysis "without clouds" are denoted with the prefix "**NC**" and the products obtained from the analysis "with clouds" are denoted with the prefix "**C**".

3.3 Multiple scattering correction

All the **C** extinction coefficient profiles are corrected for multiple scattering in cloudy regions. Multiple scattering affects lidar measurements in an optically dense medium as fog and clouds. When the laser beam goes through this medium, not only the singly backscattered photons, but also the multiple scattered photons, undergoing multiple scattering processes, remain in the lidar receiver field of view (RFOV) and are backscattered to the receiver. As a result, multiple scattering makes the extinction coefficient of the scattering medium lower than its real value, that is the single scattering extinction coefficient. The intensity of multiple-scattered light, apart from the optical depth of the scattering medium and the size of the scattering particles, depends on the measurement geometry. The larger the volume from which the scattered light is detected, the larger the multiple scattering effect. Therefore, the multiple scattering effect increases with increasing laser beam divergence, RFOV and distance between the laser transmitter and the scattering volume. Because of the low laser beam divergence and the narrow RFOV used by lidars, forward scattering from cloud droplets is the most important process to evaluate the multiple scattering effect. The correction of aerosol extinction coefficient in cloud regions is performed with a multiple-scattering model that calculates multiple scattering intensities for both particulate and molecular lidar returns, by introducing in lidar equations multiple scattering parameters for particulate and molecular backscatter signals (Wandinger, 1998). In this work, the multiple scattering parameters are calculated using the code made available by Eloranta (Eloranta, 1998). To run the code, it is assumed a lognormal size distribution of cloud droplets with effective radius of 5.4 μm, derived from in situ measurements reported in literature for continental stratus and stratocumulus clouds (Miles et al., 2000). The first four scattering orders have been summed. The calculation have been performed using the specifications (the laser beam divergence and RFOV) of MUSA lidar, which is the system used for the retrieval of particle optical properties.

3.4 Characterization of cloud layers

By comparing the vertical profiles of **C** and **NC** optical properties and RH, it is possible to obtain important information on the vertical structure of the observed cloud layers. In particular, the vertical regions where no significant differences between **C** and **NC** optical

properties are observed, i.e. the regions where they coincide within the error bars, represent regions of atmosphere outside the cloud layer, in which CCN are not activated into droplets. The altitude range where the values of **C** extensive optical properties are significantly higher than the corresponding values of **NC** extensive optical properties, i.e. the region where they do not coincide within the error bars, is the region where CCN grow and droplet formation occurs, identified as the "activation region".

The vertical extension of cloud, consisting of liquid water droplets, is determined by using **C** and **NC** averaged nitrogen Raman lidar signals at 387 nm, calibrated on the same molecular lidar signal at 387 nm derived from a standard atmosphere model. Cloud base height is located where the **C** averaged Raman signal shows an inflection point, that is a local minimum of the first derivative of such signal. More specifically, the cloud base height is identified as the height where the derivative starts to decrease on the edge of the local minimum. If the derivative of the Raman signal is very noisy, it is smoothed by a moving average in order to better identify the cloud base height.

Cloud top height is identified as the height where the **C** averaged Raman signal starts to overlap the corresponding **NC** averaged Raman signal.

The profiles of RH allow to further identify the cloudy regions as the regions where the saturation conditions are reached.

Cloud phase is identified using the radar LDR or the vertical profiles of atmospheric temperature provided by a co-located and simultaneous radio-sounding, when available, or by the microwave radiometer. When cloud hydrometeors are detected by the radar, low values of LDR, typically ranging between - 36 and - 30 dB, indicate that cloud particles are close to the sphericity, according to the Mie theory, and they consist of water droplets, while higher values of LDR indicate that cloud particles consist of ice crystals. Nevertheless, as shown later in Chapter 4, a large fraction of warm clouds observed in this study consists of small hydrometeors with diameters from a few to tens of micrometers, with very low reflectivity values (less than - 50 dBZ). In these cases, very low values of LDR are below the radar sensitivity, because the intensity of the cross-polarized radar signal is typically much lower than the co-polarized radar signal, and LDR cannot provide useful information to indicate the presence of liquid phase of the clouds. In these cases, cloud phase is identified using the atmospheric temperature profiles obtained by the microwave radiometer, that allow to check if the cloud layers are located above or below the freezing level and to estimate the cloud base and cloud top temperatures.

The LWP for each observed cloud layer is estimated averaging the LWP provided by the microwave radiometer over the same time window of lidar analysis.

Finally, the cloud optical depth (COD) is obtained by integrating **C** extinction coefficient, corrected for multiple scattering, over the altitude range between the base and the top of the cloud, while the activation region optical depth (AROD) is calculated by integrating the same extinction coefficient over the altitude range between the base and the top of the activation region.

3.5 Characterization of aerosol in cloudless regions surrounding the clouds

The type of aerosol in cloud-free regions surrounding the clouds has been identified from the analysis of air mass back-trajectories provided by NOAA Hysplit model (Draxler and Rolph, 2014; Rolph, 2014), along with the values of aerosol intensive optical properties (lidar ratios and Ångström exponents) averaged over the altitude range between the base and the top of the cloudy region and retrieved from the lidar analysis without clouds.

The size distribution and complex refractive index of CCN in regions surrounding the clouds are retrieved from multi-wavelength Raman lidar observations, using the algorithm developed by Veselovskii et al. (2004).

Starting from the vertical profiles of **NC** extensive optical properties (i.e. extinction coefficients at 355 and 532 nm and backscattering coefficients at 355, 532 and 1064 nm, so called "3β + 2α" data set), CCN effective radius r_{eff}, number concentration N_t, surface area concentration S_t, volume concentration V_t, and complex refractive index are retrieved. More specifically, the average values of the optical properties, calculated over the altitude range between the base and the top of the cloudy region, are considered as input data of the algorithm for the retrieval of aerosol microphysics. The complex refractive index is strictly related to aerosol optical properties: its real part, m_R, determines the scattering processes, while its imaginary part, m_I, determines the absorption processes. From absorption and extinction coefficients, it is possible to derive the aerosol scattering coefficient and the single scattering albedo, that measures the portion of extinction due to scattering.

The inversion algorithms for the retrieval of aerosol microphysical parameters from multi-wavelength lidar sounding provide a dataset of possible solutions. From each of these solutions the aerosol optical properties are recalculated back. The solutions able to minimize the discrepancy, ρ, between the input optical data (i.e. the measured optical coefficients) and the optical data calculated from the solutions are selected and averaged to provide the final estimation of the microphysical properties. More precisely, the solutions with

discrepancy in a range [ρ_{min}, ρ_{max}] near the minimum discrepancy, ρ_{min}, are selected and averaged.

For mono-modal particle size distributions, the uncertainty of the retrieved parameters does not depend significantly on the choice of averaging interval [ρ_{min}, , ρ_{max}] (Veselovskii et al., 2002) and averaging is usually performed over an interval in which 10% of the solutions are concentrated. However, particle size distributions in the atmosphere typically consist of two modes, denoted as the fine mode and the coarse mode. Cases could occur along continental rims where marine and anthropogenic particles mix. Dust events could lead to the transport of large mineral particles into anthropogenically polluted areas. Hygroscopic growth could lead to comparably large particles. For bimodal particle size distributions the correct choice of averaging interval is more critical with respect to mono-modal size distributions. Therefore, with respect to the previous inversion codes, the inversion method of the algorithm developed by Veselovskii et al. (2004) improve the criterion for determining ρ_{max} according to the discrepancy of averaged solutions ρ^{ave}, determined as

$$\rho^{ave} = \frac{1}{N_{opt}} \sum_{i} \left| \frac{g_i - g_i^{ave}}{g_i} \right|$$

where N_{opt} is the number of available optical coefficients (in our case N_{opt} = 3β + 2α = 5), g_i is the i-th measured optical coefficient and g_i^{ave} is the corresponding optical coefficient calculated from the solutions averaged in the interval [ρ_{min}, , ρ_{max}]. The best parameter estimation is achieved for that averaging interval for which the averaged discrepancy ρ^{ave} becomes stable (it may oscillate around some constant level) and averaging is stopped before the discrepancy ρ^{ave} starts to rise. The errors of input optical data are not required to run the code. The availability of a data banks for Mie efficiencies in the code allows to speed up the computation and to take into consideration particles with radii up to 10 µm. In the retrieval, only spherical particles are considered because no information about depolarization is available; the ranges used for minimum and maximum radius of CCN are 0.05 µm - 0.2 µm and 0.55 µm - 10 µm, respectively; the ranges used for m_R and m_I are 1.35 - 1.68 and 0.0005 - 0.05, respectively.

3.6 Example of lidar analysis

In the following, a case relative to the night time observations collected at CIAO on 26 July 2010 is presented. Figure 3.2 shows the time series of lidar range corrected signal (RCS) at 1064 nm measured by MUSA system from 19:20 UTC to 21:00 UTC. The time series shows the presence of clouds between 2.0 km and 3.0 km above sea level (a.s.l.), in the time range from 19:20 UTC to 20:00 UTC (area within the black ellipse in Figure 3.2). These clouds are optically thin, because the laser beam is able to penetrate them and a backscattered signal from the atmosphere above them is detected. Moreover, the observed clouds are also broken, because they have a not homogeneous horizontal structure characterized by cloud fields separated by cloud-free regions.

Figure 3.3 shows the time series of vertical profiles of radar reflectivity factor Z (left panel) and LDR (right panel) measured by the Doppler radar. Z catches the largest fraction of the droplet size distribution (area within the black ellipse in Figure 3.3). The absence of signatures in the radar LDR time series indicates that LDR is lower than the detection sensitivity of the cross channel and does not allow to identify the shape and, therefore, the phase of the hydrometeors.

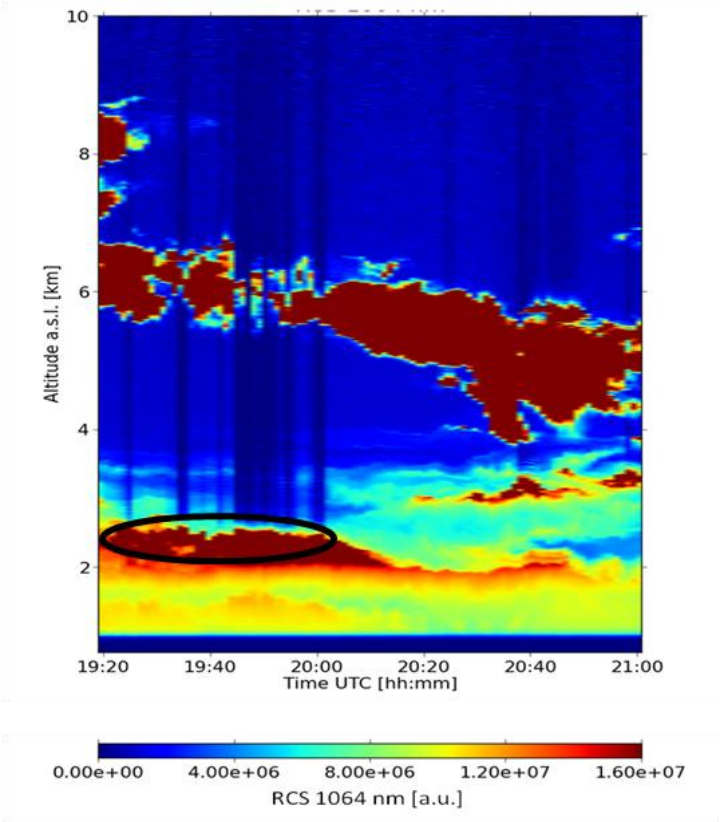

Figure 3.2: Time series of lidar range-corrected signal (RCS) at 1064 nm measured by MUSA on 26 July 2010 from 19:20 UTC to 21:00 UTC. Each profile has a vertical resolution of 3.75 meters and a time resolution of 60 seconds. The altitudes are above sea level (a.s.l.).

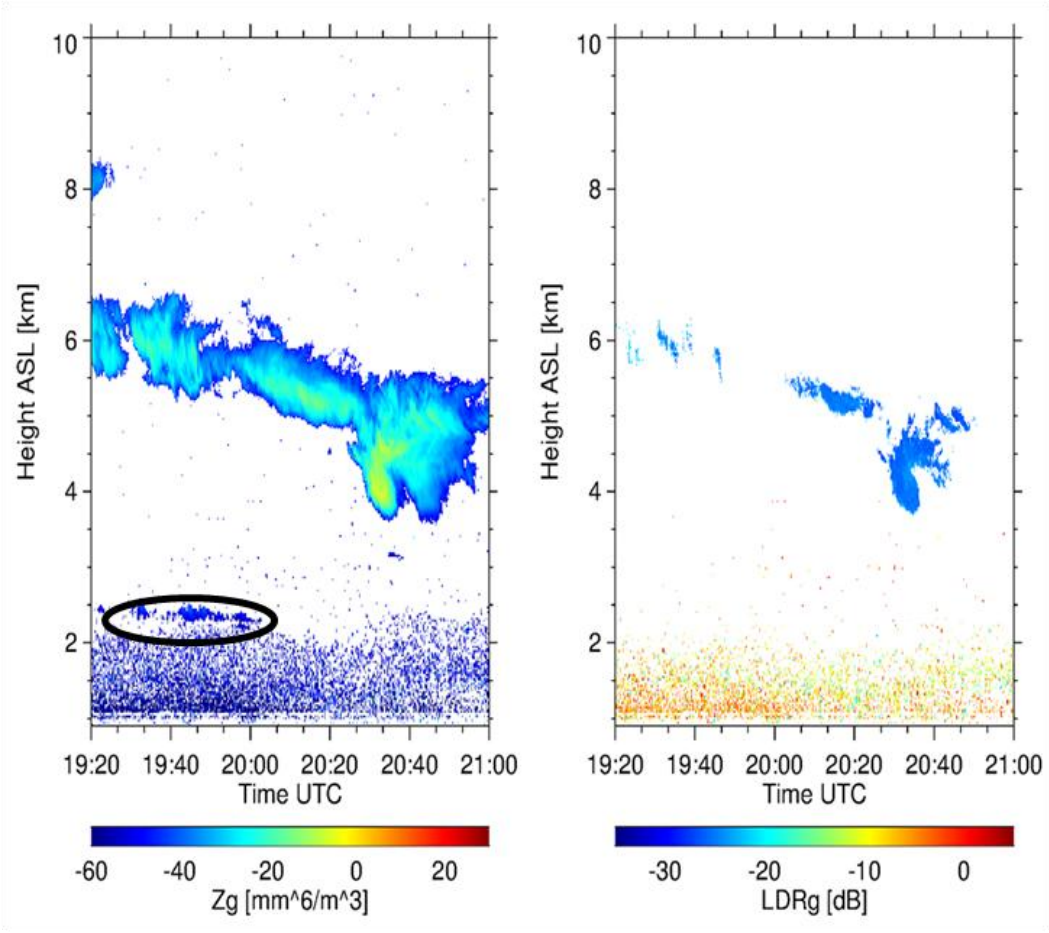

Figure 3.3: Time series of vertical profiles of reflectivity factor Z (on the left) and linear depolarization ratio LDR (on the right) measured by the Doppler radar operative at CIAO on 26 July 2010 from 19:20 UTC to 21:00 UTC. Both plots have a vertical resolution of 30 meters and a time resolution of 10 seconds. The heights are above sea level (a.s.l.).

Figure 3.4 (a) shows the vertical profiles of extinction coefficient at 355 nm "with clouds" (red line) and "without clouds" (black line) obtained with the Raman lidar technique, by averaging over a time window of 20 minutes, from 19:22 UTC to 19:42 UTC; the multiple scattering correction for the extinction coefficient "with clouds" is also reported (green line). Figure 3.4 (b) shows the vertical profiles of RH "with clouds" (red line) and "without clouds" (black line) obtained with the Raman lidar technique by averaging over the same time window and calibrated using simultaneous measurements of IWV performed by the microwave radiometer. For all the profiles in Figure 3.4 the effective vertical resolution is 270 m, while the "skipped fraction" is 40% .

In the vertical regions below 2230 m and above 2740 m a.s.l, **C** and **NC** extinction coefficients do not show significant differences within their error bars. In these regions, CCN are not activated into droplets. In the layer between 2230 m and 2740 m a.s.l., **C** extinction profile (red line) shows larger values than **NC** extinction profile (black line). This layer (pink area in

fig. 3.4a) has a vertical extension of 510 m and can be considered as the region where CCN grow and droplet formation occurs, that is the activation region.

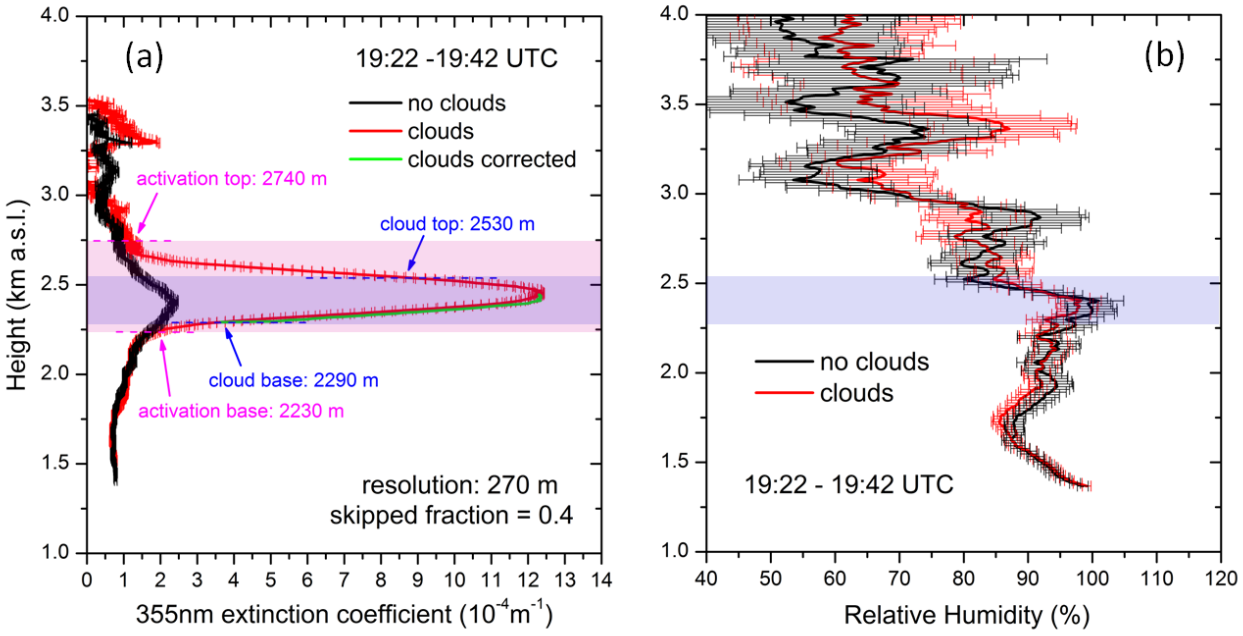

Figure 3.4: (a) Vertical profiles of extinction coefficient at 355 nm with clouds (red line) and without clouds (black line) obtained with Raman lidar technique by averaging over a time window of 20 minutes, from 19:22 UTC to 19:42 UTC. The extinction coefficient with clouds is also corrected for multiple scattering effect (green line). (b) Vertical profiles of relative humidity with clouds (red line) and without clouds (black line) obtained with Raman lidar technique over the same time window and calibrated using simultaneous measurements of water vapor performed by the microwave radiometer. The effective vertical resolution is 270 m and the skipped fraction is 40% .

Figure 3.5 shows the averaged nitrogen Raman lidar signals at 387 nm with clouds (blue line) and without clouds (green line). Both the signals are calibrated on the molecular lidar signal at 387 nm derived from a standard atmosphere model (red line). Figure 3.6 shows the first derivative of the Raman signal with clouds. This derivative is smoothed by a moving average with a smooth width of 24 points. The cloud base height, located where the **C** Raman signal shows an inflection point, corresponding to a local minimum of the first derivative of this signal, is identified as the height at which the derivative starts to decrease on the decreasing edge of the local minimum and is estimated at 2290 m a.s.l. (see arrows in Figures 3.5, 3.6). The cloud top height, identified as the height where the **C** Raman signal starts to overlap the corresponding **NC** averaged Raman signal, is estimated at 2530 m a.s.l. (see arrow in Figure 3.5). Therefore, the cloud region (purple area in Figure 3.4a) has a vertical extension of 240 m within the larger activation region.

RH profiles in figure 3.4 (b) show a good correlation within the cloudy layer and the saturation is reached close to the cloud base, in a good agreement within the respective error bars.

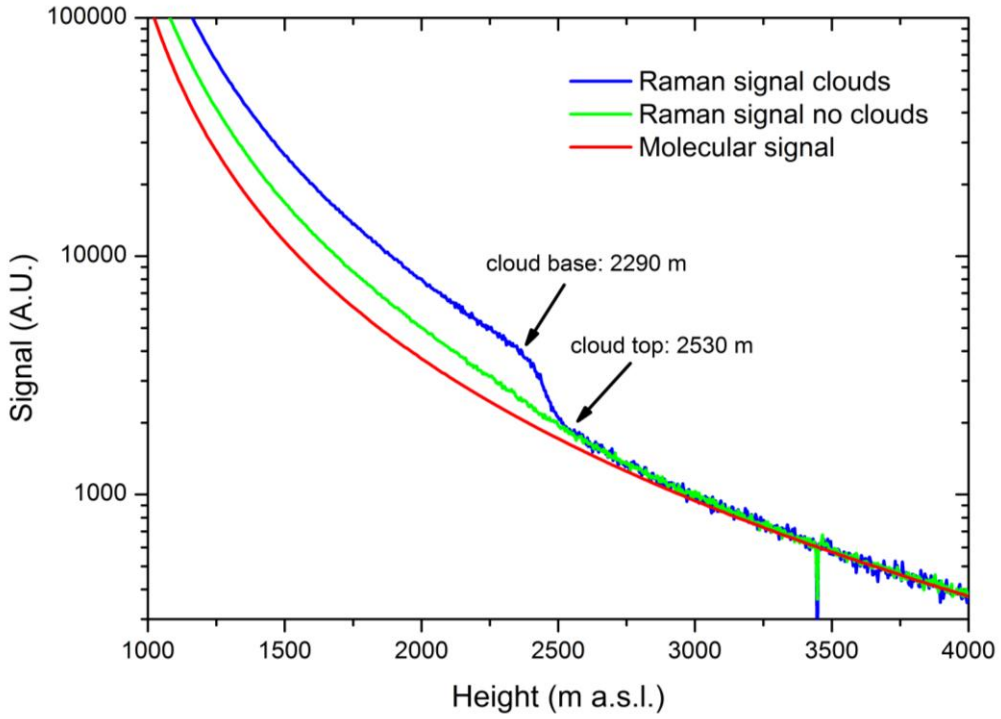

Figure 3.5: Averaged nitrogen Raman lidar signals at 387 nm with clouds (blue line) and without clouds (green line). Both signals are calibrated on a molecular lidar signal at 387 nm calculated using a standard atmosphere model (red line).

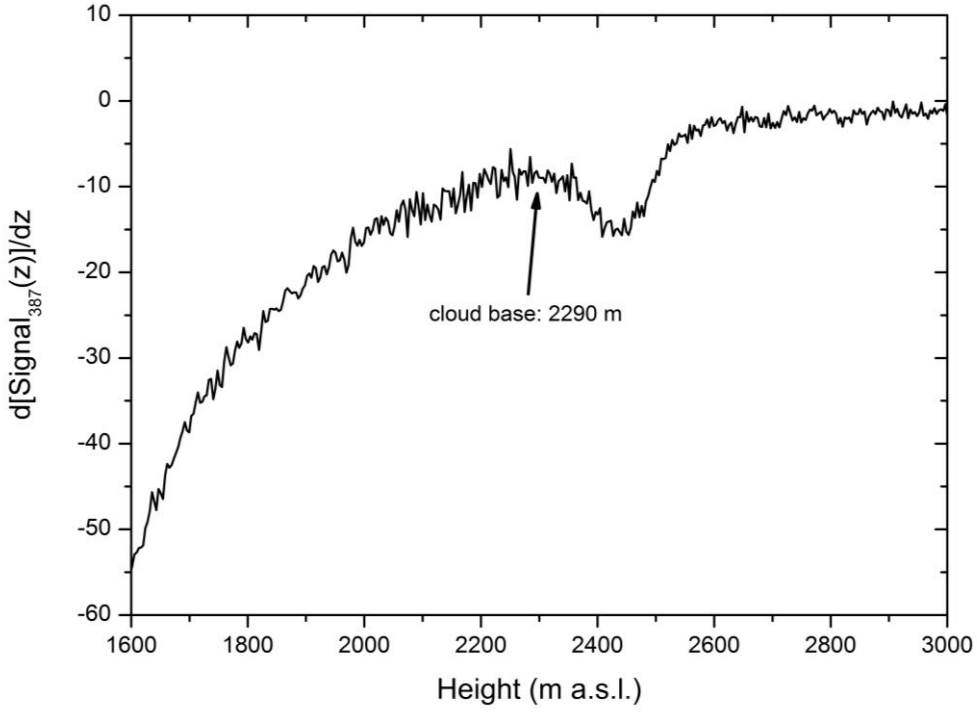

Figure 3.6: First derivative of the averaged nitrogen Raman lidar signal at 387 nm with clouds. The derivative is smoothed by a moving average with a smooth width of 24 points, corresponding to an effective resolution of 86.25 m.

Figure 3.7 shows the vertical profiles of 355 nm backscattering coefficient (left panel) and lidar ratio (right panel) "with clouds" (red lines) and "without clouds" (black lines), corresponding to the same lidar analysis of figure 3.4. It can be observed that in the layer between cloud base and cloud top, **C** backscattering profile (red line on the left panel of figure 3.7) is higher than **NC** backscattering profile (black line), and **C** lidar ratio profile (red line on the right panel of figure 3.7) is lower than **NC** lidar ratio profile. This allows to discriminate between aerosols and clouds. Particularly, in the layer between cloud base and cloud top, the cloud backscattering coefficient ranges from 1.71×10^{-5} m^{-1} sr^{-1} to 8.64×10^{-5} m^{-1} sr^{-1}, with a mean value of $6.81 \times 10^{-5} \pm 1.95 \times 10^{-5}$ m^{-1} sr^{-1}, while the aerosol backscattering coefficient ranges from 4.1×10^{-6} m^{-1} sr^{-1} to 6.3×10^{-6} m^{-1} sr^{-1}, with a mean value of $5.6 \times 10^{-6} \pm 0.6 \times 10^{-6}$ m^{-1} sr^{-1}; in the same altitude range, the cloud extinction coefficient ranges from 3.6×10^{-4} m^{-1} to 12×10^{-4} m^{-1}, with a mean value of $10 \times 10^{-4} \pm 2.3 \times 10^{-4}$ m^{-1}, while the aerosol extinction coefficient ranges from 1.6×10^{-4} m^{-1} to 2.4×10^{-4} m^{-1}, with a mean value of $2.1 \times 10^{-4} \pm 0.2 \times 10^{-4}$ m^{-1}. Moreover, for the same layer, the cloud lidar ratio ranges from 13.7 sr to 21.4 sr, with a mean value of 14.6 ± 1.2 sr, while the aerosol lidar ratio ranges from 33.2 sr to 37.7 sr, with a mean value of 37.8 ± 3.6 sr. So high values of cloud extinction and backscattering coefficients and so low values of cloud lidar ratio are never observed in cloud-free atmosphere and are comparable with the values previously measured and calculated in liquid water clouds (Pinnick et al., 1983; Wandinger, 1998; Wu et al., 2009).

Moreover, the value of the lidar ratio in liquid water clouds can be derived theoretically using Mie theory, assuming that the cloud droplets are spherical and have a well defined refractive index. Assuming a gamma cloud droplet size distribution derived from in situ measurements for stratocumulus clouds (Miles et al., 2000), it is obtained that for droplet diameter between 8 and 20 μm, which are typical values for stratocumulus clouds, the value of lidar ratio at 355 nm is almost constant, with a mean value of 18.9 ± 0.4 (O'Connor et al., 2004). The measured value may deviate from the theoretical one because the assumptions on which the theoretical calculations are based might be not enough accurate for the investigated scenarios.

Note that, in the layer just below the cloud base, between 2140 m and 2270 m a.s.l., and in the layer above the cloud top, between 2620 m and 2760 m a.s.l., a strong decrease of backscattering coefficient, even to negative values, and, consequently, a strong increase of lidar ratio are observed in **C** profiles (red lines in figure 3.7). This behavior is the effect of the use of a 2^{nd} order Savitzky-Golay smoothing filter in those vertical regions where strong gradients of the aerosol backscattering coefficient occur, such as the layers close to the

cloud base and cloud top. Indeed, this effect within the activation region, below the cloud base and above the cloud top, has been observed in most of the selected case studies; in some cases this effect also affected a few points below the cloud top. For all these cases, the values of cloud backscattering coefficient and of cloud lidar ratio at these altitudes have been cut in the following statistical analysis described in Chapter 4.

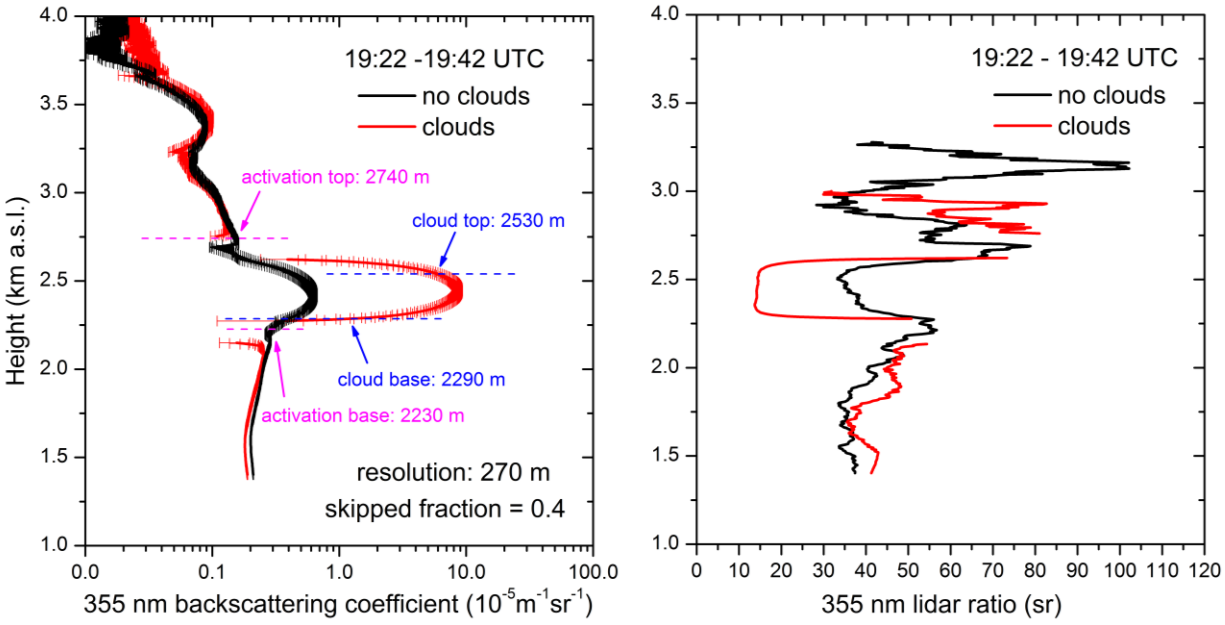

Figure 3.7: Vertical profiles of 355 nm backscattering coefficient (left panel) and lidar ratio (right panel) with clouds (red lines) and without clouds (black lines) obtained with Raman lidar technique by averaging over a time window of 20 minutes, from 19:22 UTC to 19:42 UTC. The effective vertical resolution of the profiles is 270 m and the skipped fraction is 40% .

By averaging the temperature profile provided by the microwave radiometer over the same time window of the lidar analysis, from 19:22 UTC to 19:42 UTC, cloud base and cloud top temperatures are estimated at 277 K and 275 K, respectively. The LWP in the time window of lidar analysis is lower than 60 gm^{-2} with an average value of 15 gm^{-2}. These results indicate the liquid phase of the observed clouds.

On the other hand, for these clouds, Z ranges from - 58 dBZ to - 44 dBZ, with a mean value of -49 dBZ, and no LDR is detected. Indeed, for so low values of radar reflectivity, the values of LDR less than about - 15 dB are below the radar sensitivity, because the intensity of the cross-polarized radar signal is typically much lower than the co-polarized radar signal. Therefore, for the selected case, all the LDR values less than about - 15 dB are not detected and are possible and the radar LDR does not allow to identify the cloud phase.

The calculated values of COD and AROD at 355 nm are 0.24 and 0.33, respectively.

Table 3.1 indicate the values of multi-wavelength aerosol optical properties in cloud-free regions, averaged over the altitude range between the base and the top of cloudy region and obtained with lidar analysis without clouds. These properties include extinction coefficients α at 355 and 532 nm, backscattering coefficients β at 355, 532 and 1064 nm, lidar ratios S at 355 and 532 nm and Ångström exponents å related to the above mentioned extinction and backscattering coefficients.

Figure 3.8 shows the air mass backtrajectories calculated up to 5 days before the observations, provided by NOAA Hysplit model (Draxler and Rolph, 2014; Rolph, 2014) and related to the aerosol layer that is in regions surrounding the clouds. Backtrajectories are calculated at 3 different height levels: 1400 m a.g.l. (i.e. 2160 m a.s.l.), that is about 100 m below the cloud base, 1650 m a.g.l. (i.e. 2410 m a.s.l.), that corresponds to an altitude inside the cloud and 2000 m a.g.l. (i.e. 2760 m a.s.l.), that is above the cloud top.

The retrieved values of S, between 30 sr an 40 sr, and of å, between 0.6 and 1, are consistent with the presence of mixed urban haze and fresh/aged smoke particles or forest fire smoke in the troposphere (Muller et al., 2007). This is likely confirmed by the analysis of the back-trajectories, showing the origin from North and Central Europe of the air masses related to the selected aerosol layer.

Finally, the size distribution and the complex refractive index of aerosol in regions surrounding the clouds are retrieved from the 3β +2α data set reported in Table 3.1, used as input data of the algorithm for the retrieval of aerosol microphysics. The retrieved microphysical parameters, i.e, CCN effective radius r_{eff}, number concentration N_t, surface area concentration S_t, volume concentration V_t, real part m_R and imaginary part m_I of complex refractive index, are shown in Table 3.2. The values of r_{eff} = 0.41 μm, m_R = 1.465 and m_I = 0.005 are consistent with the presence of urban - industrial aerosols following the climatologic values provided by Aerosol Robotic Network (AERONET) measurements (Dubovik et al., 2002).

wavelength (nm)	α (m^{-1})	β (m^{-1} sr^{-1})	S (sr)	å(α_{355}-α_{532})	å(β_{355}-β_{532})	å(β_{532} -β_{1064})
355	2.11×10^{-4}	5.61×10^{-6}	37.84	0.85	0.59	-
532	1.36×10^{-4}	4.44×10^{-6}	31.40	0.85	0.59	0.95
1064	-	2.30×10^{-6}	-	-	-	0.95

Table 3.1: Multi-wavelength aerosol optical properties averaged over the altitude range between the base and the top of cloudy region and obtained with lidar analysis without clouds: α and β are the extinction and backscattering coefficients, respectively, at the indicated wavelengths; S are lidar ratios at the indicated wavelengths; å are Ångström exponents related to extinction coefficients at 355 and 532 nm, to backscattering coefficients at 355 and 532 nm and to backscattering coefficients at 532 and 1064 nm.

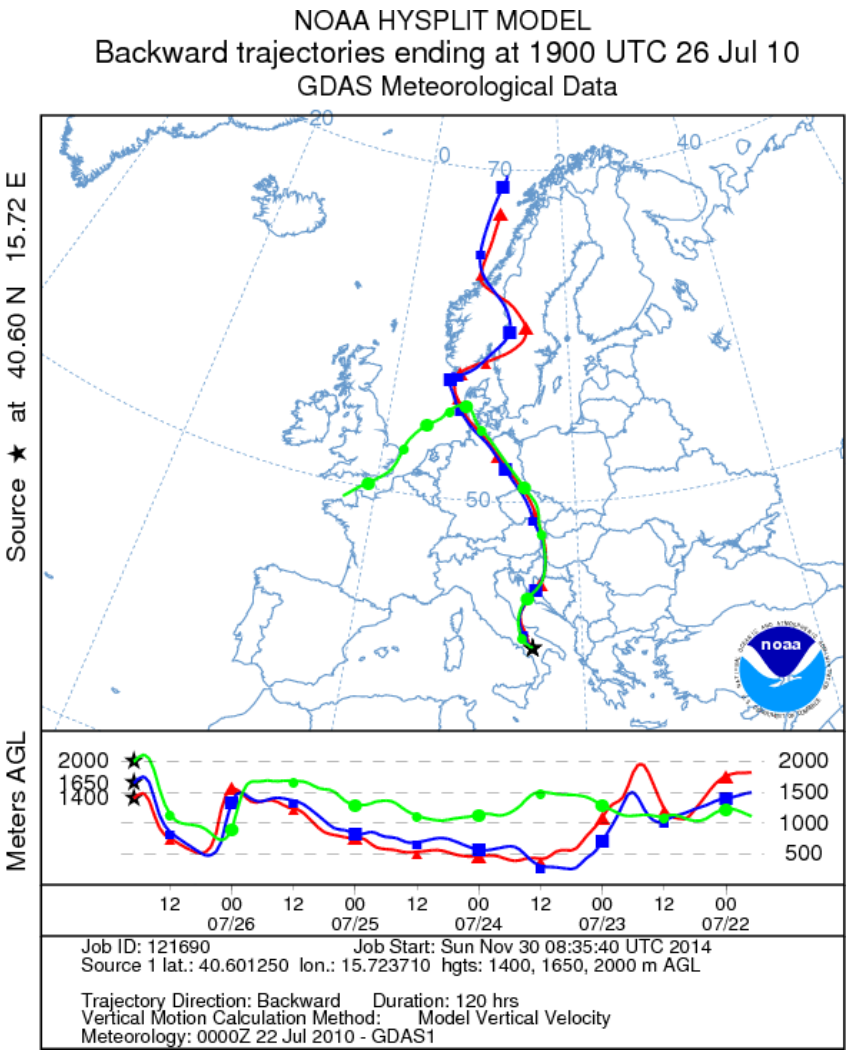

Figure 3.8: Back-trajectories calculated for air masses related to the aerosol layer that is in regions surrounding the clouds at the altitudes of 1400 m (red line), 1650 m (blue line) and 2000 m (green line) a.g.l.

Microphysical parameters	Input : 3β + 2α data set
r_{eff} (µm)	0.41 ± 0.1
N_t (cm^{-3})	1200 ± 790
S_t ($\mu m^2\ cm^{-3}$)	370 ± 81
V_t($\mu m^3\ cm^{-3}$)	52 ± 19
m_R	1.465 ± 0.0816
m_I	0.005 ± 0.0037

Table 3.2: Microphysical parameters of aerosols in regions surrounding the clouds retrieved from the values of extensive optical properties (3β +2α data set) reported in Table 3.1, used as input data of the algorithm developed by Veselovskii et al. (2004). These parameters include aerosol effective radius r_{eff}, number concentration N_t, surface area concentration S_t, volume concentration V_t , real part m_R and imaginary part m_I of complex refractive index.

CHAPTER 4

RESULTS

In this chapter, the results of the analysis of 20 night time observations of low or mid-level optically thin broken clouds, performed in the period 2010-2013 with multi-wavelength Raman lidars, the cloud Doppler radar and the microwave radiometer operative at CIAO, are presented and discussed. In Table 4.1, date, time and altitude range of the observed clouds are reported. Each observation is identified by a case number. Applying the methodology described in the previous chapter, several cloud layer properties have been retrieved, such as the geometrical and optical depth of both the activation and the cloud region, the height and temperature of cloud base and top, the LWP. All the observed cloud layers have been characterized as follows:

a. the retrieved cloud properties are compared with the corresponding Cloudnet products, with particular reference to cloud boundaries;
b. the variability of optical properties and humidity in the transition from the cloudy regions to the cloud-free regions surrounding the clouds have been studied, with the aim to empirically investigate aerosol activation and cloud formation process;
c. the moments of the radar Doppler spectrum, in particular the signal to noise ratio (SNR), the mean Doppler velocity and Z, are analyzed in order to study droplet size, updrafts and downdrafts during aerosol activation and cloud dynamical development;
d. finally, the microphysical parameters of CCN in the cloud-free regions are correlated with cloud updrafts and downdrafts.

Case number	Date	Time (UTC)	Altitude range (km a.s.l.)
1	07 June 2010	1950-2020	2.5-3.5 (mid-level clouds)
2	28 June 2010	2040-2100	2.5-3.5 (mid-level clouds)
3	26 July 2010	1920-1945	2.0-3.0 (mid-level clouds)

4	08 August 2010	0105-0130	2.5-3.5(mid-level clouds)
5	17 February 2011	1910-1930	1.5-2.5 (low level clouds)
6	30 June 2011	2000-2025	1.5-2.0 (low level clouds)
7	07 July 2011	1945-2005	3.5-4.5 (mid-level clouds)
8	04 August 2011	2010-2040	3.5-4.5 (mid-level clouds)
9	04 August 2011	2050-2115	3.5-4.5 (mid-level clouds)
10	10-11 August 2011	2345-0015	1.5-2.5 (low level clouds)
11	03 June 2013	1920-1955	2.0-2.5 (mid-level clouds)
12	09 September 2010	0210-0240	1.0-2.0 (low level clouds)
13	13 May 2010	2135-2200	1.5-2.0 (low level clouds)
14	24 June 2010	2050-2130	2.0-3.0 (mid-level clouds)
15	26 July 2011	0150-0220	2.5-3.5 (mid-level clouds)
16	04 October 2010	2030-2100	3.5-4.5 (mid-level clouds)
17	27 August 2011	0015-0100	4.0-5.0 (mid-level clouds)
18	12 August 2010	1850- 1915	2.0-2.5 (mid-level clouds)
19	13 May 2010	2320-2350	1.5-2.0 (low level clouds)
20	13 May 2010	2255-2325	1.5-2.0 (low level clouds)

Table 4.1: 20 cases of low or mid-level optically thin broken clouds observed at CIAO.

4.1 Cloud layer properties

As mentioned above, using the methodology described in Chapter 3, several properties of cloud layers have been retrieved. These properties are reported in Table 4.2, while their variability is reported in Table 4.3. The types and source regions of aerosols in cloudless regions surrounding the clouds are also reported in these tables.

For the cases 11 and 16, referred to the observations of 3 June 2013 and of 4 October 2010 according to the Table 4.1, the radiometer LWP and products are missing. For the case 18, referred to the observation of 12 August 2010, the radiometer does not detect the presence of liquid water.

The activation region, where CCN grow and condensation occurs, has a vertical extension ranging from 290 m to 1040 m. The height of cloud base ranges from 1440 m to 4550 m a.s.l., while the height of cloud top ranges from 1640 m to 4730 m a.s.l. Cloud region, where condensation occurs, is obviously identified as the region between cloud base and cloud top, and it has a geometrical depth ranging from 90 m to 500 m. The cloud optical depth (COD) at 355 nm ranges from 0.06 to 1.20, while the activation region optical depth (AROD) at 355 nm ranges from 0.09 to 1.45. The temperatures of cloud base and cloud top are estimated from the atmospheric temperature profiles provided by radio-soundings, if available, or by the microwave radiometer measurements. The cloud base temperature ranges from 270 K to 286 K and is above the freezing temperature in 80% of the selected cases, while the cloud top temperature ranges from 268 K to 284 K and is above the freezing temperature in 75% of the selected cases. 15 cases (75% of the cases) show clouds with base and top temperatures above the freezing temperature and therefore they are liquid water clouds. For the remaining 5 clouds (25% of the cases), 1 cloud has a base temperature of 276 K and a top temperature of 272 K, and 4 clouds have temperatures between 268 and 272 K. Such temperature values, as well as the relatively low values of the radar reflectivity (lower than -40 dBZ) and of LDR (lower than -30 dB) indicate that these clouds are likely super-cooled liquid water clouds, or at most mixed-phase clouds with small liquid droplets. This is also confirmed by the cloud LWP estimations provided by the microwave radiometer, which indicate the presence of liquid water for all the observed clouds, with LWP values lower than 180 g m^{-2}. Finally, it is worth to add that the aerosol type in cloud-free regions surrounding the broken clouds is originated from different sources (e.g. dust, continental, mixed).

Case number	Activation region: base height (m a.s.l.)	Activation region: top height (m a.s.l.)	Activation region thickness (m)	Cloud base height (m a.s.l.)	Cloud top height (m a.s.l.)	Cloud layer thickness (m)	COD	AROD	Cloud base temperature (K)	Cloud top temperature (K)	LWP ($g\ m^{-2}$)	Aerosol type/ source region
1	2640	3110	470	2800	3030	230	0.38	0.53	276	275	5-10	mixed , Central Europe
2	2650	3160	510	2730	2920	190	0.10	0.15	277	276	10-20	mixed, East Europe
3	2230	2740	510	2290	2530	240	0.24	0.33	277	275	15-60	mixed, North - Central Europe
4	2750	3170	420	2850	3030	180	0.24	0.36	277	276	10-15	urban haze, Central Europe
5	1810	2400	590	2120	2340	220	0.43	0.60	271	269	35-165	desert dust, Sahara
6	1620	2000	380	1670	1900	230	0.06	0.09	284	283	90-100	urban haze, Southwest Europe
7	3560	4000	440	3670	3890	220	0.37	0.47	274	273	65-80	mixed, Russia - North Europe
8	3490	4250	760	3660	4070	410	0.31	0.37	276	273	140-200	desert dust, Sahara
9	3540	4320	780	3610	4110	500	0.40	0.46	276	272	120-140	desert dust, Sahara
10	1490	2170	680	1620	2110	490	1.00	1.06	283	281	130-170	mixed, North Europe
11	2010	2370	360	2040	2300	260	1.20	1.45	278	276	n.a.	marine, Northwest Europe
12	1350	1740	390	1440	1740	300	0.59	0.64	286	284	85-200	desert dust + marine, Sahara-Tyrrhenian Sea
13	1610	1910	300	1650	1870	220	0.14	0.17	279	278	10-10	mixed, North Europe
14	1980	2330	350	2090	2320	230	0.43	0.51	279	278	50-150	urban haze industrial, North - Central Europe
15	3010	3330	320	3090	3180	90	0.06	0.13	271	271	100-110	urban industrial, Northwest Europe
16	3560	4600	1040	3890	4300	410	0.45	0.64	270	268	n.a.	desert dust, Sahara
17	4430	4990	560	4550	4730	180	0.26	0.44	270	269	190-210	desert dust + fire smoke, Sahara-East Europe
18	2150	2490	340	2230	2410	180	0.12	0.18	284	283	0	Urban, Southwest Europe
19	1380	1670	290	1510	1640	130	0.15	0.24	280	279	20-50	urban-smoke mixed, Southwest Europe

20	1480	1940	460	1700	1860	160	0.12	0.22	279	278	15-40	urban-smoke mixed Southwest Europe

Table 4.2: Properties of low or mid-level optically thin broken clouds observed at CIAO in the dataset considered for this study. For the cases 11 and 16, the radiometer LWP is not available. For the case 18, the radiometer does not detect the presence of liquid water.

Parameter	Range
Activation region thickness, m	290 - 1040
Cloud base height, m a.s.l.	1440 - 4550
Cloud top height, m a.s.l.	1640 - 4730
Cloud layer thickness, m	90 - 500
COD	0.06 - 1.20
AROD	0.09 - 1.45
Cloud base temperature, K	270 - 286
Cloud top temperature, K	268 - 284
LWP, g m^{-2}	5 - 180
Aerosol type	variable (dust, continental, mixed, ….)

Table 4.3: Variability of cloud properties for the low or mid-level optically thin broken clouds observed at CIAO and reported in Table 4.2.

4.2 Comparison with Cloudnet

Cloud base and top retrievals of thin broken clouds obtained from the Raman lidar observations have been compared with the Cloudnet categorization retrieval.

For each analyzed cloud layer, Cloudnet estimations of the heights of cloud base and cloud top have been averaged on the time window of the corresponding lidar analysis with clouds and compared with the estimations based on Raman lidar technique. Cloudnet estimations are based on the use of attenuated backscatter coefficient profiles with a vertical resolution of 30 m, corresponding to an uncertainty of 15 m for these estimations. Raman lidar

estimations are based on the use of nitrogen Raman lidar signals at 387 nm with a raw vertical resolution of 3.75 m, which corresponds to an uncertainty of 1.875 m. Figure 4.1 shows the comparison between Raman lidar technique and Cloudnet in the estimation of cloud base height for the selected case studies. The red points represent Raman lidar estimations and the black points represent Cloudnet estimations. For the cases 11 and 16, referred to the observations of 3 June 2013 and of 4 October 2010 according to the Table 4.1, Cloudnet products are not available. In 50% of cases, the discrepancy between the two techniques is less than 50 m, while in the remaining cases the Raman lidar technique overestimates the height of the cloud base with respect to Cloudnet, with discrepancies between 70 m and 120 m.

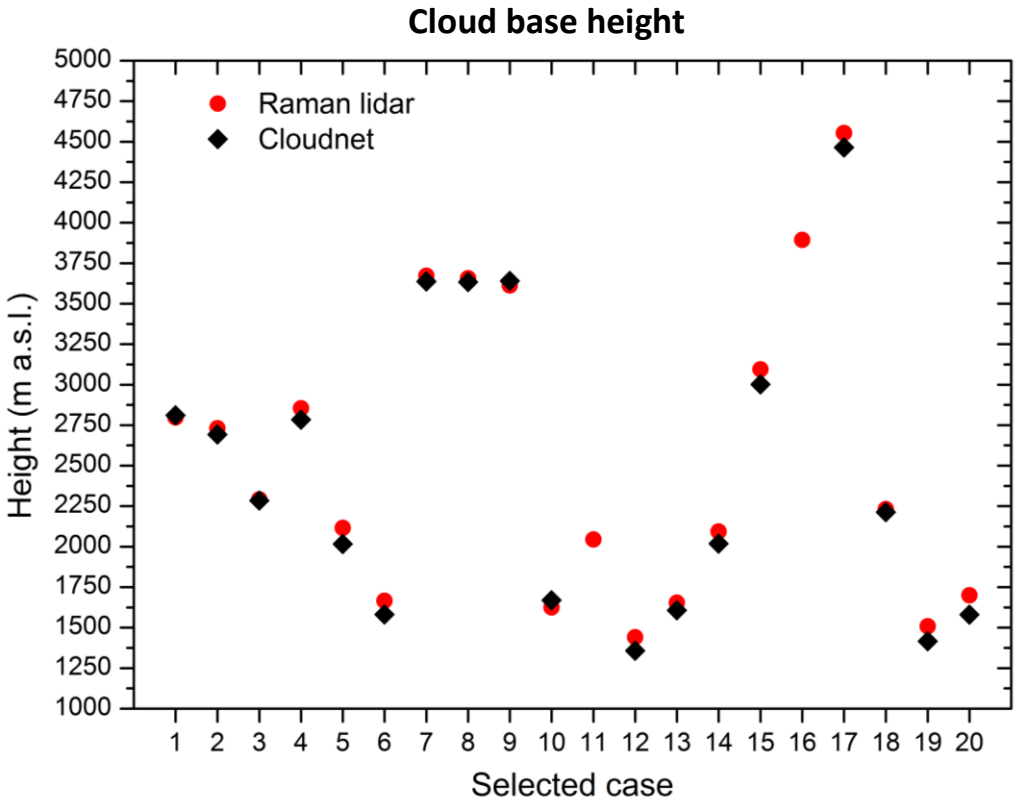

Figure 4.1: Comparison of cloud base height retrieved using Raman lidar signals (red points) and obtained from the Cloudnet algorithm (black points) for the selected case studies. For cases 11 and 16 Cloudnet products are missing.

Figure 4.2 shows the comparison between the cloud top height retrievals using Raman lidar signals (red points) and obtained from the Cloudnet algorithm (black points). For the cases 11 and 16 Cloudnet products are missing, while for the cases 3 and 12, referred to the observations of 26 July 2010 and of 9 September 2010 according to the Table 4.1, further cloud layers are located above the investigated liquid water clouds. The presence of multiple

clouds at different altitudes forces Cloudnet algorithm to provide as the cloud top the altitude of the upper cloud top and not the top altitude of the investigated liquid cloud layer. In 20% of cases, the discrepancy between the two techniques is less than 50 m; in 10% of cases, Raman lidar underestimates the height of the cloud top with respect to Cloudnet, with discrepancies ranging from 70 m to 90 m; in 70% of cases, Raman lidar overestimates the height of the cloud top with respect to Cloudnet, with discrepancies within 60 – 250 m. This overestimation is probably due to the fact that the lidar signal of ceilometer at cloud top is extinguished by the cloud itself and to the fact that the cloud droplet size at cloud top may be outside the radar detectable range. (i.e. droplet radius less than 10 μm). In this case, Cloudnet is not able to detect the upper region of the cloud, which leads to a more accurate determination of cloud top height with Raman lidar technique in comparison to the corresponding determination obtained with Cloudnet algorithms.

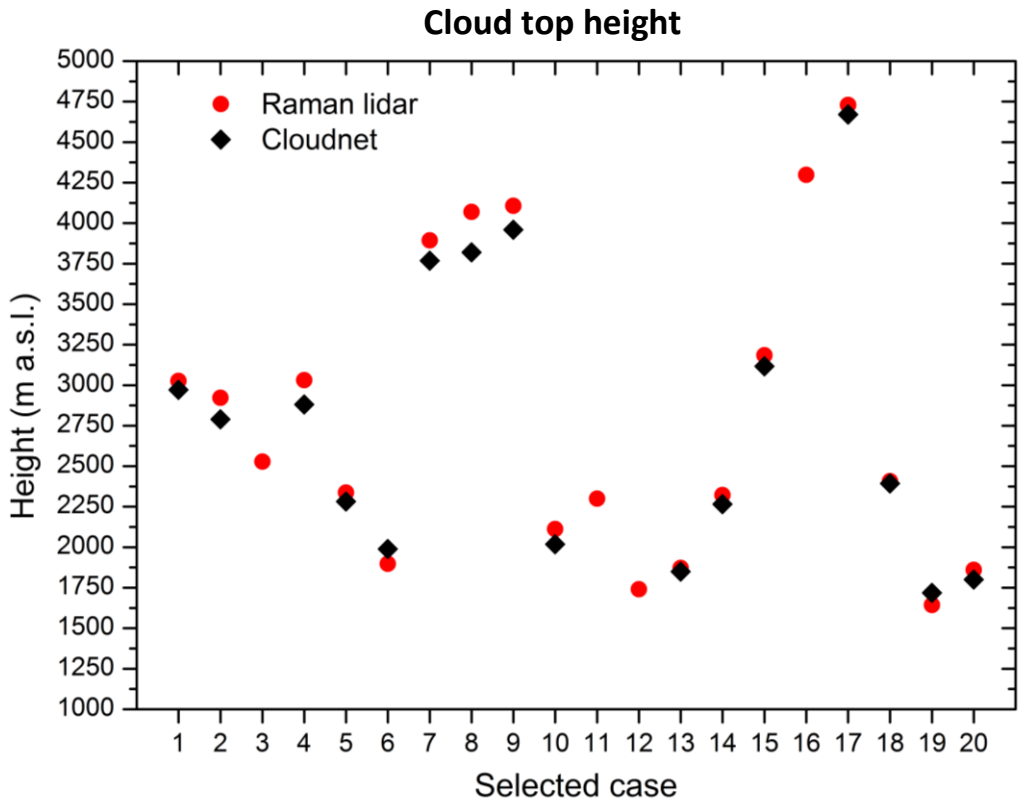

Figure 4.2: Comparison between cloud top height retrievals using Raman lidar signals (red points) and obtained from the Cloudnet algorithm (black points) in the selected case studies. For cases 11 and 16 Cloudnet products are missing; for cases 3 and 12 there are clouds above the analyzed liquid clouds and Cloudnet algorithm do not provide the top height of the selected clouds.

4.3 Statistical results with Raman lidar

For all the selected broken liquid water clouds, the variability of optical properties and humidity in the transition from the cloudy regions to the cloud-free regions surrounding the clouds has been studied with the aim to experimentally investigate the activation of aerosol particles and the cloud formation process.

Figure 4.3 shows the probability density function (pdf) of particle extinction coefficient values at 355 nm calculated with clouds (blue columns) and without clouds (red columns) in the altitude range between the base and the top of the activation region. Figures 4.4 and 4.5 show the pdfs of 355 nm particle backscattering coefficient and of 355 nm particle lidar ratio, respectively, with the same conventions and in the same altitude range of figure 4.3. In figure 4.3, it can be observed that for values of extinction coefficient higher than 3.5×10^{-4} m^{-1}, the probability in the analysis with clouds is much higher than that without clouds; for values of extinction coefficient lower than 1.0×10^{-4} m^{-1}, the probability in the analysis with clouds is much lower than that without clouds; for values of extinction coefficient in the range from 1.0×10^{-4} m^{-1} to 3.5×10^{-4} m^{-1}, the probabilities in the analysis with and without clouds are comparable. These results can be interpreted as follows: for values of extinction coefficient higher than 3.5×10^{-4} m^{-1}, there is an high probability to be within the activation region, where CCN activate and droplets are formed; for values of extinction coefficient lower than 1.0×10^{-4} m^{-1}, the probability to be within the activation region is very low, meaning that the probability of aerosol activation and cloud formation is very low; for extinction coefficient values in the range from 1.0×10^{-4} m^{-1} to 3.5×10^{-4} m^{-1}, the probabilities to be and not to be within the activation region are comparable, meaning that the probabilities of CCN activation or not activation are comparable. Therefore, the extinction coefficient values in this range do not allow to discriminate between cloudy and cloudless regions; this range of values might be identified as the transition region between clouds and cloud-free atmosphere or “Twilight Zone”, defined as the region containing small fragments of clouds, hydrated aerosol, as well as incipient and decaying clouds (Koren et al., 2007). From Figure 4.4 it can be similarly deduced that: for values of backscattering coefficient higher than 1.0×10^{-5} m^{-1} sr^{-1}, there is an high probability to be within the activation region, meaning that there is an high probability of CCN activation and droplet formation; for values of backscattering coefficient lower than 0.6×10^{-5} m^{-1} sr^{-1}, the probability to be within the activation region is very low, meaning that the probability of CCN activation and cloud formation is very low; for values of backscattering coefficient in the range from 0.6×10^{-5} m^{-1} sr^{-1} to 1.0×10^{-5} m^{-1} sr^{-1}, the probabilities to be and not to be within

the activation region are comparable, meaning that the probabilities of CCN activation or not activation are comparable. These values of backscattering coefficient do not allow to discriminate between cloudy and cloudless regions and might identity the “Twilight Zone”. Finally, from Figure 4.5 it can be deduced that: for values of lidar ratio lower than 25 sr, there is an high probability of CCN activation and cloud formation; for lidar ratio values higher than 55 sr, the probability of CCN activation and cloud formation is very low; for lidar ratio values in the range from 25 sr to 55 sr, the probabilities of CCN activation or not activation are comparable. These values of lidar ratio do not allow to discriminate between cloudy and cloudless regions and might identify the “Twilight Zone”.

In summary, for each optical parameter considered in this study, it is possible to identify two threshold values to discriminate between aerosol activation and not activation. These values are 1.0×10^{-4} m^{-1} and 3.5×10^{-4} m^{-1} for extinction coefficient, 0.6×10^{-5} m^{-1} sr^{-1} and 1.0×10^{-5} m^{-1} sr^{-1} for backscattering coefficient, 25 sr and 55 sr for lidar ratio. For values of extinction coefficient and backscattering coefficient higher than 3.5×10^{-4} m^{-1} and 1.0×10^{-5} m^{-1} sr^{-1}, respectively, and for lidar ratio values lower than 25 sr, there is an high probability of CCN activation and droplets formation; for values of extinction coefficient and backscattering coefficient lower than 1.0×10^{-4} m^{-1} and 0.6×10^{-5} m^{-1} sr^{-1}, respectively, and for lidar ratio values higher than 55 sr, the probability of CCN activation and cloud formation is very low. For values of optical parameters in the range between the threshold values, that is for extinction coefficient in the range from 1.0×10^{-4} m^{-1} to 3.5×10^{-4} m^{-1}, backscattering coefficient in the range from 0.6×10^{-5} m^{-1} sr^{-1} to 1.0×10^{-5} m^{-1} sr^{-1} and lidar ratio in the range from 25 sr to 55 sr, the probabilities of activation and not activation are comparable. These values of optical parameters do not allow to discriminate between cloudy and cloudless regions and might identify the transition region between clouds and cloud-free atmosphere or “Twilight Zone”(Koren et al., 2007).

These results can be used to directly evaluate and improve the ability of cloud numerical models to predict the droplet activation, by ground-based Raman lidar measurements of extinction and backscattering coefficients. This evaluation of cloud models also implies an indirect validation of the parameterizations of droplet activation used in these models. Moreover, the above mentioned lidar measurements can be used also to better parameterize model diagnostic variables based on the comparison of the pdfs obtained by the model and by the measurements.

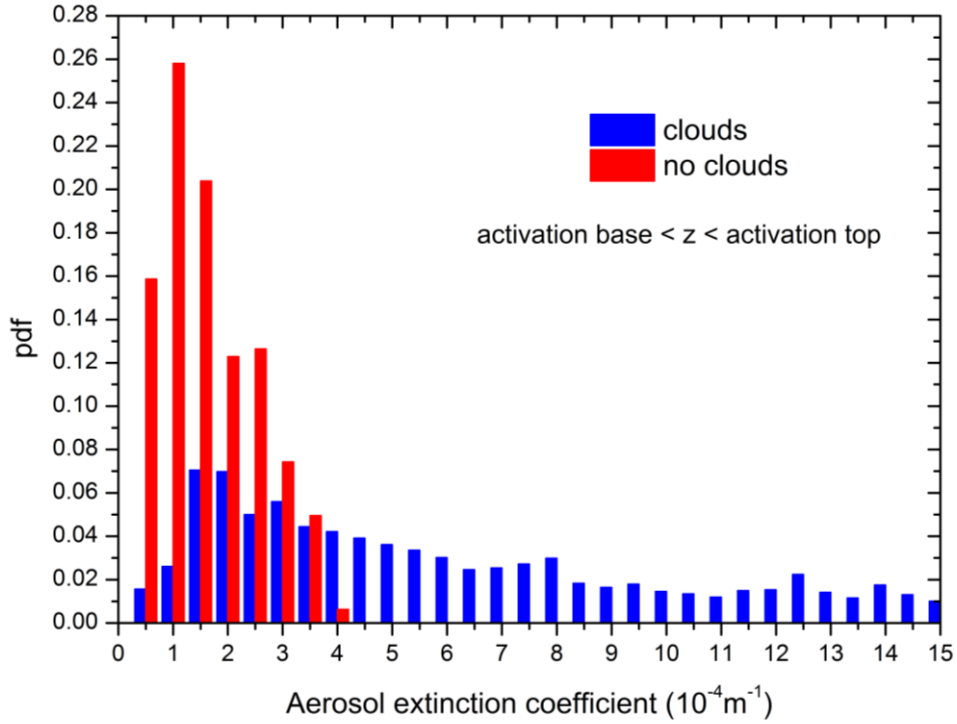

Figure 4.3: Probability density function of particle extinction coefficient at 355 nm "with clouds" (blue columns) and "without clouds" (red columns) in the altitude range between the base and the top of the activation region for the selected case studies.

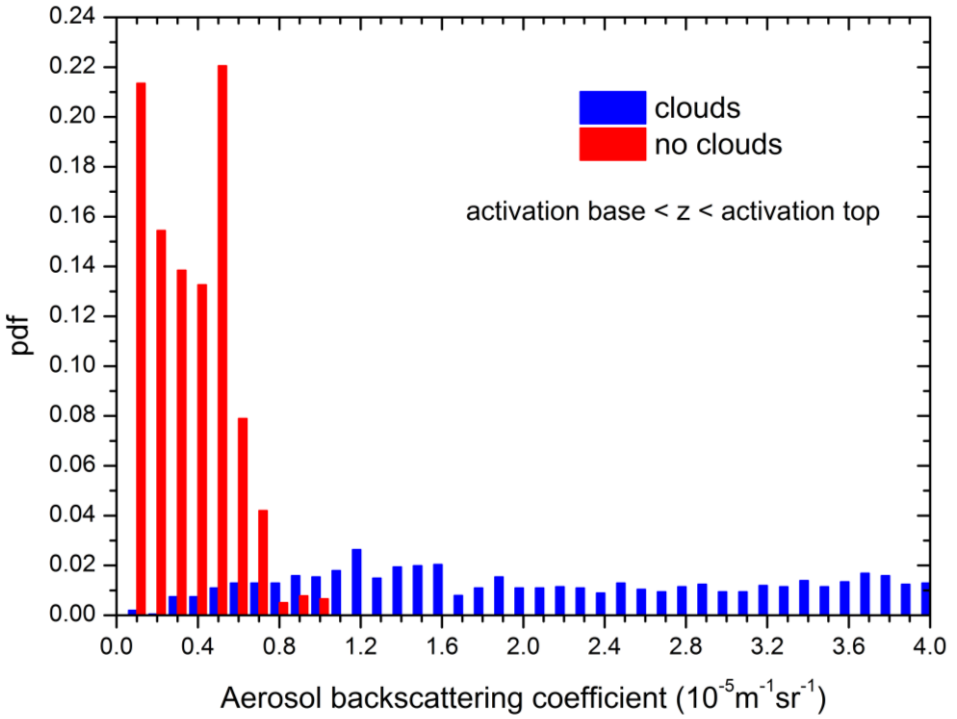

Figure 4.4: Probability density function of particle backscattering coefficient at 355 nm "with clouds" (blue columns) and "without clouds" (red columns) in the altitude range between the base and the top of the activation region for the selected case studies.

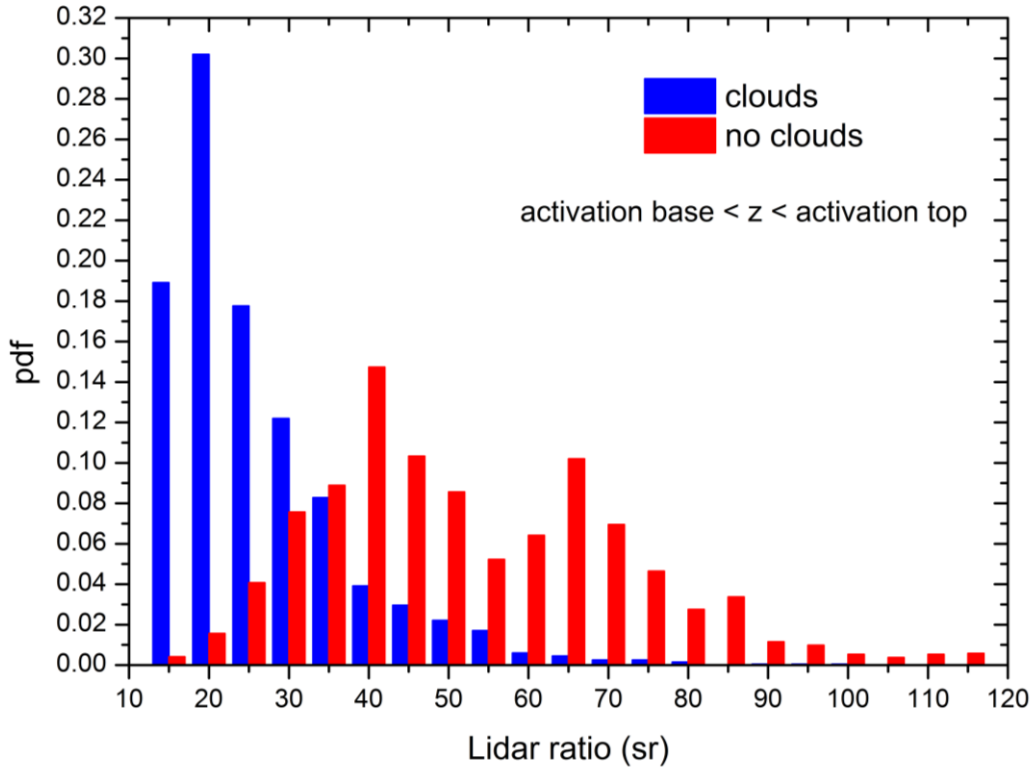

Figure 4.5: Probability density function of particle lidar ratio at 355 nm "with clouds" (blue columns) and "without clouds" (red columns) in the altitude range between the base and the top of the activation region for the selected case studies.

Figure 4.6 shows the pdf of relative humidity (RH) values calculated with clouds (blue columns) and without clouds (red columns) in the altitude range between the base and the top of the activation region. In the selected altitude ranges, RH values are essentially higher than 50% and RH values with pdf greater than 0.1 are higher than 80%, for both clouds and clear sky conditions. For all RH values, the probabilities with clouds and without clouds have comparable values, indicating that for all RH values the probability of activation is comparable with that of not activation. Therefore, RH pdf does not allow the discrimination between aerosols and clouds. A reason behind this result is that the RH Raman lidar profiles have uncertainties too large to be used for this target classification. Actually, droplet formation in the atmosphere occurs at supersaturation levels typically lower than 1% (Pruppacher and Klett, 2000). Random uncertainties of RH lidar measurements are typically in the range between 10 and 30%. Therefore, Raman lidar measurements of RH do not allow to improve the knowledge of the activation processes.

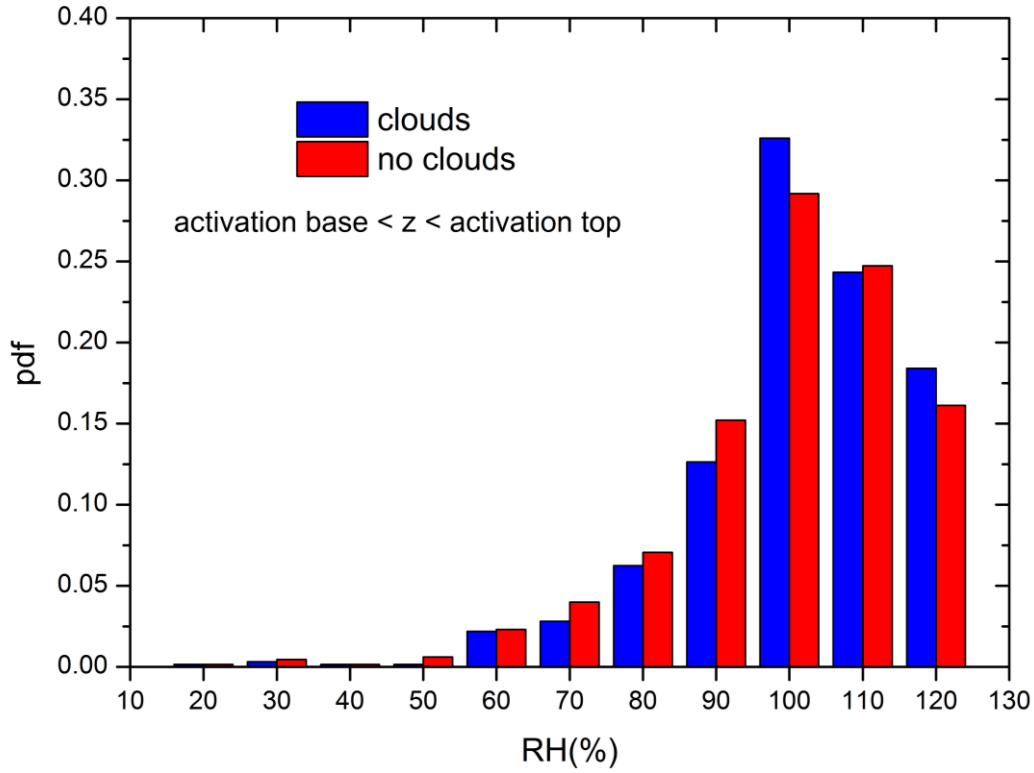

Figure 4.6: Probability density function of relative humidity obtained from Raman lidar analysis "with clouds" (blue columns) and "without clouds" (red columns) in the altitude ranges between the base and top of the activation region for the selected case studies.

Figure 4.7 shows the scatter plot of aerosol extinction coefficient values at 355 nm versus RH values calculated by lidar analysis with clouds in the altitude range of 600 m below the cloud base height; figure 4.8 shows the same scatter plot in the altitude range between the cloud base and cloud top. The lidar extinction profiles, with a raw vertical resolution of 3.75 m, are interpolated on the raw vertical resolution of lidar RH profiles, i.e. 15 m. In Figure 4.7, the data points with extinction coefficient values lower than 1.0 x 10^{-4} m^{-1}, for which the activation probability of CCN is very low, are located below the base of activation region; the points with extinction coefficient between 1.0 x 10^{-4} m^{-1} and 3.5 x 10^{-4} m^{-1} are mostly located below the base of activation region, but a group of them, having RH values higher than 85%, is located within the portion of activation region below the cloud base; the data points with extinction coefficient higher than 3.5 x 10^{-4} m^{-1} are within the activation region below the cloud base. In Figure 4.7, the points of the activation region located below the cloud base are within the blue ellipse. Furthermore, it can be observed that RH is lower than 100% for most of the data points below the cloud base, but a group of data points shows high super-saturation levels (higher than 1%) below the cloud base. These points, although reliable

within the measurement errors, including both the statistical uncertainty and the calibration bias, are probably related to processes not well understood that need further investigation. For example, these points might indicate the presence of large hydrated CCN with sizes comparable to those of the droplets, which have not had sufficient time to form droplets and having values of optical properties and RH similar to those of the droplets. These particles are produced starting from CCN with a large dry diameter and very low critical supersaturation; the timescale of cloud formation is not sufficient for these particles to reach their critical diameter. Nonetheless, the driving force for growth is always positive, and these particles continuously grow, attaining a wet diameter similar or larger to those of the activated droplets. Thus, even though these particles do not activate, they cannot be distinguished from activated droplets, and so should be treated as such (Nenes, 2003).

In Figure 4.8, it can be observed that all the points inside the cloud region are characterized by aerosol extinction coefficient values higher than 3.5×10^{-4} m^{-1} or between 1.0×10^{-4} m^{-1} and 3.5×10^{-4} m^{-1}, and most of these points have RH values higher than 85%. A small group of data points shows lower values of RH inside the clouds (area within the black ellipse in figure 4.8). All these points are located close to the cloud top, where the random uncertainty for RH is high, even higher than 20%, because of the strong extinction of Raman lidar signals due to the cloud water droplets. In some cases, close to the cloud top, the extinction of water vapor Raman signal at 407 nm is much higher than the extinction of nitrogen Raman signal at 387 nm and this leads to an under-estimation of WVMR and RH, which can explain RH values lower than 85%. From the analysis of scatter plots shown in figures 4.7 and 4.8, it can be deduced that the points within the activation region located below the cloud base (area within the blue ellipse in figure 4.7) have values of extinction coefficient (higher than 1.0×10^{-4} m^{-1}) and RH (higher than 85%) similar to those observed within the cloud region.

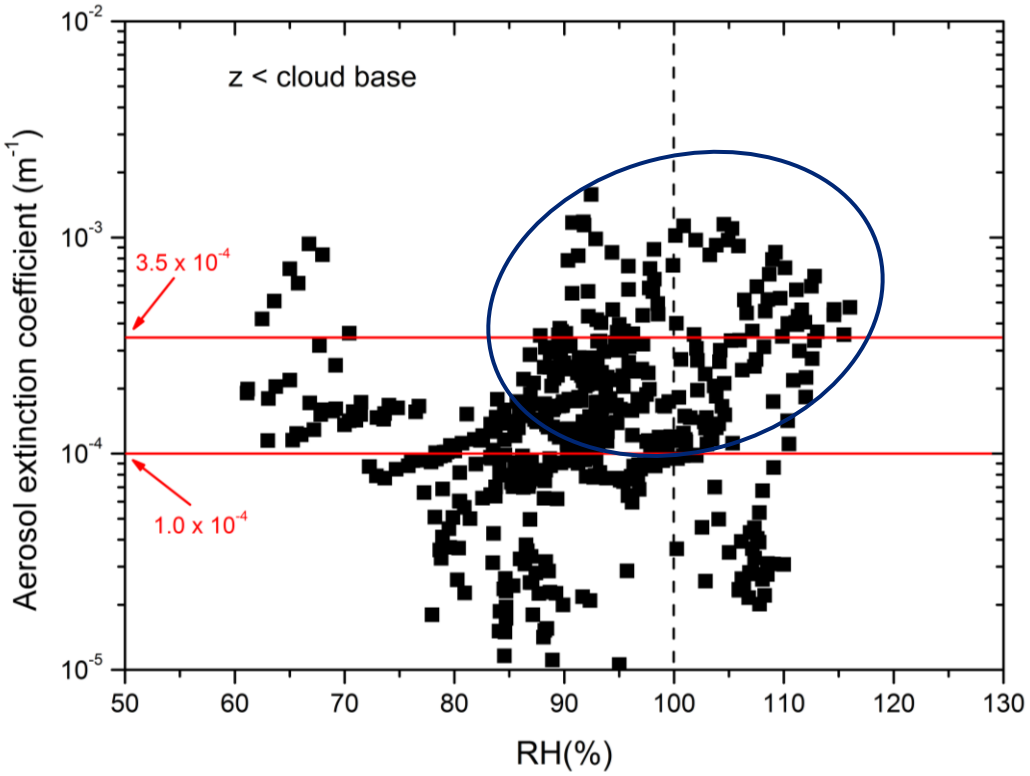

Figure 4.7: Scatter plot of aerosol extinction coefficient at 355 nm versus RH calculated by lidar analysis "with clouds" in the altitude range of 600 m below the cloud base. The area within the blue ellipse contains the points of the activation region located below the cloud base.

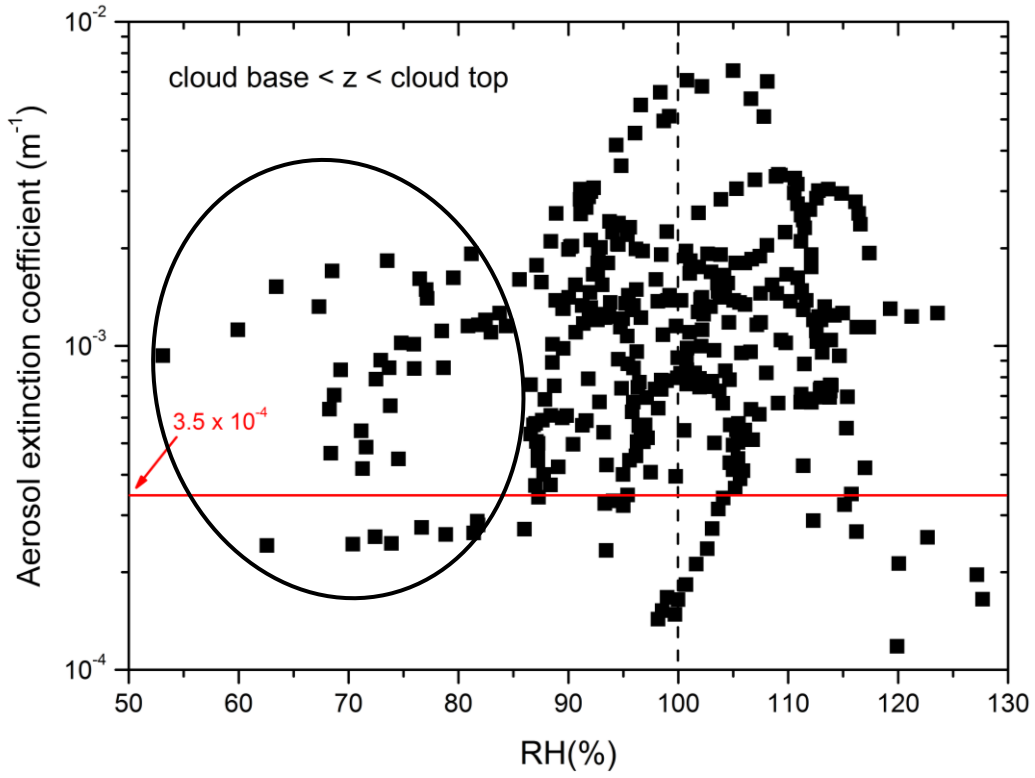

Figure 4.8: Scatter plot of aerosol extinction coefficient at 355 nm versus RH calculated by lidar analysis "with clouds" in the altitude range between the cloud base and cloud top. The area within the black ellipse shows RH values lower than 85% inside the cloud region.

Figure 4.9 shows the scatter plot of aerosol backscattering coefficient values at 355 nm versus RH values calculated by lidar analysis with clouds in the altitude range of 600 m below the cloud base; Figure 4.10 shows the same scatter plot in the altitude range between the cloud base and cloud top. The backscattering profiles, with a raw vertical resolution of 3.75 m, are interpolated on the raw vertical resolution of RH profiles. In figure 4.9, the points with backscattering coefficient values lower than 0.6 x 10^{-5} m^{-1} sr^{-1}, for which the activation probability of CCN is very low, are located below the base of activation region; the points with backscattering coefficient between 0.6 x 10^{-5} m^{-1} sr^{-1} and 1.0 x 10^{-5} m^{-1} sr^{-1} are located partly below the base of activation region and partly within the portion of activation region below the cloud base; the data points with backscattering coefficient higher than 1.0 x 10^{-5} m^{-1} sr^{-1} are within the activation region below the cloud base. In Figure 4.9, the points of the activation region located below the cloud base are within the blue ellipse. Note that RH is lower than 100% for most of the data points below the cloud base, while a group of points shows high super-saturation levels below the cloud base, which can be explained similarly to figure 4.7. In figure 4.10, all the points inside the cloud region have aerosol backscattering coefficient values higher than 1.0 x 10^{-5} m^{-1} sr^{-1} or between 0.6 x 10^{-5} m^{-1} sr^{-1} and 1.0 x 10^{-5} m^{-1} sr^{-1}, and most of these points have RH values higher than 85%. A small group of points, all located close to the cloud top, shows lower values of RH (area within the black ellipse in figure 4.10), which can be explained similarly to figure 4.8. From the analysis of scatter plots shown in figures 4.9 and 4.10, it can be deduced that the points within the activation region located below the cloud base (area within the blue ellipse in figure 4.9) have values of backscattering coefficient (higher than 0.6 x 10^{-5} m^{-1} sr^{-1}) and RH (higher than 85%) similar to those observed within the cloud region.

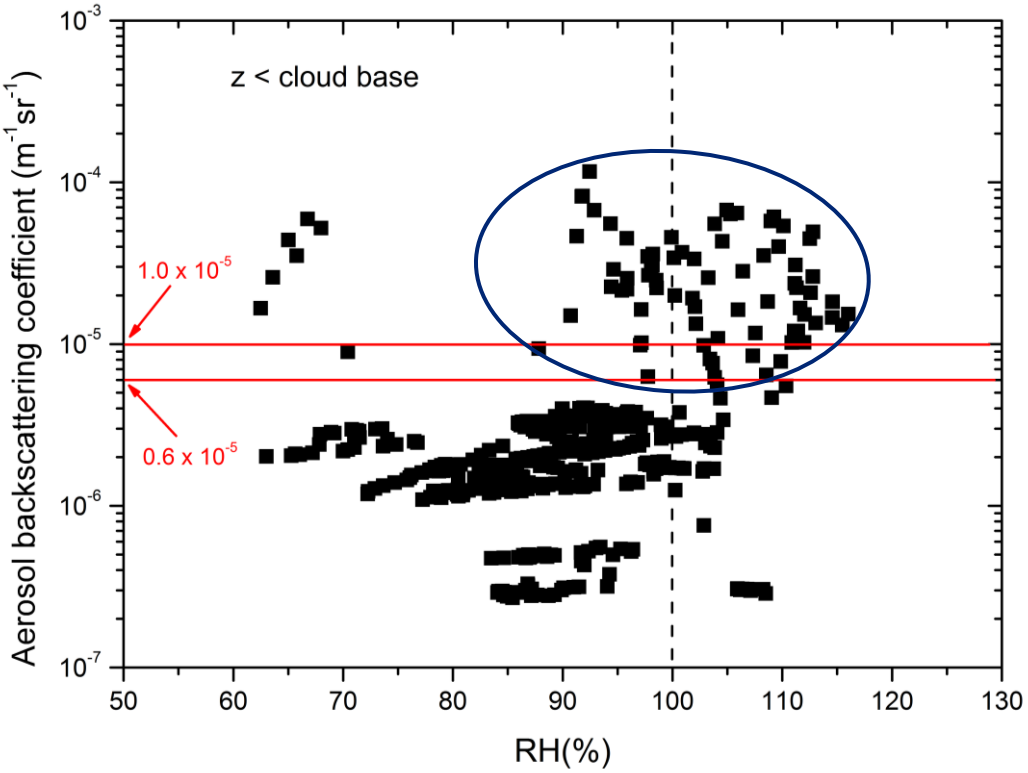

Figure 4.9: Scatter plot of aerosol backscattering coefficient at 355 nm versus RH calculated by lidar analysis "with clouds" in the altitude range of 600 m below the cloud base. The area within the blue ellipse contains the points of the activation region located below the cloud base.

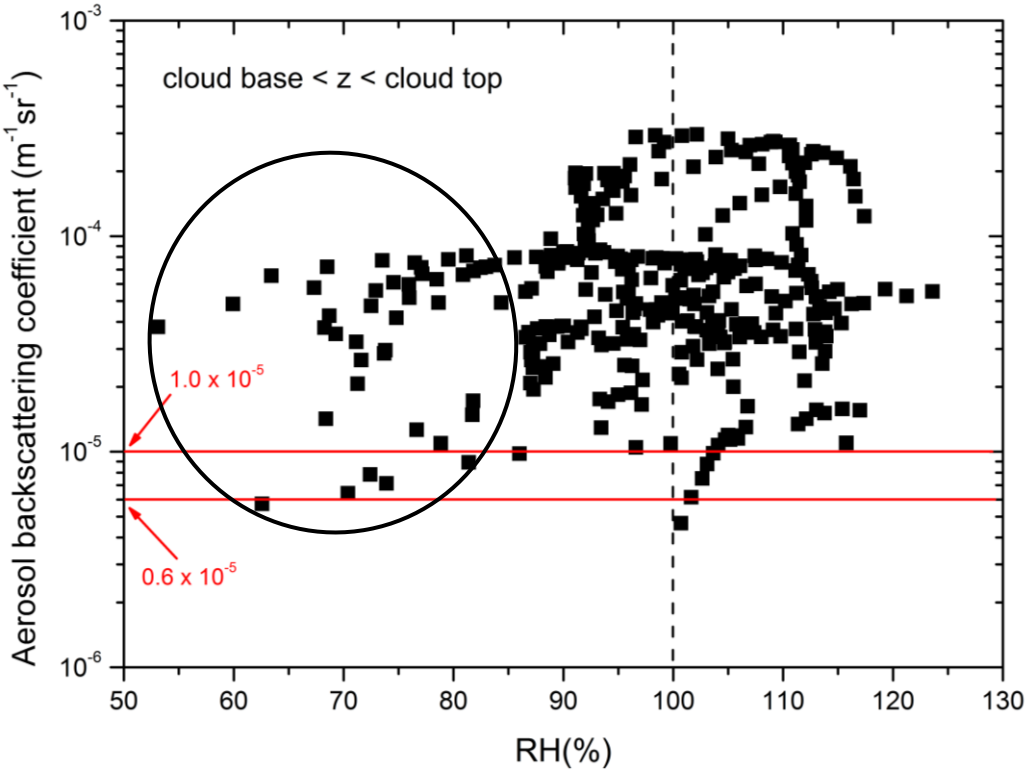

Figure 4.10: Scatter plot of aerosol backscattering coefficient at 355 nm versus RH calculated by lidar analysis "with clouds" in the altitude range between the cloud base and cloud top. The area within the black ellipse shows RH values lower than 85% inside the cloud region.

Figure 4.11 shows the scatter plot of particle lidar ratio values at 355 nm versus RH values calculated by lidar analysis with clouds in the altitude range of 600 m below the cloud base; Figure 4.12 shows the same scatter plot in the altitude range between the cloud base and cloud top. The lidar ratio profiles, with a raw vertical resolution of 3.75 m, are interpolated on the raw vertical resolution of RH profiles. In Figure 4.11, the points with lidar ratio higher than 55 sr, for which the activation probability of CCN is very low, are located below the base of activation region; the points with lidar ratio between 25 sr and 55 sr are mostly located below the base of activation region, but a group of them, having RH values higher than 85%, is located within the portion of activation region below the cloud base; the data points with lidar ratio lower than 25 sr are within the activation region below the cloud base. In Figure 4.11, the points of the activation region located below the cloud base are within the blue ellipse. Note that RH is lower than 100% for most of the data points below the cloud base, while a group of points shows high super-saturation levels below the cloud base, which can be explained similarly to figure 4.7.

In figure 4.12, all the points inside the cloud region have particle lidar ratio values lower than 25 sr or between 25 sr and 55 sr, and most of these points have RH values higher than 85%. A small group of points, all located close to the cloud top, shows lower values of RH (area within the black ellipse in figure 4.12), which can be explained similarly to figure 4.8. From the analysis of scatter plots shown in figures 4.11 and 4.12, it can be deduced that the points within the activation region located below the cloud base (area within the blue ellipse in figure 4.11) have values of lidar ratio (lower than 55 sr) and RH (higher than 85%) similar to those observed within the cloud region.

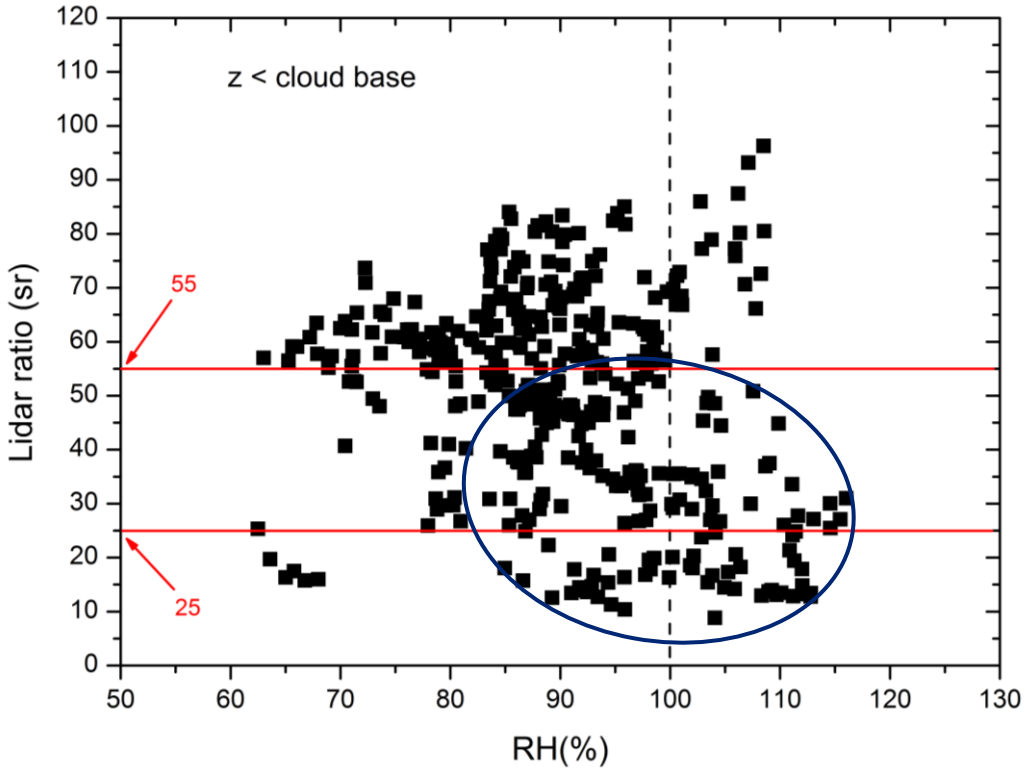

Figure 4.11: Scatter plot of particle lidar ratio at 355 nm versus RH calculated by lidar analysis "with clouds" in the altitude range of 600 m below the cloud base. The area within the blue ellipse contains the points of the activation region located below the cloud base.

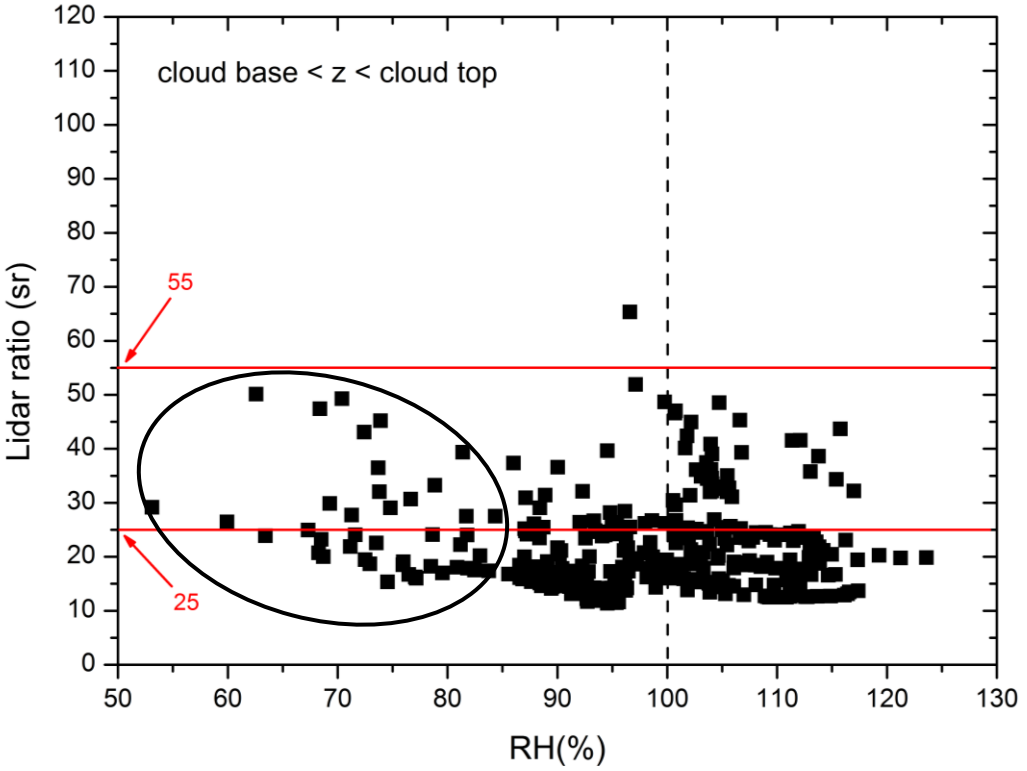

Figure 4.12: Scatter plot of particle lidar ratio at 355 nm versus RH calculated by lidar analysis "with clouds" in the altitude range between the cloud base and cloud top. The area within the black ellipse shows RH values lower than 85% inside the cloud region.

In conclusion, from the analysis of all the scatter plots shown before, it is deduced that the portion of the activation region that is below the cloud base and the cloud region are characterized by similar values of optical properties and RH: extinction coefficient higher than 3.5 x 10^{-4} m^{-1} or, less likely, between 1.0 x 10^{-4} m^{-1} and 3.5 x 10^{-4} m^{-1}; backscattering coefficient higher than 1.0 x 10^{-5} m^{-1} sr^{-1} or, less likely, between 0.6 x 10^{-5} m^{-1} sr^{-1} and 1.0 x 10^{-5} m^{-1} sr^{-1}; lidar ratio lower than 25 sr or, less likely, between 25 sr and 55 sr; RH higher than 85%. Therefore, from these parameters it is not possible to distinguish between these two regions within the larger activation region, even though these regions can be discriminated geometrically by comparing the vertical profiles of **C** and **NC** extinction coefficients and **C** and **NC** nitrogen Raman signals, as shown in Chapter 3. This leads to consider the portion of the activation region that is below the cloud base in two possible ways: it essentially consists of liquid water droplets, which implies to extend the boundaries of cloud region, identifying it with the whole activation region; alternatively, it is essentially formed of large hydrated aerosol particles, with sizes comparable to those of the droplets, which have not had sufficient time to form droplets and having values of optical properties and RH similar to those of the droplets. These particles are produced starting from CCN with a large dry diameter and very low critical supersaturation as described by Nenes (2003).

4.4 Statistical results with Doppler radar

For the selected dataset of broken liquid water clouds, the moments of the radar Doppler spectrum have been studied. In particular, the signal to noise ratio (SNR), the mean Doppler velocity and reflectivity (Z) have been considered. The mean Doppler velocity provides the mean vertical velocities of air masses above the radar with time resolution of 10 s and vertical resolution of 30 m. Positive values of this parameter indicate updrafts, whereas negative values indicate downdrafts.

Aerosol activation and hence cloud droplet concentration and properties depend on the updrafts in the clouds. The aerosols are activated in the lower levels of the cloud region and as these cloud droplets are lofted by the updrafts, water vapor condense because of raised super-saturation due to adiabatic cooling. Several model experiments (Kirshbaum and Smith, 2009) have shown that when the updrafts are well simulated, the aerosol activation models simulate the cloud droplet concentration fairly well. Therefore, measuring updrafts in the clouds and their correlation with aerosol and clouds properties is very interesting. Typically,

an intense updraft produces an intense downdraft since an intense updraft condenses more moisture and this condensate exerts drag on the vertical motions and decreases the buoyancy. Also, intense updrafts increase entrainment of dry air from the atmosphere at the interface between clean air and cloud top, causing cooling and downdrafts.

Doppler Radar measurements are mainly sensitive to large particles, while the sub-micron activated CCN and low concentrations of small droplets (with diameter lower than 20 μm), typically forming liquid water clouds, especially close to the cloud base, fall outside the radar detectable range. This makes challenging to identify the vertical motion at the very beginning of the CCN activation (at the cloud base) and droplet formation. Indeed, this identification is often not possible by the typical processing of radar measurements performed at CIAO based on the averaging 200 consecutive spectra with a time resolution of 10 s and vertical resolution of 30 m. On the other hand, it may become possible by a different processing of radar measurements that increase the radar sensitivity. For example, the data processing performed averaging 1200 consecutive spectra and 3 range gates with a time resolution of 1 minute and vertical resolution of 90 m allows to enhance the radar sensitivity of 5 - 10 dBZ (Rosoldi et al, 2013).

Among the 20 cases selected for lidar analysis, the radar detects a Doppler spectrum only in 10 cases. For each of these cases, the temporal evolution of vertical velocity in clouds at the closest altitude to the cloud base inside the radar detectable range is considered. Two typical situations are observed. The first consists of layers slightly detected by the radar with only a few points with a mainly positive vertical velocity, that indicates a prevailing effect of the buoyancy on the droplets. Alternatively, layers detected for longer time interval and characterized by strong updrafts and downdrafts followed by slightly negative velocities only; this indicates of major role of entrainment related to strong updrafts likely not detected at the beginning of droplets activation, because out of the radar sensitivity.

Figure 4.13 shows the pdf of vertical velocities measured by Doppler radar inside the clouds at the closest altitudes to the cloud base and in the time windows of lidar analysis. Close to the cloud base, the vertical velocities typically range from - 1.5 m s^{-1} to + 0.5 m s^{-1}, with a pdf median value around - 0.25 m s^{-1}, indicating a prevalence of downdrafts on the droplets.

Figure 4.14 shows the pdf of radar reflectivity values in clouds at the same altitudes and in the same time windows of the pdf reported in Figure 4.13. The pdf is negatively skewed with a sharp decrease for values of Z larger than - 42.5 dBZ. Moreover, the pdf shows a regression coefficient of 0.85 if fitted over a mono-modal Gaussian distribution, but the coefficient increases up to 0.95 if the distribution is fitted over a bi-modal Gaussian distribution with peaks centered around - 50 dBZ and - 42.5 dBZ. This indicates the likely presence of two

modes in the size distribution of cloud droplets. Known that the radar reflectivity is directly related to the droplet concentration and to the 6^{th} power of droplet size and assuming comparable number concentrations of droplets for the two modes, theoretical simulations have been used to investigate the possible droplet sizes generating the values of reflectivity measured by the Doppler radar. The simulations take advantage of existing codes for the calculation of scattering and absorption properties of cloud droplets at the radar wavelength, starting from cloud microphysical properties. The codes, based on the T-matrix method (Waterman, 1971; Barber and Yeh, 1975) and the Mueller-matrix method (Vivekanandan et al. 1991), use as input data droplet shape, temperature, dielectric constant, orientation and size distribution and provide different radar products, such as reflectivity and LDR, as output.

Simulations performed with the code designed by Carey (Carey and Rutledge, 1998) are performed, assuming a gamma cloud droplet size distribution with mean diameter of 10 μm and number concentration within 100-1000 cm^{-3}, as reported in literature for continental liquid water clouds (Miles et al., 2000; Quante, 2004; Wallace and Hobbs, 2006) and random droplet orientation distribution. These simulations show that reflectivity values of - 50 dBZ and - 42.5 dBZ refer to droplet size of about 10 μm and 15 μm, respectively. Therefore, the droplet size distribution identified by the radar reflectivity pdf in figure 4.14 is characterized by mean droplet diameters not greater than 15 μm and by the presence of two modes with droplet diameters around 10 μm and 15 μm, respectively.

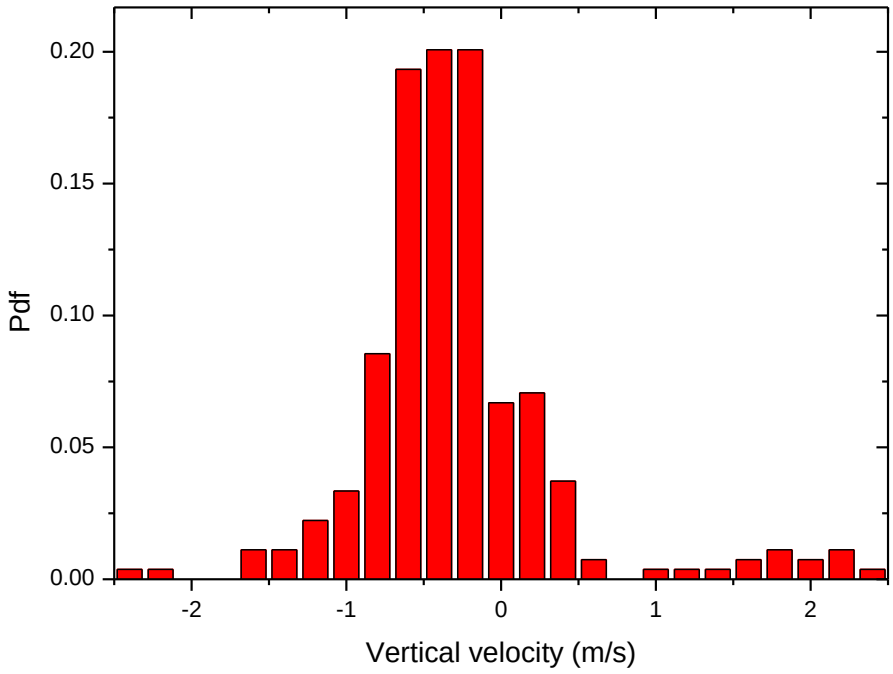

Figure 4.13: Probability density function of vertical velocities measured by the Doppler radar inside the clouds at closest altitudes to the base of the ten cloud layers selected in this work that are inside the radar detectable range. Positive velocities indicate updrafts and negative velocities indicate downdrafts.

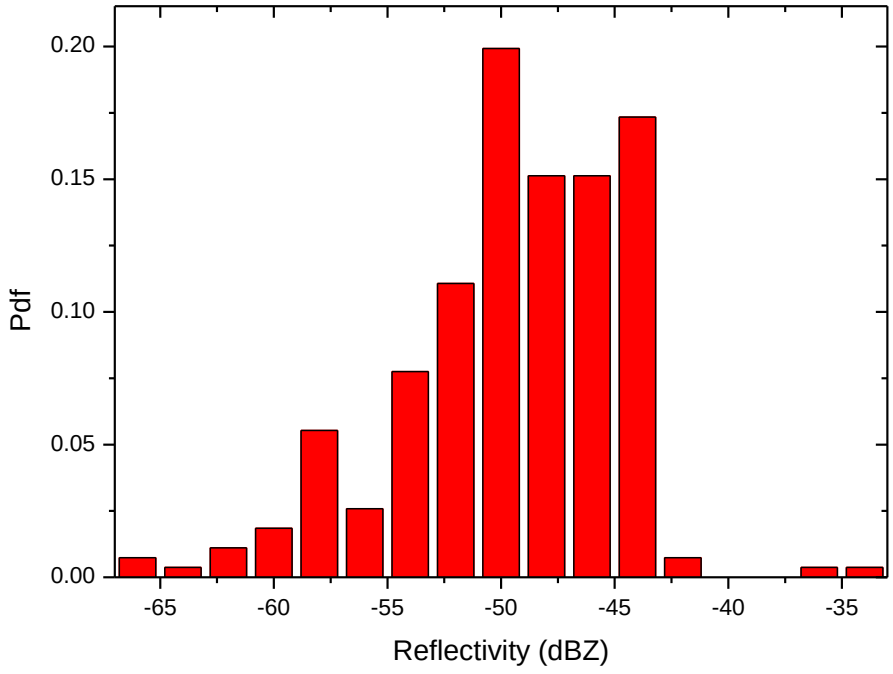

Figure 4.14: Probability density function of radar reflectivity values measured by the Doppler radar inside the clouds at closest altitudes to the base of the ten cloud layers selected in this work that are inside the radar detectable range.

Figure 4.15 shows the scatter plot of vertical velocities versus reflectivity measured by Doppler radar in clouds at the same altitudes and time windows of the previous pdfs. There are two main groups of data points (marked areas in Figure 4.15). The points within the smaller area are characterized by positive vertical velocities, between + 1.5 m s^{-1} and + 3 m s^{-1} with a mean value around + 2 m s^{-1}, and reflectivity values between - 55 dBZ and - 45 dBZ with a mean value around - 50 dBZ. The points within the larger area are characterized by lower mainly negative vertical velocities, between - 1.6 m s^{-1} and + 0.6 m s^{-1} with a mean value around - 0.4 m s^{-1}, and reflectivity values over a larger dynamic range, from - 66 dBZ to - 42 dBZ. The first group represents droplets moving upward, likely because of the buoyancy, while the second group represents droplets mainly moving downward, probably due to an entrainment of dry air at the cloud top in correspondence of the interface between clean air and cloud.

In conclusion, the analysis of the moments of the radar Doppler spectrum provides the following information: close to the cloud base, cloud droplets have size smaller than 15 µm and they are likely distributed in two modes, with droplet size around 10 µm and 15 µm, respectively. Regardless of their size, these droplets are distributed in two different groups: the first is characterized by strong updrafts, with vertical velocities around + 2 m s^{-1}, the second is characterized by lighter downdrafts, with vertical velocities around - 0.4 m s^{-1}. The smallest droplets, with reflectivity values less than - 55 dBZ, belong to the last group.

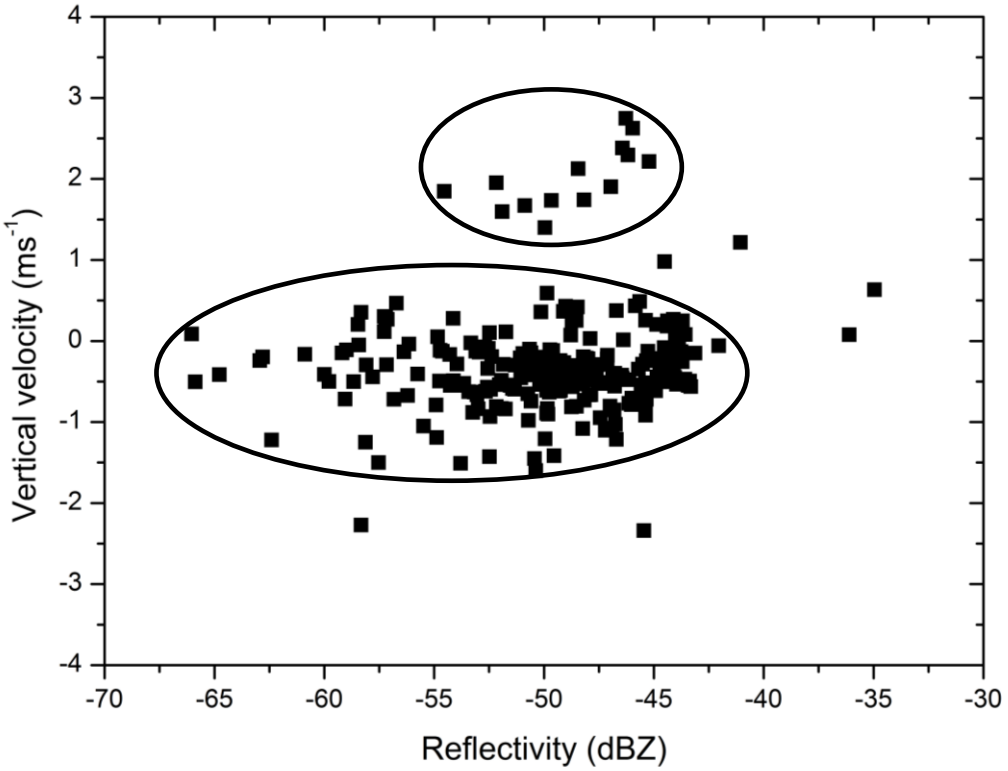

Figure 4.15: Scatter plot of vertical velocities versus reflectivity measured by the Doppler radar inside the clouds at closest altitudes to the base of the ten cloud layers selected in this work that are inside the radar detectable range. Positive velocities indicate updrafts and negative velocities indicate downdrafts. The smaller marked area represents droplets moving upward, the larger marked area represents droplets mainly moving downward.

4.5 Aerosol microphysical properties and cloud updrafts-downdrafts

Droplet size distribution in clouds is affected by the size distribution and chemical composition of aerosol particles in cloud-free regions surrounding the clouds, acting as CCN. Therefore, the correlations between droplet size distribution and aerosol microphysical properties are very interesting for studying droplet activation and cloud formation. The size distribution and complex refractive index of CCN in regions surrounding the clouds are retrieved from multi-wavelength Raman lidar observations (see Chapter 3, paragraph 3.5).

Figure 4.16 shows the scatter plot of vertical velocities, averaged over the time windows used for lidar analysis and at closest altitudes to the base of the ten cloud layers selected in this work that are inside the radar detectable range, versus CCN effective radius in cloud-free regions surrounding the clouds. The uncertainty ranges involved in the retrieval of CCN

effective radius are also reported by the horizontal error bars. The errors estimated for CCN effective radius range from 15 % to 33 %.

Two groups of data points are observed: the first characterized by CCN effective radius smaller than 0.8 µm and negative vertical velocities or downdrafts (area marked in blue in Figure 4.16), the second with larger CCN effective radius and positive vertical velocities or updrafts (area marked in red in Figure 4.16). This indicates that CCN with the smaller effective radius (smaller than 0.8 µm) are activated to form droplets moving downward, while CCN with larger effective radius are activated to form droplets moving upward.

In agreement with previous studies (Kollias et al., 2001), it is possible to suppose that smaller aerosol particles induce stronger updrafts, probably not detected by the radar at the beginning of droplet activation. These updrafts generate larger droplets moving downward also under the effect of entrainment of dry air from the cloud-free atmosphere at the interface between clean air and cloud top. Larger CCN induce less intense vertical motion, the droplets are smaller and uplift under the effect of buoyancy.

The correlation between aerosol effective radius and cloud properties has been studied. A first analysis seems to show that increasing values of the effective radius could be associated to larger values of the vertical velocity. However, a more quantitative analysis will be performed on a larger dataset in a follow-up of this work. Moreover, CCN concentration plays a major role in droplet activation process and it is a very interesting parameter to correlate with cloud properties.

It is also worth to mention that the small number of data points on the plot in Figure 4.16 is due to the limitations of radar sensitivity. Therefore, the availability of a Doppler lidar could strongly improve this kind of studies.

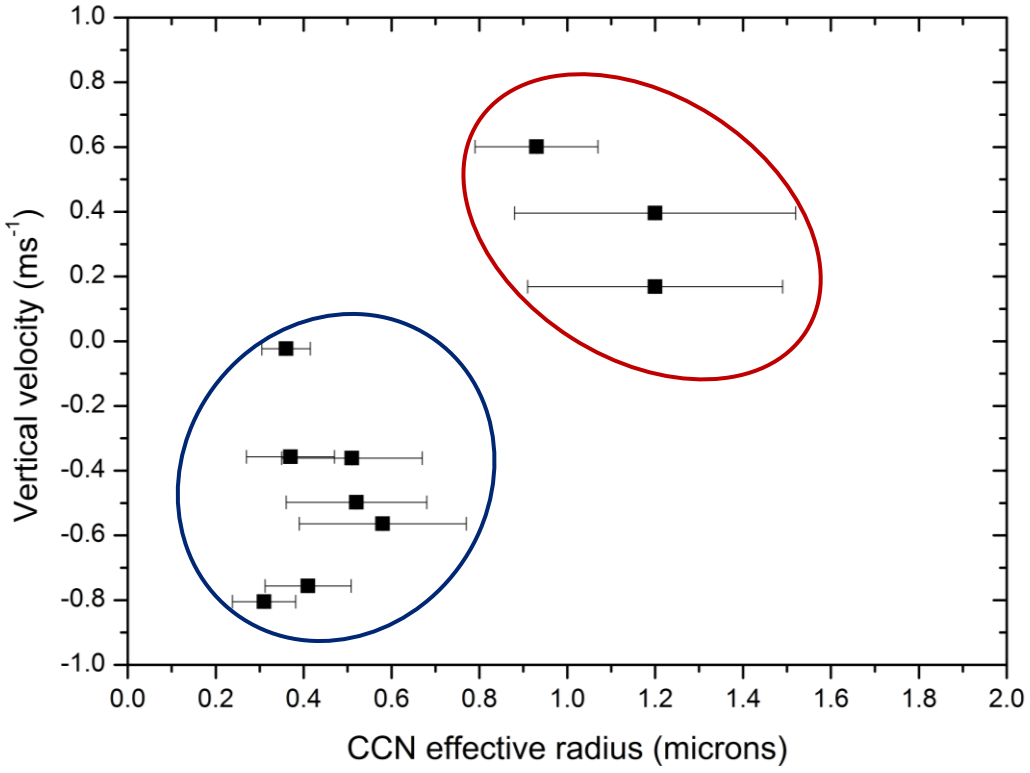

Figure 4.16: Scatter plot of vertical velocities, averaged over the time windows used for lidar analysis at closest altitudes to the base of the ten cloud layers selected in this work that are inside the radar detectable range, versus CCN effective radius in cloud-free regions surrounding the clouds. The horizontal bars represent the uncertainty ranges. The area marked in blue shows negative vertical velocities for CCN effective radius smaller than 0.8 µm and the area marked in red shows positive vertical velocities for higher values of CCN effective radius.

CONCLUSIONS AND OUTLOOKS

Aerosol-cloud interactions, and in particular cloud droplet activation, are not yet accurately quantified and parameterized in weather and climate models, because their experimental investigation is very difficult due to the complexity of the involved processes which take place in the atmosphere far away from the ground. Such investigation needs information on aerosol microphysical and optical properties in proximity of the clouds, as well as cloud microphysical, macrophysical and optical properties. This information can be obtained by ground-based active remote sensing technique, that provides powerful tools for the vertical profiling of aerosol and cloud properties and for the continuous monitoring of cloud evolution. In this work, a new methodology for experimental investigation of droplet activation in optically thin and broken liquid clouds, based on multi-wavelength ground-based Raman lidar and Doppler radar techniques, has been presented. The methodology has been applied to twenty cases characterized by the observation of low or mid-level optically thin broken clouds.

Several properties of cloud layers, such as their geometrical and optical depth, the height and temperature of cloud base and cloud top, the cloud LWP, have been estimated. A comparison with the products provided by the Cloudnet retrieval scheme has been performed. The comparison shows a good agreement with Cloudnet. In particular, Cloudnet and Raman lidar estimations of the heights of cloud base and cloud top have been compared, showing how it is possible to improve the accuracy in the determination of cloud top height using only the Raman lidar signals in comparison to the corresponding determination obtained with Cloudnet algorithms.

A statistical study of the variability of particle optical properties and humidity to characterize the transition from cloudy regions to regions surrounding the clouds is presented and discussed. From this study, threshold values for optical properties at 355 nm, that allow to discriminate between cloudy and cloudless regions, are identified. These values are 1.0×10^{-4} m^{-1} and 3.5×10^{-4} m^{-1} for extinction coefficient, 0.6×10^{-5} m^{-1} sr^{-1} and 1.0×10^{-5} m^{-1} sr^{-1} for backscattering coefficient, 25 sr and 55 sr for lidar ratio. In particular, for values of extinction coefficient and backscattering coefficient higher than 3.5×10^{-4} m^{-1} and 1.0×10^{-5} m^{-1} sr^{-1}, respectively, and for lidar ratio values lower than 25 sr, there is an high probability of aerosol activation and droplet formation; for values of extinction coefficient and backscattering

coefficient lower than 1.0 x 10^{-4} m^{-1} and 0.6 x 10^{-5} m^{-1} sr^{-1}, respectively, and for lidar ratio values higher than 55 sr, the probability of aerosol activation and cloud formation is very low. For values of optical parameters in the range between the threshold values, that is, for extinction coefficient in the range from 1.0 x 10^{-4} m^{-1} to 3.5 x 10^{-4} m^{-1}, backscattering coefficient in the range from 0.6 x 10^{-5} m^{-1} sr^{-1} to 1.0 x 10^{-5} m^{-1} sr^{-1} and lidar ratio in the range from 25 sr to 55 sr, the probabilities of aerosol activation and not activation are comparable. These values of optical parameters do not allow to discriminate between cloudy and cloudless regions and may identify the transition region between clouds and cloud-free atmosphere or "Twilight Zone" (Koren et al., 2007). These results can be used to directly evaluate and improve the ability of cloud numerical models to predict the formation of liquid water clouds, by ground-based Raman lidar measurements of extinction and backscattering coefficients. This evaluation of cloud models also implies an indirect validation of the parameterizations of droplet activation used in these models. Moreover, the above mentioned lidar measurements can be also used to better parameterize model diagnostic variables based on the comparison of the pdfs obtained by the model and by the measurements.

Unlike optical parameters, for RH lidar measurements it has not been identified any threshold value that allows to discriminate between cloudy and cloudless regions, because these measurements have uncertainties too large to be used for such a discrimination. Therefore, these measurements do not allow to improve the knowledge of the activation processes. However, it has been found that droplet activation is always associated to RH values higher than 85% .

A statistical study of the moments of the radar Doppler spectrum leads to the following results: close to the cloud base, the radar Doppler velocity typically ranges from - 1.5 m s^{-1} to + 0.5 m s^{-1}, with a median value around - 0.25 m s^{-1}, indicating a prevalence of downdrafts on the droplets. Close to the cloud base, cloud droplets have size smaller than 15 µm and they are likely distributed in two modes with droplet size around 10 µm and 15 µm, respectively. Regardless of their size, these droplets are distributed in two different groups: the first group is characterized by strong updrafts, with vertical velocities around + 2 m s^{-1}, probably because of the buoyancy; the second group is characterized by lighter downdrafts, with vertical velocities around - 0.4 m s^{-1}, probably due to an entrainment of dry air at the cloud top. The smallest droplets, with reflectivity values less than – 55 dBZ, belong to the last group.

Finally, a correlation between the effective radius of CCN in cloud-free regions surrounding the clouds and droplet updrafts and downdrafts close to the cloud base is found: CCN with

effective radius smaller than 0.8 μm are activated to form droplets moving downward, while CCN with larger effective radius are activated to form droplets moving upward. In agreement with previous studies (Kollias et al., 2001), it is possible to interpret this correlation supposing that smaller aerosol particles induce stronger updrafts, probably not detected by the radar at the beginning of droplet activation; these updrafts generate larger droplets moving downward in a second stage, also under the effect of entrainment of dry air at the cloud top from the cloud-free atmosphere. On the other hand, larger CCN induce less intense vertical motion, the droplets are smaller and uplift under the effect of buoyancy.

The methodology and results presented in this thesis for optically thin and broken liquid clouds can be used as a basis for future research to improve our understanding of aerosol-cloud interactions and cloud droplet activation.

Concerning aerosol-cloud interactions, correlations between cloud optical depth and aerosol optical (optical depth, lidar ratio) and microphysical (effective radius, number concentration) properties in proximity of clouds can be investigated; moreover, from cloud optical depth and LWP the cloud microphysical properties (effective radius and number concentration of droplets) can be retrieved and related to the aerosol optical and microphysical properties. These correlations will be considered in the follow-up of this work.

Concerning droplet activation, the parameterizations used in the models can be directly validated and improved by applying them to the thin liquid water clouds considered in this study. Indeed, the presented methodology allows to derive the aerosol optical and microphysical properties and aerosol type in proximity of the clouds, the cloud optical and microphysical properties, as well as information on the updraft speed and atmospheric thermodynamic properties at the cloud base. All these properties contain information on the input and output (droplet concentration) data used in droplet activation parameterizations, as well as on diagnostic or prognostic variables of global, regional or cloud-resolving numerical models to which these parameterizations are applied. Therefore, these parameterizations and numerical models can be directly validated and improved.

ACKNOWLEDGMENTS

First, I would like to express my gratitude to Dr. Fabio Madonna, who generously helped me during the preparation of this thesis, providing guidance and professional support. I would like to thank Dr. Gelsomina Pappalardo for her supervision and useful suggestions.
I would also like to thank Dr. Aldo Amodeo for his encouragement during the most difficult times and for his valuable scientific support. I would like to express my thanks to Dr. Albert Ansmann and Johannes Bühl for reviewing and improving this thesis.
I would also like to thank all the colleagues in CIAO observatory for their friendship and help during the past three years: Aldo Giunta, Lucia Mona, Giuseppe D'Amico, Francesco Amato, Nikolaos Papagiannopoulos, Pilar Gumà Claramunt and Nicolae Ajtai.
Furthermore, I would like to thank E.E. Eloranta for the availability of his code to calculate the intensity of multiple-scattered light in lidar signals, I. Veselovskii for the availability of his code for retrieval of aerosol microphysical properties and L. D. Carey for the availability of his scattering code. I also would like to thank the NOAA Air Resources Laboratory (ARL) for the provision of the HYSPLIT back trajectory analysis.
Finally, this research would not have been possible without the financial support for the ACTRIS Research Infrastructure Project by the European Union Seventh Framework Programme (FP7/2007-2013) under grant agreement n. 262254.

.

REFERENCES

Abdul-Razzak, H., and S. J. Ghan, "A parameterization of aerosol activation 2. Multiple aerosol types", *J. Geophys. Res., 105 (D5), 6837-6844, 2000.*

Abdul-Razzak, H., and S. J. Ghan, "A parameterization of aerosol activation 3. Sectional representation", *J. Geophys. Res., 107(D3), 4026, 2002.*

Ackermann, I. J., H.Hass, M. Memmesheimer, A. Ebel, F. S. Binkowski, and U. Shankar, "Modal aerosol dynamics model for Europe: Development and first applications", *Atmos. Environ., 32(17), 2981–2999, 1998.*

Ackerman, A. S., M. P. Kirkpatrick, D. E. Stevens, and O. B. Toon, "The impact of humidity above stratiform clouds on indirect aerosol climate forcing", *Nature, 432, 1014–1017, 2004.*

Albrecht, B. A., "Aerosols, cloud microphysics, and fractional cloudiness", *Science, 245(4923), 1227–1230, 1989.*

Amiridis, V., D. Balis, S. Kazadzis, A. Bais, E. Giannakaki, A. Papayannis, and C. Zerefos, "Four-year aerosol observations with a Raman lidar at Thessaloniki, Greece, in the framework of European Aerosol Research Lidar Network (EARLINET)", *J. Geophys. Res., 110, D21203, 2005.*

Ångström, A., "On the atmospheric transmission of Sun radiation and on dust in the air", *Geogr. Ann. Dtsch., 12, 156–166, 1929.*

Ansmann, A., M. Riebesell, and C. Weitkamp, "Measurements of atmospheric aerosol extinction profiles with Raman lidar", *Optics Letters 15, 746-748, 1990.*

Ansmann, A., U. Wandinger, M. Riebesell, C. Weitkamp, and W. Michaelis, "Independent measurement of extinction and backscatter profiles in cirrus clouds by using a combined Raman elastic-backscatter lidar", *Appl. Optics, 31, 7113–7131, 1992a.*

Ansmann, A., M. Riebesell, U. Wandinger, C. Weitkamp, E. Voss, W. Lahmann, and W. Michaelis, "Combined Raman elastic-backscatter lidar for vertical profiling of moisture, aerosol extinction, backscatter, and lidar ratio", *Appl. Phys. B 55, 18–28, 1992b*.

Barber, P., and C. Yeh, "Scattering of electromagnetic waves by arbitrarily shaped dielectric bodies", *Appl. Opt., 14, 2864-2872, 1975.*

Barnaba, F., and G. P. Gobbi, “Lidar estimation of tropospheric aerosol extinction, surface area and volume: Maritime and desert-dust cases”, *J. Geophys. Res., 106, D3, 3005–3018, 2001.*

Barnaba, F., and G. P. Gobbi, “Modeling the Aerosol Extinction versus Backscatter Relationship for Lidar Applications: Maritime and Continental Conditions”, *J. Atmos. Oceanic Technol., 21, 428–442, 2004.*

Bauer-Pfundstein, M., and U. Görsdorf, “Target separation and classification using cloud radar doppler-spectra”, *Proceedings 33rd Intern. Conf. on Radar Meteorology, Cairns, 2007.*

Behrendt, A., and T. Nakamura, “Calculation of the calibration constant of polarization lidar and its dependency on atmospheric temperature”, *Optics Express, Vol. 10, No. 16, pp. 805-817, 2002*

Bösenberg, J., A. Ansmann, J. M. Baldasano, D. Balis, Ch. Böckmann, B. Calpini, A. Chaikovsky, P. Flamant, A. Hagard, V. Mitev, A. Papayannis, J. Pelon, D. Resendes, J. Schneider, N. Spinelli, Th. Trickl, G. Vaughan, G. Visconti, and M. Wiegner, “EARLINET: A European Aerosol Research Lidar Network”, in: Advances in Laser Remote Sensing, edited by: Dabas, A., Loth, C., and Pelon, J., *ISBN 2-7302-0798-8, 155–158, 2001.*

Boucher, O., D. Randall, P. Artaxo, C. Bretherton, G. Feingold, P. Forster, V.-M. Kerminen, Y. Kondo, H. Liao, U.Lohmann, P. Rasch, S.K. Satheesh, S. Sherwood, B. Stevens and X.Y. Zhang: Clouds and Aerosols, in: *Climate Change 2013*: The Physical Science Basis. Contribution of Working Group I to the Fifth Assessment Report of the Intergovernmental Panel on Climate Change, edited by: Stocker, T.F., D. Qin, G.-K. Plattner, M. Tignor, S.K. Allen, J. Boschung, A. Nauels, Y. Xia, V. Bex and P.M. Midgley, Cambridge University Press, Cambridge, United Kingdom and New York, NY, USA, 2013.

Cadeddu, M. P., D. D.Turner, and J. C. Liljegren, “A neural network for real-time retrievals of PWV and LWP from Arctic millimeter-wave ground-based observations”, *IEEE Trans. Geosci. Remote Sens., 47, 1887–1900, 2009.*

Carey, L. D., and S. A. Rutledge, “Electrical and multiparameter radar observations of a severe hailstorm”, *J. Geophys. Res., 103, 13979–14000, 1998.*

Chuang, P. Y., R. J. Charlson, and J. H. Seinfeld , “Kinetic limitations on droplet formation in clouds”, *Nature(London), 390 (6660), 594–596, 1997.*

Collis, R., and P. Russell, “Lidar Measurement of Particles and Gases by Elastic Backscattering and Differential Absorption”, *Laser Monitoring of the Atmosphere, edited by E. Hinkley, chap. 4, pp. 71–151, Springer, New York, 1976.*

D’Amico, G., et al., “EARLINET Single Calculus Chain for automatic lidar data processing: first tests on optical products”, *Reviewed and Revised Papers of the 26th International Laser Radar Conference, Volume 1, pp. 331-334, 2012.*

Dey, S., L. Di Girolamo, and G. Zhao, "Scale effect on statistics of the macrophysical properties of trade wind cumuli over the tropical western Atlantic during RICO", J. Geophys. Res., 113, D24214, 2008.

Di Girolamo, P., P. F. Ambrico, A. Amodeo, A. Boselli, G. Pappalardo, and N. Spinelli, "Aerosol observations by lidar in the nocturnal boundary layer", *Appl. Opt., 38 (21), 4585–4595, 1999.*

Dubovik, O., B. Holben, T. F. Eck, A. Smirnov, Y. J. Kaufman, M. D. King, D. Tanre´, and I. Slutsker, "Variability of absorption and optical properties of key aerosol types observed in worldwide locations," *J. Atmos. Sci., 59, 590–608, 2002.*

Draxler, R.R. and G.D. Rolph, 2014. HYSPLIT (HYbrid Single-Particle Lagrangian Integrated Trajectory) Model access via NOAA ARL READY Website (http://ready.arl.noaa.gov/HYSPLIT.php). NOAA Air Resources Laboratory, Silver Spring, MD.

Ekman, A. M. L., C. Wang, and J. Ström , "Explicit simulation of aerosol physics in a cloud-resolving model", *Atmospheric Chemistry and Physics, 4, 773–791, 2004.*

Eloranta, E.E., "Practical model for the calculation of multiply scattered lidar returns", *Applied Optics, Vol.37, N.12, 2464 – 2472, 1998.*

Facchini, M. C., M. Mircea, S. Fuzzi, and R. J. Charlson "Cloud albedo enhancement by surface-active organic solutes in growing droplets" *Nature, 401: 257-259, 1999.*

Feingold, G., W. L. Eberhard, D. E. Veron, and M. Previdi, "First measurements of the Twomey indirect effect using ground-based remote sensors", *Geophys. Res. Lett., 30(6), 1287, 2003.*

Forster, P., V. Ramaswamy, P. Artaxo, T. Berntsen, R. Betts, D. W. Fahey, J. Haywood, J. Lean, D. C. Lowe, G. Myhre, J. Nganga, R. Prinn, G. Raga, M. Schulz, and R. Van Dorland: Changes in Atmospheric Constituents and in Radiative Forcing, in: Climate Change 2007: The Physical Science Basis. Contribution of Working Group I to the Fourth Assessment Report of the Intergovernmental Panel on Climate Change, edited by: Solomon, S., D. Qin, M. Manning, Z. Chen, M. Marquis, K. B. Averyt, M. Tignor, and H. L. Miller, Cambridge University Press, Cambridge, UK and New York, NY, USA, 2007.

Fountoukis, C. and A. Nenes, "Continued development of a cloud droplet formation parameterization for global climate models", J. Geophys. Res., 110, D11212, 2005.

Hegg, D.A., and P.V. Hobbs, *Proc. 13th Intern. Conf. on Nucleation and Atmospheric Aerosols, Salt Lake City, 1992.*

Hogan, R.J., and E. J. O'Connor, 2006: "Facilitating cloud radar and lidar algorithms: The Cloudnet Instrument Synergy/Target Categorization product. Cloudnet documentation", *2006 [Available online at www.cloud-net. org/data/products/categorize.html.].*

GCOS report N.107, Systematic Observation Requirements for Satellite based Products for Climate, Supplemental details to the satellite-based component of the "Implementation Plan for the Global Observing System for Climate in Support of the UNFCCC", September, 2006.

Iarlori, M., F. Madonna, V. Rizi, T. Trickl and A. Amodeo, “Effective resolution concepts for EARLINET-ASOS products”, in preparation.

Illingworth, A.J., R. J. Hogan, E. J. O’Connor, D. Bouniol, M. E. Brooks, J. Delanoë, D. P. Donovan, J. D. Eastment, N. Gaussiat, J. W. F. Goddard, M. Haeffelin, H. Klein Baltink, O. A. Krasnov, J. Pelon, J.-M. Piriou, A. Protat, H. W. J. Russchenberg, A. Seifert, A. M. Tompkins, G.-J. Van Zadelhoff, F. Vinit, U. Willén, D. R. Wilson, And C. L. Wrench, “CLOUDNET: Continuous Evaluation of Cloud Profiles in Seven Operational Models Using Ground-Based Observations”, *Bull. Am. Meteorol. Soc., 88, 883-898, 2007.*

Jensen, J. B., and R. J. Charlson, “On the efficiency of nucleation scavenging”, *Tellus B, 36: 367-375, 1984.*

Jiang, H., H. Xue, A. Teller, G. Feingold, and Z. Levin, “Aerosol effects on the lifetime of shallow cumulus”, *Geophys. Res. Lett., 33, L14806, 2006.*

Kim, B.-G., M. A. Miller, S. E. Schwartz, Y. Liu, and Q. Min, “The role of adiabaticity in the aerosol first indirect effect”, *J. Geophys. Res., 113, D05210, 2008.*

Kirshbaum, D. J., and R. B. Smith, “Orographic Precipitation in the Tropics: Large-Eddy Simulations and Theory”, *J. Atmos. Sci., 66, 2259-2578, 2009.*

Köhler, H., “The nucleus in and the growth of hygroscopic droplets”, *Trans. Faraday Soc., 32(2), 1152–1161, 1936.*

Kollias, P., B. A. Al-brecht, R. Lhermitte, and A. Savtchenko, “Radar observations of updrafts, downdrafts, and turbulence in fair-weather cumuli”, *J. Atmos. Sci., 58, 1750–1766, 2001.*

Koren, I., L. A. Remer, Y. J. Kaufman, Y. Rudich, and J. V. Martins, “On the twilight zone between clouds and aerosols”, *Geophysical Research Letters, Vol. 34, L08805, 2007.*

Kulmala, M., A. Laaksonen, P. Korhonen, T. Vesala, T. Ahonen, and J. C. Barrett, “The effect of atmospheric nitric acid vapor on cloud condensation nucleus activation” *J. Geophys. Res., 98: 22949-22958, 1993.*

Kumar, P., I. N. Sokolik, and A. Nenes, “Parameterization of cloud droplet formation for global and regional models: including adsorption activation from insoluble CCN”, *Atmos. Chem. Phys., 9, 2517–2532, 2009.*

Laaksonen, A., P. Korhonen, M. Kulmala, and R. J. Charlson, “Modifcation of the Kohler equation to include soluble trace gases and slightly soluble substances” *J. Atmos. Sci., 55: 853-862, 1998.*

Lohmann, U., and S. E. Schwartz, “Aerosols and clouds in chemical transport models and climate models”, *Prepared for the Ernst Strüngmann Forum: Perturbed Clouds in the Climate System, Frankfurt, Germany, March 2-7, 2008.*

Madonna, F., A. Amodeo, A. Boselli, C. Cornacchia, V. Cuomo, G. D'Amico, A. Giunta, L. Mona, and G. Pappalardo, "CIAO: the CNR-IMAA advanced observatory for atmospheric research", *Atmos. Meas. Tech., 4, 1191-1208, 2011.*

Madonna, F., A. Amodeo, G. D'Amico, and G. Pappalardo, "A study on the use of radar and lidar for characterizing ultragiant aerosol" *Journal of Geophysical Research: Atmospheres, Vol. 118, 1–16, 2013.*

Marshak, A., S. Platnick, T. Varnai, G. Wen, and R. F. Cahalan, "Impact of three-dimensional radiative effects on satellite retrievals of cloud droplet sizes" J. Geophys. Res., 111, D09207, 2006.

Mattila, T., Y., Viisanen, H. Kokkola, A. Laaksonen, and M. Kulmala, "Enhancement of CCN concentration due to aqueous phase sulfate production in polluted air", *J. Aerosol Sci., 31:360-361, 2000.*

Mattis, I., A. Ansmann, D. Müller, U. Wandinger, and D. Althausen, "Multiyear aerosol observations with dual-wavelength Raman lidar in the framework of EARLINET", *J. Geophys. Res., 109, D13203, 2004.*

McComiskey, A. and G. Feingold, "Quantifying error in the radiative forcing of the first aerosol indirect effect", *Geophys. Res. Lett., 35, L02810, 2008.*

McComiskey, A., and G. Feingold, "The scale problem in quantifying aerosol indirect effects", *Atmos. Chem. Phys., 12, 1031–1049, 2012.*

Miles, N. L., J. Verlinde, and E. E. Clothiaux, "Cloud Droplet Size Distributions in Low-Level Stratiform Clouds", *J. Atmos. Sci., 57, 295 – 310, 2000.*

Ming, Y., V. Ramaswamy, L. J. Donner, and V. T. J. Phillips, "A new parameterization of cloud droplet activation applicable to general circulation models", *J. Atmos. Sci., 63(4), 1348–1356, 2006.*

Mona, L., A. Amodeo, M. Pandolfi, and G. Pappalardo, "Saharan dust intrusions in the Mediterranean area: three years of Raman lidar measurements", *J. Geophys. Res., 111, D16203, 2006.*

Mona, L., C. Cornacchia, G. D'Amico, P. Di Girolamo, G. Pappalardo, G. Pisani, D. Summa, X. Wang, and V. Cuomo, "Characterization of the variability of the humidity and cloud fields as observed from a cluster of ground-based lidar systems", *Q. J. Roy. Meteorol. Soc., 133(S3) 257–271, 2007.*

Mona, L., G. Pappalardo, A. Amodeo, G. D'Amico, F. Madonna, A. Boselli, A. Giunta, F. Russo, and V. Cuomo, "One year of CNR-IMAA multi-wavelength Raman lidar measurements in coincidence with CALIPSO overpasses: Level 1 products comparison", *Atmos. Chem. Phys., 9, 7213–7228, 2009.*

Müller, D., U. Wandinger, D. Althausen, and M. Fiebig, "Comprehensive particle characterization from three-wavelength Raman-lidar observations: case study", *Appl. Opt., 40(27), 4863–4869, 2001.*

Müller, D., A. Ansmann, I. Mattis, M. Tesche, U. Wandinger, D. Althausen, and G. Pisani, "Aerosol-type-dependent lidar ratios observed with Raman lidar", *Journal of Geophysical Research: Atmospheres, Vol. 112, D16202, 2007.*

Nenes, A., S. Ghan, H. Abdul-Razzak, P. Y. Chuang, and J. H. Seinfeld, "Kinetic limitations on cloud droplet formation and impact on cloud albedo", *Tellus B, 53(2): 133-149, 2001.*

Nenes, A., "Toward an Understanding of the Indirect Climatic Effect of Aerosols", *PhD thesis, California Institute of Technology, Pasadena, California, 2003.*

Nenes, A., and J. Seinfeld, "Parameterization of cloud droplet formation in global climate models", *Journal of Geophysical Research–Atmospheres, 108 (D14), 2003.*

O'Connor, E.J., A.J. Illingworth and R. J. Hogan, "A technique for autocalibration of cloud lidar", *J. Atmos. Ocean. Tech., 21(5), 777- 778, 2004*

Pappalardo, G., A. Amodeo, L. Mona, M. Pandolfi, N. Pergola, and V.Cuomo, "Raman lidar observations of aerosol emitted during the 2002 Etna eruption", *Geophys. Res. Lett., 31, L05120, 2004a.*

Pappalardo G., A. Amodeo, M. Pandolfi, U. Wandinger, A. Ansmann, J. Bosenberg, V. Matthias, V. Amiridis, F. De Tomasi, M. Frioud, M. Iarlori, L. Komguem, A. Papayannis, F. Rocadenbosch, and X. Wang, "Aerosol lidar intercomparison in the framework of the EARLINET, project. 3. Raman lidar algorithm for aerosol extinction, backscatter and lidar ratio", *Appl. Opt., 43(28), 5370–5385, 2004b.*

Pappalardo, G., U. Wandinger, L. Mona, A. Hiebsch, I. Mattis, A. Amodeo, A. Ansmann, P.Seifert, H. Linné, A. Apituley, L. Alados Arboledas, D. Balis, A. Chaikovsky, G. D'Amico, F. De Tomasi, V. Freudenthaler, E. Giannakaki, A. Giunta, I. Grigorov, M.Iarlori, F. Madonna, R.-E. Mamouri, L. Nasti, A. Papayannis, A. Pietruczuk, M. Pujadas, V. Rizi, F. Rocadenbosch, F. Russo, F. Schnell, N. Spinelli, X. Wang, and M. Wiegner, "EARLINET correlative measurements for CALIPSO: First intercomparison results", *J. Geophys. Res., 115, D00H19, 2010.*

Pinnick, R. G., S. G. Jennings, P. Chylek, C. Ham, and W. T. Grandy, "Backscattering and extinction in water clouds", *J. Geophys. Res., 88 (C11), 6787–6796, 1983.*

Peng, Y., and U. Lohmann, "Sensitivity study of the spectral dispersion of the cloud droplet size distribution on the indirect aerosol effect", *Geophys. Res. Lett., 30, 2003.*

Press, W.H., B. P. Flannery, S. A. Teukolsky, and W. T. Vetterling, "Numerical Recipes in FORTRAN: The Art of Scientific Computing", *2nd ed., Cambridge, U. Press, Cambridge, pp. 127–128 and 644–647, 1992.*

Pruppacher, H.R., and J.D. Klett, "Microphysics of Clouds and Precipitation", *Second Revised and Enlarged Edition with an Introduction to Cloud Chemistry and Cloud Electricity, Kluwer Academic Publishers, Dordrecht, Boston, London, pp 110-112, 2000.*

Quante, M., "The role of clouds in the climate system", *Journal De Physique Iv, 121, 61–86, 2004.*

Ramanathan, V., P. J. Crutzen, J. Lelieveld, A. P.Mitra, D. Althausen, J. Anderson, M. O. Andreae, W. Cantrell, G. R. Cass, C. E. Chung, A. D. Clarke, J. A. Coakley, W. D. Collins, W. C. Conant, F. Dulac, J. Heintzenberg, A. J. Heymsfield, B. Holben, S. Howell, J. Hudson, A. Jayaraman, J. T. Kiehl, T. N. Krishnamurti, D. Lubin, G. McFarquhar, T. Novakov, J. A. Ogren, I. A. Podgorny, K. Prather, K. Priestley, J. M. Prospero, P. K. Quinn, K. Rajeev, P. Rasch, S. Rupert, R. Sadourny, S. K. Satheesh, G. E., Shaw, P. Sheridan, and F. P. J. Valero, "Indian Ocean Experiment: An integrated analysis of the climate forcing and effects of the great Indo-Asian haze", *J. Geophys. Res., 106, 28371–28398, 2001.*

Ramaswamy, V., O. Boucher, J. Haigh, D. Hauglustaine, J.Haywood, G. Myhre, T. Nakajima, G. Y. Shi, and S. Solomon: Radiative Forcing of Climate Change, in: Climate Change 2001: The Scientific Basis. Contribution of working group I to the Third Assessment Report of the Intergovernmental Panel on Climate Change, edited by: Houghton, J. T., Y. Ding, D. J. Griggs, M. Noguer, P. J. van der Linden, X. Dai, K. Maskell, and C. A. Johnson, Cambridge Univ. Press, New York, 2001.

Rennó, N. O., E. Williams, D. Rosenfeld, D. G. Fischer, J. Fischer, T. Kremic, A. Agrawal, M. O. Andreae, R. Bierbaum, R. Blakeslee, A. Boerner, N. Bowles, H. Christian, A. Cox, J. Dunion, A. Horvath, X. Huang, A. Khain, S. Kinne, M. C. Lemos, J. E. Penner, U. Pöschl, J. Quaas, E. Seran, B. Stevens, T. Walati, and T. Wagner, "CHASER: An Innovative Satellite Mission Concept to Measure the Effects of Aerosols on Clouds and Climate" *Bull. Amer. Meteor. Soc., 94, 685–694, 2013.*

Rolph, G.D., 2014. Real-time Environmental Applications and Display sYstem (READY) Website (http://ready.arl.noaa.gov). NOAA Air Resources Laboratory, Silver Spring, MD.

Rosenfeld D., E. Williams, M. O. Andreae, E. Freud, U. Pöschl, and N. O. Rennó, "The scientific basis for a satellite mission to retrieve CCN concentrations and their impacts on convective clouds", *Atmos. Meas. Tech., 5, 2039-2055, 2012.*

Rosenfeld, D., S. Sherwood, R. Wood, and L. Donner, "Climate effects of Aerosol-Cloud Interactions", *Science, 343(6169): 379-380, 2014.*

Rosoldi, M., P. Gumà Claramunt, F. Madonna, A. Amodeo, I. Binietoglou, G. D'Amico, A. Giunta, L. Mona, N. Papagiannopoulos, and G. Pappalardo, "Study of thin clouds at CNR-IMAA Atmospheric Observatory (CIAO)", *Annals of Geophysics, 56, Fast Track – 1, 10.4401/ag -6337, 2013.*

Rossow, W.B., and R.A. Schiffer, "Advances in understanding clouds*"* *ISCCP. Bull. Amer. Meteor. Soc., 80(11), 2261-2287, 1999.*

Sasano, Y., E. V. Browell, and S. Ismail, “Error caused by using a constant extinction/backscatter ratio in the lidar solution”, *Appl. Opt., 24, 3929–3932, 1985.*

Schmidt, J., A. Ansmann, J. Bühl, H. Baars, U. Wandinger, D. Müller, and Aleksey V. Malinka, “Dual-FOV Raman and Doppler lidar studies of aerosol-cloud interactions: Simultaneous profiling of aerosols, warm-cloud properties, and vertical wind”, *Journal of Geophysical Research: Atmospheres, Volume 119, Issue 9, pages 5512–5527, 2014*.

Shulman, M. L., M. C. Jacobson, R. J. Charlson, R. E. Synovec, and T. E. Young, “Dissolution behaviour and surface tension effects of organic compounds in nucleating cloud droplets”, *Geophys. Res. Lett., 23: 277-280, 1996.*

Solheim, F., J. Godwin, E. Westwater, Y.Han, S. Keihm, K. Marsh, and R. Ware, “Radiometric profiling of temperature, water vapor, and cloud liquid water using various inversion methods, *Radio Sci., 33, 393–404, 1998.*

Shupe, M. D., J. S. Daniel, G. de Boer, E. W. Eloranta, P. Kollias, C. N. Long, E. P. Luke, D. D. Turner, and J. Verlinde, “A Focus on Mixed-Phase Clouds. The Status of Ground-Based Observational Methods”, *Bull. Amer. Meteor. Soc., 89(10), 1549–1562, 2008.*

Sorjamaa, R. and A. Laaksonen, “The effect of H_2O adsorption on cloud drop activation of insoluble particles: a theoretical framework”, *Atmos. Chem. Phys., 7, 6175–6180, 2007.*

Stacey, D. N., “Rayleigh’s legacy to modern physics: high resolution spectroscopy”, *Eur. J. Phys. 15, 236–242 , 1994.*

Steele, H., “Investigations of Cloud Altering Effects of Atmospheric Aerosols using a New Mixed Eulerian-Lagrangian Aerosol Model”, *Ph.D. thesis, Massachusetts Institute of Technology, 2004*

Stevens, B., W.R. Cotton, G. Feingold, and C.-H. Moeng, “Large-Eddy Simulations of Strongly Precipitating, Shallow, Stratocumulus-Topped Boundary Layers”, *J. Atmos. Sci., 55, 3616–3638, 1998.*

Stocker, T.F., D. Qin, G.-K. Plattner, L.V. Alexander, S.K. Allen, N.L. Bindoff, F.-M. Bréon, J.A. Church, U. Cubasch, S. Emori, P. Forster, P. Friedlingstein, N. Gillett, J.M. Gregory, D.L. Hartmann, E. Jansen, B. Kirtman, R. Knutti, K. Krishna Kumar, P. Lemke, J. Marotzke, V. Masson-Delmotte, G.A. Meehl, I.I. Mokhov, S. Piao, V. Ramaswamy, D. Randall, M. Rhein, M. Rojas, C. Sabine, D. Shindell, L.D. Talley, D.G. Vaughan and S.-P. Xie: Technical Summary, in: Climate Change 2013: The Physical Science Basis. Contribution of Working Group I to the Fifth Assessment Report of the Intergovernmental Panel on Climate Change, edited by: Stocker, T.F., D. Qin, G.-K. Plattner, M. Tignor, S.K. Allen, J. Boschung, A. Nauels, Y. Xia, V. Bex and P.M. Midgley, Cambridge University Press, Cambridge, United Kingdom and New York, NY, USA, 2013.

Turner, D. D., A. M. Vogelmann, R. T. Austin, J. C. Barnard, K. Cady-Pereira, J. C. Chiu, S. A. Clough, C. Flynn, M. M. Khaiyer, J. Liljegren, K. Johnson, B. Lin, C. Long, A. Marshak, S. Y. Matrosov, S. A. McFarlane, M. Miller, Q. Min, P. Minnis, W. O’Hirok, Z. Wang, and W.

Wiscombe, “Thin liquid water clouds: Their importance and our challenge”, *Bull. Amer. Meteor. Soc., 88, 177–190, 2007.*

Twohy, C., M. Petters, J. Snider, B. Stevens, W. Tahnk, M. Wetzel, L. Russell, and F. Burnet, “Evaluation of the aerosol indirect effect in marine stratocumulus clouds: Droplet number, size, liquid water path, and radiative impact”, *J. Geophys. Res., 110, D08203, 2005.*

Twomey, S., “The nuclei of natural cloud formation Part I: The chemical diffusion method and its application to atmospheric nuclei”, *Pure and Applied Geophysics, 43 (1), 227–242, 1959.*

Twomey, S., and T. A. Wojciechowski , “Observations of the geographical variation of cloud nuclei”, *Journal of the Atmospheric Sciences, 26 (4), 648–651, 1969.*

Twomey, S., “Pollution and the planetary albedo”, *Atmos. Environ., 8(12), 1251–1256, 1974.*

Twomey, S., “The influence of pollution on the shortwave albedo of clouds”, *J. Atmos. Sci., 34(7), 1149-1152, 1977.*

Veselovskii, I., A. Kolgotin, V. Griaznov, D. Müller, U. Wandinger, and D. N. Whiteman, “Inversion with regularization for the retrieval of tropospheric aerosol parameters from multiwavelength lidar sounding,” *Appl. Opt., 41, 3685–3699, 2002*.

Veselovskii, I., A. Kolgotin, V. Griaznov, D. Müller, K. Franke, and D. N. Whiteman “Inversion of multiwavelength Raman lidar data for retrieval of bimodal aerosol size distribution”, *Applied Optics, Vol.43, N.5, 1180 – 1195, 2004.*

Vivekanandan, J., W. M. Adams, and V. N. Bringi, “Rigorous approach to polarimetric radar modeling of hydrometeor orientation distributions”, *J. Appl. Meteor., 30, 1053-1063, 1991.*

Wallace, J. M., and P. V. Hobbs, “Atmospheric science: an introductory survey”, *2nd ed., Academic Press, pp 216-217, 2006.*

Wandinger,U., “Multiple-scattering influence on extinction and backscatter coefficient measurements with Raman and high-spectral resolution lidars”, *Applied Optics, Vol.37, N.3, 417 - 427, 1998.*

Wang, S., Q. Wang, and G. Feingold, “Turbulence, condensation and liquid water transport in numerically simulated non precipitating stratocumulus clouds”, *J. Atmos. Sci., 60, 262–278, 2003.*

Waterman, P. C. , “Symmetry, unitarity, and geometry in electromagnetic scattering”, *Phys Rev D, 3, 825–39, 1971.*

Whiteman, D. N., S. H. Melfi, and R. A. Ferrare, “Raman lidar system for measurement of water vapor and aerosols in the Earth’s atmosphere”, *Appl. Opt. 31(16), 3068–3082, 1992.*

Whiteman, D.N., G. Schwemmer, T.Berckoff, H. Plotkin, L. Ramos-Izquierdo, and G. Pappalardo, “Performance modelling of an airborne Raman water vapour lidar”, *Appl. Opt., Vol. 40, No. 3, 2001.*

Whiteman, D. N., “Examination of the traditional Raman lidar technique. I. Evaluating the temperature-dependent lidar equations”, *Applied Optics, 42, No. 15, 2571-2592, 2003.*

Winker, D. M., M. A. Vaughan, A. H. Omar, Y. Hu, K. A. Powell, Z. Liu, W. H. Hunt, and S. A. Young, “Overview of the CALIPSO mission and CALIOP data processing algorithms”, *J. Atmos. Oceanic Technol., 26, 1105–1119, 2009.*

Wu,Y., S. Chaw, B. Gross, F. Moshary, and S. Ahmed, “Low and optically thin cloud measurements using a Raman-Mie lidar”, Applied Optics, Vol. 48, N. 6, 1218-1227, 2009.

Xue, H., and G. Feingold, “Large-eddy simulations of trade wind cumuli: Investigation of aerosol indirect effects”, *J. Atmos. Sci., 63(6), 1605–1622, 2006.*

Young, S. A., and M. A. Vaughan, “The retrieval of profiles of particulate extinction from Cloud-Aerosol Lidar Infrared Pathfinder Satellite Observations (CALIPSO) data: Algorithm description”, *J. Atmos. Oceanic Technol., 26, 1105–1119, 2009.*